Université de Montréal

Modeling and numerical study of the diffusion of point defects in $\alpha-$iron

par

Md Mijanur Rahman

Département de physique

Faculté des arts et des sciences

Thèse présentée en vue de l'obtention du grade de

Philosophiæ Doctor (Ph.D.)

en Physique

Thursday 9th February, 2023

© Md Mijanur Rahman, 2023

Université de Montréal

Faculté des arts et des sciences

Cette thèse intitulée

Modeling and numerical study of the diffusion of point defects in $\alpha-$iron

présentée par

Md Mijanur Rahman

a été évaluée par un jury composé des personnes suivantes :

Prof. François Schiettekatte
(président-rapporteur)

Prof. Normand Mousseau
(directeur de recherche)

Prof. Michel Côté
(membre du jury)

Prof. Joerg Rottler
(examinateur externe)

(représentant du doyen de la FESP)

Résumé

Le fer et les alliages à base de fer présentent un intérêt considérable pour la communauté de la modélisation des matériaux en raison de l'immense importance technologique de l'acier. Les alliages ferritiques à base de fer sont largement utilisés dans les industries aéronautique et nucléaire en raison de leur résistance mécanique élevée, de leur faible dilatation à haute température et de leur résistance à la corrosion. Ces propriétés sont cependant affectées par des défauts ponctuels intrinsèques et extrinsèques. Dans cette thèse, nous décrivons en détail la cinétique des défauts ponctuels dans le fer α en utilisant la technique d'activation-relaxation cinétique (ARTc), une méthode de Monte Carlo cinétique hors réseau avec construction de catalogue à la volée. Plus précisément, nous nous intéressons aux mécanismes de diffusion du carbone (C) et des amas de lacunes dans le fer α. Dans un premier temps, nous étudions l'effet de la pression sur la diffusion du carbone dans le joint de grains de fer α. Nous constatons que l'effet de la pression peut fortement modifier la stabilité et la diffusivité du carbon dans le joint de grains d'une manière qui dépend étroitement de l'environnement local et de la nature de la déformation. Ceci peut avoir un impact majeur sur l'évolution des matériaux hétérogènes, avec des variations de pression locale qui altéreraient fortement la diffusion à travers le matériau. Nous étudions également l'évolution structurale des amas de lacunes contenant de deux à huit lacunes dans le fer α. Nous décrivons en détail le paysage énergétique, la cinétique globale et les mécanismes de diffusion associés à ces défauts. Nos résultats montrent des mécanismes de diffusion complexes même pour des défauts aussi simples que de petits amas de lacunes. Enfin, dans le dernier chapitre, nous discutons une approche de gestion de petites barrières par bassin local dans ARTc. Les simulations de Monte Carlo

cinétiques deviennent inefficaces dans les systèmes où le paysage énergétique est constitué de bassins avec de nombreux états reliés par des barrières énergétiques très faibles par rapport à celles nécessaires pour quitter ces bassins. Au fur et à mesure que le système évolue état par état, il est beaucoup plus susceptible d'effectuer des événements répétés (appelés oscillateurs) à l'intérieur du bassin d'énergie de piégeage que de s'échapper du bassin. De tels osccilateurs ne font pas progresser la simulation et ne fournissent que peu d'informations au-delà d'uen première évaluation de ces états. Notre algorithme de bassin local détecte, à la volée, des groupes d'états oscillants et les consolide en bassins locaux, que nous traitons avec la méthode de taux moyen d'auto-construction de bassin (bac-MRM), une approche de type équation maîtresse selon la méthode du taux moyen.

Mots clés: Défauts ponctuels, Diffusion, Fer, Monte-Carlo cinetique, ARTc

Abstract

Iron and iron-based alloys are of considerable interest to the materials modelling community because of the immense technological importance of steel. Iron-based ferritic alloys are widely used in aeronautic and nuclear industries due to their high mechanical strength, low expansion at high temperatures, and corrosion resistance. These properties are affected by intrinsic and extrinsic point defects, however. In this thesis, we describe in detail the kinetics of point defects in $\alpha-$iron using the kinetic activation-relaxation technique (kART), an off-lattice kinetic Monte Carlo method with on-the-fly catalog building. More specifically, we focus on the diffusion mechanisms of carbon and vacancy clusters in $\alpha-$iron. First, we study the pressure effect on carbon diffusion in the grain boundary (GB) of $\alpha-$iron. We find that the effect of pressure can strongly modify the C stability and diffusivity in the GB in ways that depend closely on the local environment and the nature of the deformation. This can have a major impact on the evolution of heterogeneous materials, with variations of local pressure that would strongly alter diffusion across the material. We also study the structural evolution of vacancy clusters containing two to eight vacancies in $\alpha-$iron. We describe in detail the energy landscape, overall kinetics, and diffusion mechanisms associated with these defects. Our results show complex scattering mechanisms even for defects as simple as small vacancy clusters. Finally, in the last chapter, we discuss a local basin approach to managing low-barrier events in the kART. Kinetic Monte Carlo simulations become inefficient in systems where the energy landscape consists of basins with numerous states connected by very low energy barriers compared to those needed to leave these basins. As the system evolves state by state, it is much more likely to perform repeated events (so-called flickers) inside the

trapping energy basin than to escape the basin. Such flickers do not progress the simulation and provide little insight beyond the first identification of those states. Our local basin algorithm detects, on the fly, groups of flickering states and consolidates them into local basins, which we treat with the basin-auto-constructing Mean Rate Method (bac-MRM), a master equation-like approach based on the mean-rate method.

Keywords: Point defects, Diffusion, Iron, kinetic Monte Carlo, kART

Contents

List of Tables

List of Figures

List of Acronyms and Abbreviations

kART	The Kinetic Activation-Relaxation Technique
ARTn	The Activation-Relaxation Technique
KMC	kinetic Monte Carlo
TST	Transition State Theory
PES	Potential energy surface
eV	Unit of energy, the electron volt
K	Unit of temperature, the Kelvin
Å	Unit of distance, the Angstrom
NAUTY	No AUTomorphisms, Yes?
LAMMPS	Large-scale Atomic/Molecular Massively Parallel Simulator

Notations

ΔF	Difference of free energy
ΔE	A variation of internal energy
ΔS	A variation of entropy
k_B	Boltzmann's constant
T	Temperature
$\tilde{r}$	Effective frequency
E	Internal energy
F	Free energy
S	Entropy
r^*	Test frequency

Acknowledgment

I would like to thank several people for making the success of this thesis possible. First and foremost, I would like to express my sincere gratitude to my thesis advisor, Prof. Normand Mousseau. Normand is a constant inspiration to the entire research group, as he provides us with good advice and insightful guidance in all our projects. Normand is also the best advisor in the literary sense that one can hope for. His care for students goes far beyond our scientific work, and time and again he has given me invaluable advice and comforted me at many pivotal moments in my PhD career. Without his contribution and constant motivation, this work would not have been possible.

I would also like to thank the many collaborators I have had along the way. Prof. Fedwa El-Mellouhi, Prof. Othmane Bouhali, and Prof. Charlotte S. Becquart helped me carry out my first research project and provided tremendous support during the first three years.

Many thanks to my former trainer colleagues Dr. Simon Gelin, Dr. Sami Mahmoud, and Dr. Vincent Binette, who warmly welcomed me into Normand's group and provided me with the best learning conditions. Another thanks goes to recent colleagues, Dr. Jeffrey Roshan De Lile and Aynour Khosravi; the scientific discussions and exchange of ideas were sometimes tense, but they pushed me to do my best.

I thank the members of my dissertation committee, Prof. François Schiettekatte, Prof. Joerg Rottler, and Prof. Michel Côté, for the honour they gave me to serve as a jury member on my dissertation.

Finally, I would like to thank my parents for their unconditional love and support during the ups and downs of my life.

Introduction

Optimising material properties is a significant research challenge. In many industrial fields, materials with strong mechanical properties, high plasticity and high corrosion resistance are in demand. To improve these properties, it is essential to identify the factors that influence them. Point defects in metals can affect their physical and mechanical properties [35]. For example, point defects such as vacancies promote dislocation formation [58]. The subsequent evolution of the latter causes extreme plastic deformation in metals [161]. In contrast to vacancies, the presence of interstitial defects can increase the hardness of a material by impeding the mobility of dislocations, and thereby decreasing plastic deformation [45, 153]. Another mechanical property of materials, creep under applied stress, is characterised by the collective motion of individual vacancies or clusters [101, 161]. It is not just the mechanical characteristics that are impacted by point defects diffusion processes; the electrical ones are as well. For example, it has been demonstrated that the deformation of the Fermi surface caused by defects such as vacancies and extrinsic interstitials leads to different electrical resistivity in the two materials [47, 123].

Numerous studies have been carried out to describe the thermodynamic properties of metals in the presence of defects, including the chemical equilibrium characterised by the minimization of the Gibbs free energy (for the case when temperature and pressure remain constant), as well as the enthalpy and entropy of the formation of point defects in crystals. Due to the limitations of numerical and experimental approaches, many details of the kinetic evolution of these defects as well as their aggregation remain unclear.

Despite the research conducted in the last fifty years, there are still many obstacles to understanding and knowing the mechanisms that take place at the atomic level. The advent of the digital age now justifies the use of numerical simulation approaches that accurately and realistically represent the states and properties of matter. Numerical approaches would ideally model system evolution up to experimental time scales and with atomic-level descriptions. However, there is not yet a single method that fully covers atomic-level descriptions for experimental times. For example, ab initio approaches based on the solution of the quantum Schröedinger equation provide the best results in terms of electronic and atomic properties. On the other hand, finite element methods provide a more accurate representation of macroscopic and mesoscopic dynamics and properties, including mechanical, thermodynamic, and acoustic quantities. Currently, the combined application of several numerical methods provides a partial understanding of matter on long time scales and an atomistic description.

The study of diffusion, structure relaxation and defect aggregation processes in materials, in this work specifically in iron, requires the use of powerful multiscale numerical methods. Indeed, we will see that all these processes are distributed over several orders of magnitude, both spatially and temporally. It is essential to have tools that accurately describe energy levels and atomic configurations. At the same time, these tools must track the evolution of the system on experimental time scales.

The dissertation is organised as follows: The first three chapters (1, 2, and 3) are bibliographic chapters devoted to the description of the problem studied (the specific defects in materials) and the numerical methods used for its study. In the following chapters (4, 5 and 6), which have the form of articles, our results are presented. In chapter 1, we describe the different types of point defects that can occur in materials. The end of the chapter is devoted to the kinetics of these defects. Then, in chapter 2, the problem of activated processes (also called rare events) is put into context. The activated processes describe, among other things, the nature of diffusion of atoms and possible structural defects in solids. For this purpose, the theory of transition states is presented, which is currently one of the most important methods to treat activated processes efficiently and rapidly. Among the so-called

accelerated methods, the kinetic Monte Carlo method is described in detail in its original form; then an overview of the developments of this method during the last twenty years is given. In chapter 3 we will focus more on the method used in our studies, the kinetic ART (k-ART) method, an off-lattice kinetic Monte Carlo algorithm with on-the-fly catalog construction based on activation-relaxation technique nouveau (ARTn). ARTn is a powerful open-ended saddle search method that fully accounts for the long-range elastic effect. In chapter 4, which presents the results of the first article, we investigated the pressure effect on carbon diffusion in the grain boundary of $\alpha-$iron to understand the evolution of heterogeneous materials in which variations in local pressure can alter carbon diffusion through the material. In chapter 5, which contains the results of the second article, we studied the diffusion mechanism of vacancy clusters (from one to eight vacancies) in crystalline $\alpha-$iron. Finally, in the last chapter (chapter 6), the application of the local basin approach to the kinetic activation-relaxation technique is presented in detail. The thesis is concluded with a conclusion summarising all the innovations as well as the perspectives of our research work.

Chapter 1

Point defects in materials

1.1. Introduction

Crystals are, in reality, never perfect and always contain defects. Defects in solids are broadly divided into two categories: (i) point defects (zero-dimensional defects) such as vacancies, interstitials, etc., and (ii) extended defects (ordered in one, two, and three dimensions) such as dislocations, grain boundaries, voids, etc. In this chapter, and in the dissertation in general, we focus exclusively on the study of point defects. In particular, this thesis focuses only on the study of point defects in $\alpha-$iron. Point defects play an important role in maintaining the macroscopic properties of materials, especially when they are subjected to irradiation that multiplies the presence of vacancies and interstitials. This chapter provides a concise overview of the different types of point defects and their kinetics, as well as the experimental and numerical methods used to study defect evolution.

1.2. The different types of point defects

In the literature, point defects are classified according to their atomic nature, i.e., intrinsic and extrinsic defects, or according to their configuration, i.e., when atoms are missing, one more atom is present, or an atom of a different kind replaces another in the lattice. We will use the second classification criterion, which divides the point defects into three types: vacancies, interstitial atoms and substitution atoms.

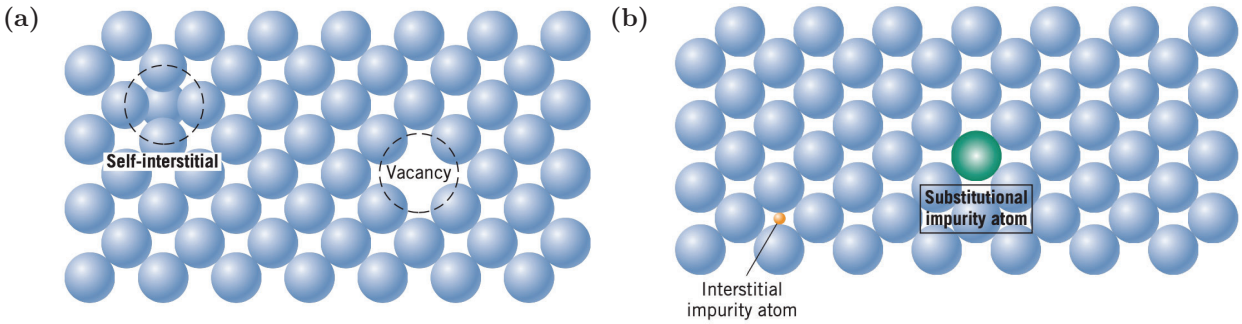

Fig. 1.1. Schematic illustration of (a) intrinsic and (b) extrinsic point defects. The intrinsic defects are the vacancy and the self-interstitial, which are a crystalline site unoccupied and one more atom in the lattice of the same type as those of the crystal, respectively. The extrinsic point defects are the substitutional atoms (in green in figure b) and the interstitial atoms (in orange in figure b), both different from those of the crystal [19].

1.2.1. Vacancies

The vacancy is simply an unoccupied crystalline space, as seen in Fig.1.1a. At absolute zero temperature (0 K), all atoms forming the crystal of a metal are in their crystalline sites. Vacancy defects can occur in any crystalline solid; in fact, they are inherent. Any material whose temperature is above absolute zero can contain vacancies. As the temperature increases, the number of vacancies increases exponentially. Their concentration can be expressed as $N_v N e^{-\frac{E_f}{k_B T}}$, where N is the number of atoms in the crystal, E_f is the formation energy of a vacancy, T is the temperature of the solid, and k_B is the Boltzmann constant. The presence of a vacancy in a material does not cause much distortion of the crystal because the neighboring atoms of the vacancy tend to leave their crystalline site slightly to approach the vacancy, but they will not try to take the place of the vacancy.

1.2.2. Interstitial

The interstitial is an atom located in an irregular site of the crystal, also called interstitial, hence the name of the defect. In metals in general, and in the most compact metals in particular, the atoms are larger than the interstitials, which means that the presence of interstitial sites is unlikely compared to vacancies. Indeed, for interstitial sites to be incorporated into the network, large distortions must occur.

Depending on the nature of the interstitial, two cases can occur: an intrinsic interstitial (Fig.1.1a), when the atom belongs to the same species as the atoms forming the crystal (a pure metal or a simple alloy), or an impurity (Fig.1.1b), when the interstitial atom belongs to a different species than the atoms of the crystal. Logically, the atoms that remain in the interstitial spaces are smaller than the atoms that form the metal lattice (such as hydrogen, oxygen, or carbon).

1.2.3. Substitutional atom

Substitution atoms, as their name implies, are impurities that replace an atom of the original network. Fig.1.1b illustrates the substitution defect. Unlike the interstitial atoms, the substitution atoms are generally the same size or different (either larger or smaller) than the atoms of the network. Depending on the size of the substituted impurity atom, the neighboring atoms may remain either in tension or in compression. In ordered systems with more than one atomic species, substitution leads to the appearance of antisites, atoms that are different in nature than expected and dictated by the order of the structure.

1.3. Diffusion kinetics of defects

Understanding diffusion in any metal begins with identifying the mechanism by which defects migrate through the host lattice. A diffusing species can only occupy certain equilibrium lattice sites in an ordered crystal lattice. Microscopic diffusion occurs when a defect completes numerous jumps between these sites. The elemental jumps in this series can be diverse, but we limit ourselves here to the typical jumps in metals, especially in $\alpha-$iron.

1.3.1. Diffusion by vacancy

An atom can diffuse by exchanging its position with the vacancy, resulting in self-diffusion (see Fig.1.2a). On the other hand, an impurity occupying a substitution site can also use this mechanism to diffuse. This is called vacancy-assisted diffusion. However, the mechanism of vacancy diffusion is very subtle and depends strongly on the structural and electronic

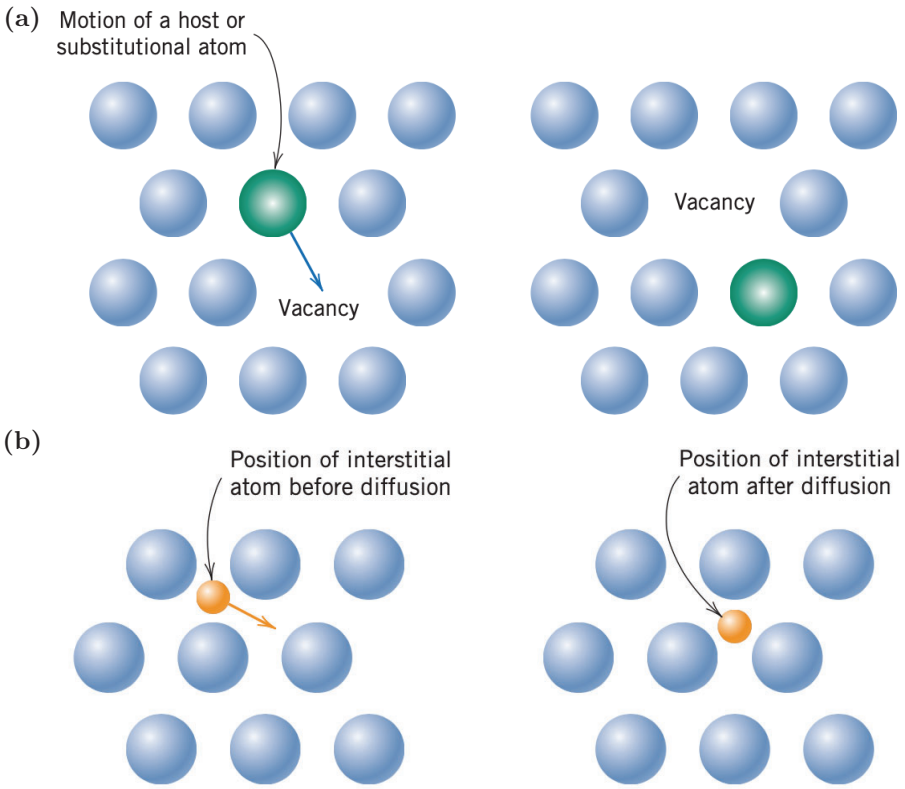

Fig. 1.2. Schematic representation of diffusion from (a) the vacancy and (b) the interstitial. At the vacancy, an adjacent atom (in green) jumps to fill it, and thus the vacancy has diffused into the original site of that atom. The interstitial atom (in orange) jumps from one interstitial site to another neighbor [19].

environment of the vacancy. This mechanism may be more advantageous in exchanges between the vacancy and its first or distant neighbor. For this to occur, the remote atom must have sufficient energy to break its bonds with its neighbors and create the distortions that allow it to migrate. When divergences are present, this mechanism becomes more complicated, since a divergence has the possibility of dissolving into two vacancies, rotating as a non-rigid dumbbell, or moving directly.

1.3.2. Diffusion by interstitials

Some atoms move through the interstitial region without interacting with regular sites in the crystal structure (see Fig.1.2b). These may be self-interstitial atoms or impurities occupying the various possible interstitial sites in the crystal. Since metals are generally very compact, diffusion of an interstitial site leads to numerous distortions of the lattice.

The high compactness of metals (atomic packing factor is 68 and 74% for BCC and FCC crystal structure, respectively) also means that there is not enough interstitial space for the extra atom, which is why interstitial site diffusion in metals often corresponds to dumbbell motions, i.e., motions in which a pair of atoms share the same crystal site. In addition, interstitial diffusion in most metals is generally much faster than vacancy diffusion because there are more interstitial sites than crystal sites.

1.4. Determination of point defect properties

To study and describe the diffusion of point defects in crystals, some features are important. First, one must know the defect formation energy and the defect migration energy. The first quantity, i.e., the defect formation energy, is the energy required to create a defect (a vacancy or interstitial) in a perfect crystalline structure. The formation energy is important for determining the defect concentration in the solid. In some cases, the defects could be sufficiently concentrated to have a non-negligible chance of interacting. Therefore, the defects could diffuse into groups, and these diffusion mechanisms could become important. The second quantity, i.e., the migration energy, is the difference in energy between the equilibrium configuration and the saddle point along the migration path.

1.4.1. Experimental study of defects

The study of defects begins with the observation and characterization of defects. This involves determining the nature of the defect, which is initially completely unknown. Information about a point defect can be obtained by spectroscopic methods such as electron paramagnetic resonance (EPR) [131], infrared spectroscopy (IR) [126], deep-level transient spectroscopy (DLTS) [80], or photoluminescence [48]. For studies at high temperatures, other methods are required, such as positron annihilation spectroscopy (PA) [52]. In positron annihilation spectroscopy, the lifetime of the positron injected into the material is determined by detecting gamma particles produced during electron-positron annihilation. The positron

injected into the material is degraded to thermal energy within a time interval of a few picoseconds by ionization and excitation of the material [113]. A longer lifetime of a positron is an indication of the presence of a defect (vacancy or dislocation), since the position is trapped there due to the lower electron density and thus the probability of annihilation of an electron is lower. Fig.1.3 shows the difference between the densities of positrons in a perfect crystal and a crystal with a vacancy in $\alpha-$iron. However, the PA method is limited to the detection of neutral or negatively charged vacancies. Extensive defects are detected by structural analysis of the material by X-ray diffraction [151] or transmission electron microscopy (TEM) [63]. On the other hand, it is more difficult to identify the true nature of certain point defects using these methods alone. The most effective method remains identification based on their optical or electrical signature.

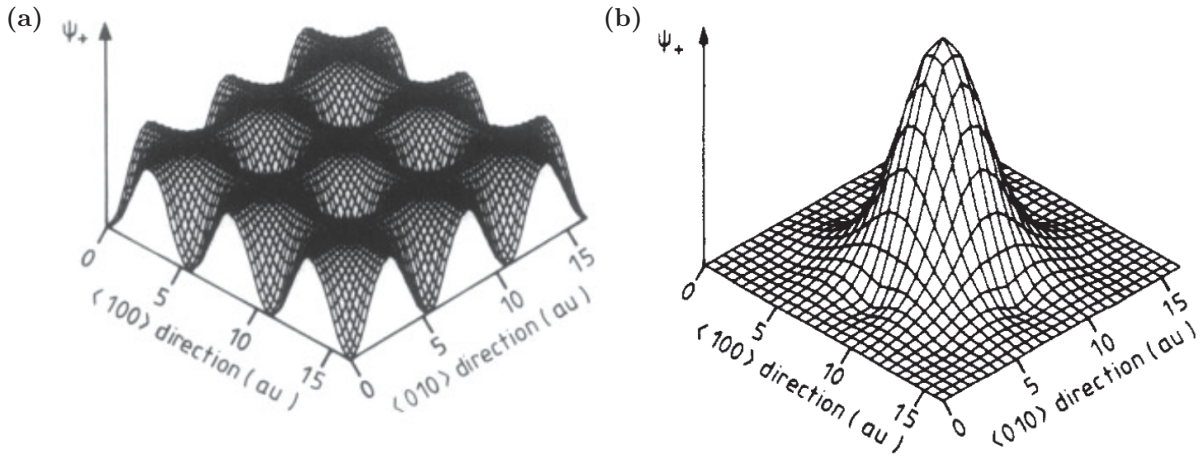

Fig. 1.3. Bloch state positron density in BCC Fe, and (b) Vacancy trapped positron density in BCC Fe [113].

Identification of defects is most effective by combining several methods, including magnetic resonance spectroscopy [5] and the study of localized vibrational modes [71]. First-principles calculations are a very efficient method for identifying defects [74]. Quantum calculations yield results comparable to those obtained by spectroscopy in terms of the structure and formation energy of defects.

Defect control first begins by studying the thermal stability of a complex defect in annealing experiments. A series of isothermal anneals are performed to cause either dissociation of

the defect or its migration. This provides a better understanding of the defect so that it can be controlled by generation or dissociation to improve the performance of the materials.

For diffusion measurements, a distinction is made between direct experiments with radioactive tracers [154] and indirect experiments such as induced magnetic anisotropy [34]. The migration energy can be determined by calculating the slope of the Arrhenius curve [122] (diffusion as a function of the inverse of temperature), which requires measurements at different temperatures. In the context of an Arrhenius curve, the diffusion coefficient is the measure of the mobility of a diffusing species and is expressed as $D = D_0 e^{-\frac{E_m}{k_B T}}$; where D is the diffusion coefficient of the species, D_0 is a pre-exponential factor, and E_m is the migration energy of the mechanism. Experimental measurements at different temperatures, therefore, allow us to find E_m.

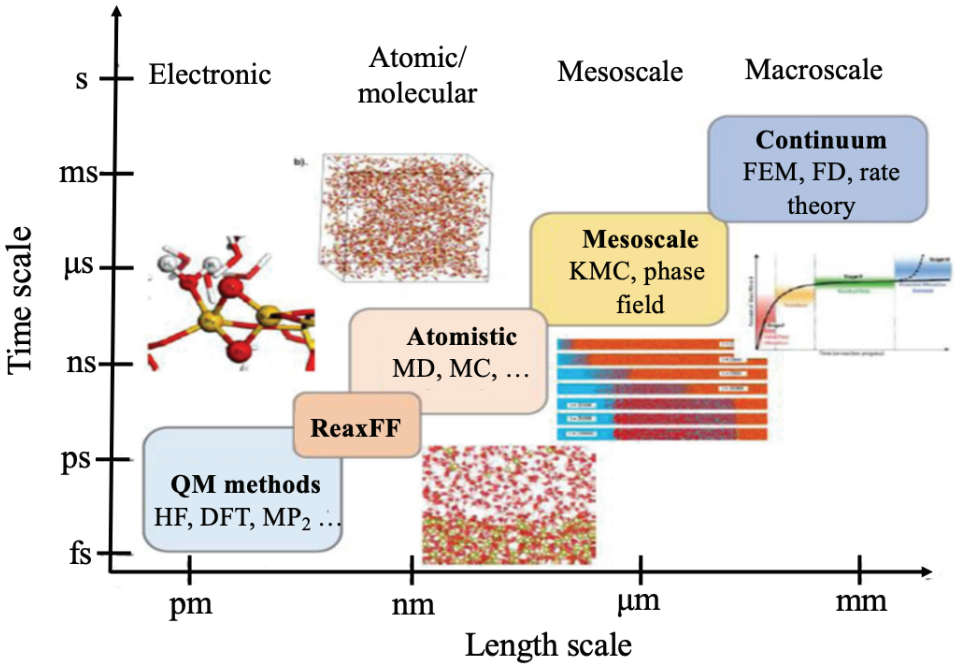

Fig. 1.4. Schematic representation of the multi-scale simulation method [39].

1.4.2. Numerical study of defects

The most reliable numerical methods for calculating defect properties are based on first-principle calculations, which are generally based on density functional theory (DFT) [59].

The first-principle calculations provide a good estimate of the defect formation energy. These methods are also used to study defect kinetics. However, due to their cost, these methods are limited in their ability to map energy landscapes, and most work is limited to finding a transition state between given initial and final states based on an initial guess for the connection path. Only the path closest to the initial guess is explored, leaving other possible paths unexplored. This can be problematic in complex energy landscapes where multiple nontrivial but relevant paths may exist. In addition, the methods of DFT are too expensive to apply to large systems or to enable extensive sampling.

To circumvent the constraint imposed by the limited size of the system and CPU time, there are two approaches based on approximate methods: molecular dynamics (MD) [60] and kinetic Monte Carlo methods (KMC) [146]. Standard molecular dynamics (MD) uses the interaction potential to calculate forces on individual atoms or molecules and uses Newton's equations to directly simulate motion. Despite its simple principle and efficiency in accurately determining atomic trajectories, molecular dynamics is subject to certain limitations. First, the quality of the atomic potential affects the quality of the results. It should also be noted that some potentials are optimized for certain problems or for certain precise atomic compositions. In addition, this type of simulation generally does not adequately account for the influence of the electronic structure of the material. As soon as the coordination of the diffusing atoms deviates too much from the crystalline state, the empirical potentials cannot represent well the interaction between atoms. The classical MD cannot predict atomic configurations or migration energies and barriers. However, some more computationally intensive potentials can approximate these electronic correlations. Similarly, molecular dynamics can be coupled with an ab initio algorithm [65, 110] to correctly calculate the interactions between atoms. However, the increase in precision limits the number of atoms to be used and increases the cost and the computation time. Second, in this type of simulation, the time step must be small enough to ensure numerical stability, which is of the order of one to two femtoseconds ($1{,}2 \times 10^{-15}$ s). To achieve simulation times on the order of milliseconds, a sequence must be executed in billions (10^{12}) of steps, which is

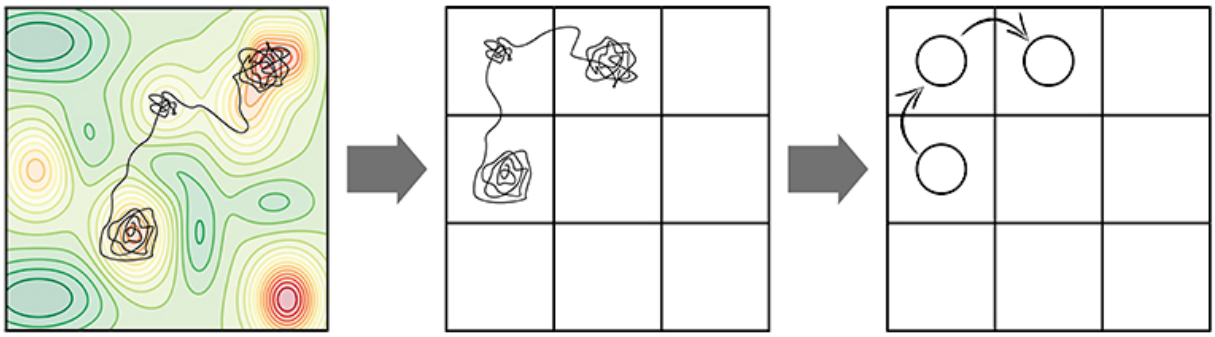

Fig. 1.5. Coarse-grained representation of a MD trajectory in a Markov chain. (Left) Oscillatory motion is also included, and the MD trajectories spend most of their time around the local minimum. (Middle) Coarse-grained representation of the minima of PES in positions on a suitably defined lattice. Each grid position represents the local minima in PES. (Right) Coarse structuring of the MD trajectory into a Markov chain of discrete jumps between the local minima [4].

very computationally expensive and difficult to achieve even with supercomputers that have large numbers of processors. Time limitation is a problem in describing the effects of diffusion of point defects in materials, since several of the properties directly affected by the motion of these defects can be observed on scales larger than a microsecond. The current trend is to accelerate dynamic methods to quickly find activated events and improve phase space sampling. Examples include molecular dynamics accelerated by the temperature of the Voter [29, 144], hyperdynamic method [143], parallel replica dynamics [145], self-directed dynamics [157], and finally thermodynamically biased dynamics [79]. So far, the application of these accelerated dynamical methods has been limited to simple and well-known systems with a limited number of transition states.

The kinetic Monte Carlo simulation method attempts to overcome the time constraints by exploiting the fact that the long-term dynamics of this type of system typically consists of a series of diffusion jumps from state to state (see Fig.1.5). Instead of following the trajectory through each vibrational period, these state-to-state transitions are treated directly, as we explain in detail in chapter 2. The result is that KMC can reach much longer time scales, typically seconds and often well beyond. In a standard KMC implementation, a catalog of all possible transitions and their rates is provided at the beginning. Then, in each KMC step, a transition path is randomly selected from the catalog with a probability proportional

to its rate, time is updated, the system is placed in the new state, and the rate list must be updated. If the basic assumptions of KMC are satisfied, namely that the first escape time from a state is exponentially distributed, the statistics obtained from KMC simulations can be as accurate as those obtained from MD.

1.5. Conclusion

In this chapter, we have briefly introduced the different types of point defects in materials and their diffusion mechanisms. We have also briefly discussed different types of experimental and multiscale numerical approaches to study the defect properties. In a multiscale modeling approach, a chain of simulation techniques is formed, ranging from high-fidelity DFT calculations for the smaller scales to KMC methods for approximated simulations at higher-order scales. In the next chapter, we discuss the activated processes and the theory of transition states and present the standard KMC algorithms in detail.

Chapter 2

Theory and numerical approaches

2.1. Introduction

This chapter deals with the activated processes (also called rare events) that characterize the kinetics of a system, i.e., the time scale on which these processes can be observed. These include, for example, defect diffusion and impurities trapped in solids, atomic reorganization in a material after damage, and the time scale associated with the relaxation mechanisms of a material. To characterize these phenomena, it is necessary to have a theoretical model which is provided by the transition state theory that we present. Transition state theory conceptualizes the kinetics of a system by discretizing the temporal evolution into a series of events. The kinetic Monte Carlo (KMC) method is a numerical method that uses transition state theory to directly simulate the structural evolution of the system through a sequence of activated transitions and estimate the elapsed time between each transition. In this chapter, we present the original kinetic Monte Carlo method. However, we see that the first versions of these KMC methods were limited. We conclude this chapter by reviewing the progress of the KMC method to show how the initial limitations of this method have been overcome.

2.2. Activated processes

An activated process is a physical transformation (chemical reaction, diffusion of an atom in a solid, etc.) that requires a certain amount of free energy. This process is also called

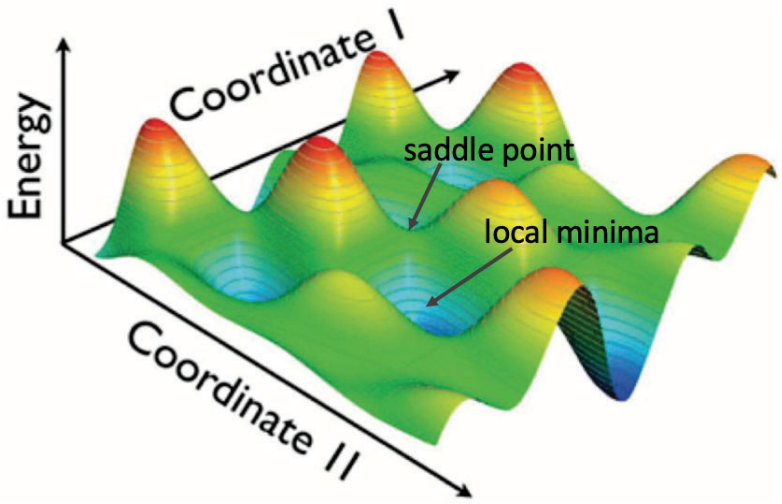

Fig. 2.1. Three-dimensional illustration of a potential energy surface represented in two dimensions (dependent on 3N+1 variables) with first-order saddle points [105].

a rare event because the barrier associated with it is usually much larger than the thermal energy available at a given temperature. In order to deal with the problem of activated processes, one must first be able to evaluate the free energies of the various configurations of a system. Let us dwell on the internal energy of the system. The potential energy of a system is calculated from the interactions between the particles of the solid and depends only on the position of these particles and the spatial dimension of the solid under consideration. The potential energy surface (PES) is the set of possible configurations; therefore, at a given time, the system is at a point of PES (see Fig.2.1). The potential energy is a function with 3N variables, where N is the number of atoms in a 3-dimensional space. Each stable configuration is represented there by a set of local minima connected by saddle points, called saddle points. All elements in nature tend to minimize their Gibbs free energy, minimize their energy, and maximize their entropy to achieve dynamic equilibrium. The same is true for atoms and their rearrangements within structures, and PES describes the possible or improbable configurations according to their energy levels. Most of the time, a system is in a local minimum at PES. Atomic oscillations due to the contribution of thermal energy allow the system to explore the surface around a given minimum until a series of fluctuations allow the system to cross a saddle point and reach a nearby minimum.

The amount of internal energy required during a transition is called the activation energy (ΔE) and is defined by the difference between the potential energy at the initial minimum and the saddle point. In addition, the entropy contribution (ΔS) can be calculated by evaluating the integral of the path between these two points. These activation energies and the entropy contribution, and more generally the notion of activated process, define the kinetics of a system. Indeed, they characterize the time scales associated with each transition. In the next section, we will see that a transition rate can be assigned to the different activated processes based on the transition state theory (TST) and some basic assumptions. This amount of free energy, $\Delta G = \Delta H - T\Delta S \approx \Delta E - P\Delta V - T\Delta S$, which is essential during a transition, formally separates two states of matter so that a transition can be described: by a stable initial state (minimum energy), an unstable saddle point (transition state), and a stable final state. The notation ΔH is the activation enthalpy and is defined as the difference between the enthalpy of the transition state and that of the initial minimum, and ΔV is the activation volume, defined as the volume of a material involved in the process of overcoming the energy barrier.

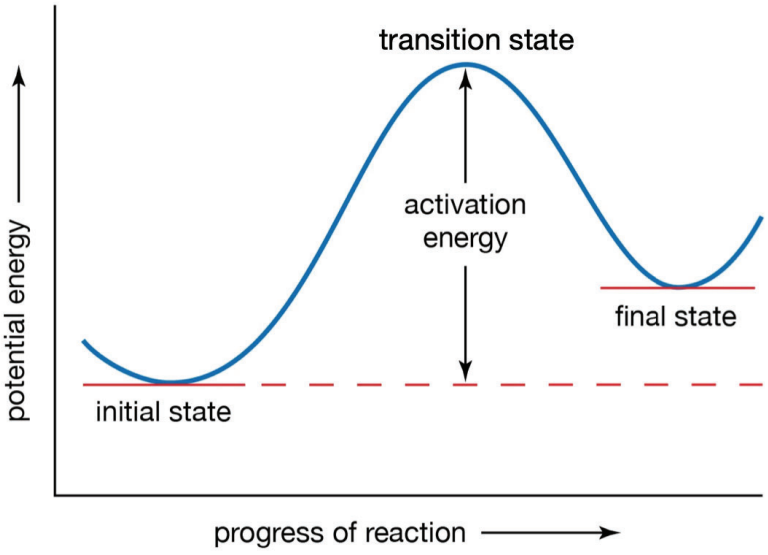

Fig. 2.2. A two-state system illustrating the definition of the transition state theory rate [78].

2.3. Transition State Theory (TST)

Transition state theory (TST) was developed by Henry Eyring [43] in 1935 to understand and describe activated processes by calculating the rates associated with transitions on a potential energy surface. The basic concept of TST divides the PES into two adjacent regions, each associated with a local minimum and sharing at least one common saddle point (see Fig.2.2). Assuming that this saddle point is first order, this separation is a (3N-1) dimensional hyperplane. The last dimension, called the reaction coordinate, connects the initial, saddle point, and final states. From a theoretical point of view, the transition rate is defined by the flux crossing the hyperplane. The assumptions of TST are:

(1) a first-order saddle point exists.

(2) the different transitions available are uncorrelated.

(3) vibrational energies are negligible compared to activation energies.

With these assumptions, Vineyard [141] showed that the transition rate could take the following form:

$$\Gamma = \tilde{r} \exp\left[\frac{-\Delta F}{k_B T}\right]; \tag{2.3.1}$$

where, ΔF is the amount of free energy that must be supplied to move from one local minimum to another (called the activation free energy), T is the absolute temperature, k_B is the Boltzmann constant, and $\tilde{r}$ is an effective frequency that depends on the atomic vibrations in the region of the initial minimum and the saddle point of PES. Based on the thermodynamic identity $F = E - TS$, the equation can be reformulated as follows:

$$\Gamma = \tilde{r} \exp\left[\frac{\Delta S}{k_B}\right] \exp\left[\frac{-\Delta E}{k_B T}\right]; \tag{2.3.2}$$

$$\text{or, } \Gamma = r^* \exp\left[\frac{-\Delta E}{k_B T}\right]; \tag{2.3.3}$$

where, $r^* = \tilde{r} \exp\left[\frac{\Delta S}{k_B}\right]$ is the test frequency corresponding to the atomic vibrations in the regions of the initial minimum and the saddle point, but also to the entropic contributions,

ΔE is the activation energy defined by the difference in potential energy between the initial minimum and the saddle point, and ΔS is the entropy change between the initial minimum and the saddle point. The equation 2.3.3 allows us to separate the entropic contributions from the potential energy contribution. Recall that for a crystal with N atoms in a 3−dimensional space, the number of degrees of freedom associated with the crystal is 3N and the potential energy is a function with 3N variables. Despite this separation, the calculation of the test frequency requires the evaluation of the path integral over the entire PES between the initial minimum and the saddle point, which is numerically tedious. Nevertheless, based on the assumption of weak oscillations, Vineyard was able to approximate the potential energy near the initial minimum and the saddle point quadratically (by a series expansion) and thus derive an expression for the test frequency r^*.

This test frequency is defined by the ratio of the products of the modal frequencies (ν_i) of minimum vibration and the modal frequencies (ν') at the saddle point deprived of the negative frequency such that:

$$r^* = \frac{\prod_{i=1}^{3N} \nu_i}{\prod_{i=1}^{3N-1} \nu_i'}; \tag{2.3.4}$$

Using the underlying assumptions of TST and that of low vibration, the calculation of the transition rate associated with an activated process becomes more affordable numerically, and the Harmonic Transition State Theory (hTST) is expressed as that :

$$\Gamma = \left(\frac{\prod_{i=1}^{3N} \nu_i}{\prod_{i=1}^{3N-1} \nu_i'} \right) \exp\left[\frac{-\Delta E}{k_B T} \right]. \tag{2.3.5}$$

For crystalline solids, it is common to associate the test frequency (r^*) with a constant of the order of the mean vibrational frequency (for crystalline iron, for example, the value $10^{13}\ s^{-1}$ is commonly used) to save further computational time. The calculation of the activation energy for a given process depends on the energy levels of the initial minimum and the saddle point. However, the calculation of these two energy levels is not always

the main problem. Indeed, the identification of the configuration of the saddle point can sometimes elude us. In the next section, we present the original kinetic Monte Carlo method, which over the years, has become one of the most efficient, versatile, and important numerical tools for studying the kinetic and thermodynamic evolution of a solid.

2.4. The kinetic Monte-Carlo method

The kinetic Monte Carlo method (KMC) is a numerical method that allows the structural evolution of the system to be simulated directly by a sequence of activated transitions and the elapsed time between each transition to be estimated. By focusing on rare events and neglecting atomic oscillations, it is possible to simulate structural evolution on larger time scales than with more traditional methods. The algorithm presented by Bortz et al [17] in the 1970s, called the "n-fold way" is the basic algorithm of most kinetic Monte Carlo methods developed to date, some of which are presented in the next section. This algorithm allows to reproduce stochastically a sequence of activated events and to estimate a temporal duration of Δt between each simulation step.

If we want to interpret the dynamics and kinetics of the Monte Carlo method, we need to discretize time so that two processes cannot occur simultaneously, and then determine a characteristic "time step", the dwell time. To determine the dwell time, we define the process of counting the number of events during a given time t by the random variable N(t), which follows a Poisson distribution with parameter $R_{i\hookrightarrow j}$t. It is assumed that each event admits a unique transition rate defined by $R_{i\hookrightarrow j}$ to get from state i to state j, and that the rate associated with each of the transitions does not depend on the transition performed to get to the current state (no correlation between events). The kinetic Monte Carlo method is used in the context of TST such that all of these assumptions are satisfied. The probability of observing a transition between an initial state i and a state j n times during a time t is then given by:

$$P_{i\hookrightarrow j}(N(t) = n, t) = \frac{(R_{i\hookrightarrow j}t)^n}{n!} exp(-R_{i\hookrightarrow j}t) \tag{2.4.1}$$

By definition, the exponential law describes the time interval between events in a Poisson process. Let $p_i(t)$ be those independent and identical random variables corresponding to the time interval between two transitions of the Poisson process. Then the probability density of each p_i is given by:

$$\forall t \geq 0; f(p_i(t)) = R_i^{tot} exp(-R_i^{tot} t) \tag{2.4.2}$$

with $R_i^{tot} = \sum_{j=1}^{N_i} R_{i \hookrightarrow j}$ and N_i corresponds to the number of accessible transitions in state i.

Moreover, by definition, the dwell time in state i is given by the first moment of the distribution of p_i:

$$\Delta t_i = \int_0^\infty t f(p_i(t)) dt = \frac{1}{R_i^{tot}} \tag{2.4.3}$$

To stochastically reproduce the expected value of the random variable p_i at time t_i in the KMC algorithm, a random number μ uniformly distributed over [0; 1[is declared, and the KMC dwell time is thus defined as:

$$\Delta t_i^{KMC} = -\frac{ln\ \mu}{R_i^{tot}} \tag{2.4.4}$$

The ratio between the rate of the chosen transition and the sum of the rates of the accessible transitions is the relative probability associated with that transition and is defined by:

$$P_{i \hookrightarrow j} = \frac{R_{i \hookrightarrow j}}{R_i^{tot}} \tag{2.4.5}$$

The transition performed by the KMC algorithm is determined by constructing the rate of cumulative ascending (or descending) transition such that $R_{i;k} = \sum_{j=1}^{k} R_{i \hookrightarrow j}$ ($R_{i;0} = 0$ by definition) for k up to N_i, the number of transitions accessible from state i. Generating a uniformly distributed random number ν on [0; 1[such that νR_i^{tot} determines transition k as the one to be executed if the condition $R_{i;k-1} < \nu R_i^{tot} \leq R_{i;k}$ is satisfied.

In summary, the kinetic Monte Carlo algorithm involves the following steps:

(1) Reading the initial state i of the system.

(2) Identify the list of N_i possible transitions of the system from the current state i to reachable states j.

(3) Calculate the transition rates $R_{i \hookrightarrow j}$ for all N_i transitions of the system from state i to state j.

(4) Construct the ascending cumulative transition rate, $R_{i;k} = \sum_{j=1}^{k} R_{i \hookrightarrow j}$. We also derive the total transition rate, $R_{tot} = R_{i;N_i}$.

(5) Generate a random number ν_1 uniformly distributed over the interval]0, 1].

(6) Update the simulated time by adding $\Delta t = -\frac{ln\ \nu_1}{R_{tot}}$, which should correspond to the dwell time in state i, with stochastic effects mimicking a Poisson process.

(7) Generate a second random number ν_2 uniformly distributed over the interval]0, 1].

(8) Choose the transition k from the relation $R_{i;k-1} < \nu_2 R_{tot} \leq R_{i;k}$ and execute the transition that leads to the new configuration.

(9) Update the current state $k \rightarrow i$.

(10) Return to step 2.

On the other hand, the kinetic Monte Carlo method in its original form was limited by three aspects:

(1) It was only able to deal with lattice problems.

(2) It required prior creation of a catalog of transitions.

(3) It did not consider the possible effects of elastic deformations.

2.5. Review of kinetic Monte-Carlo methods

In 1975, Bortz et al [17] were the first to apply the kinetic Monte Carlo method to characterise the time evolution of Ising spin systems using the "n-fold way" algorithm. Motivated by the work of Bortz, Voter et al. [142] developed an algorithm in 1986 to characterise the diffusion of the rhodium cluster on the Rh(100) surface. Most of the KMC methods developed up to 2000 were direct applications or derivatives of Voter's algorithm. For example, Maksym et al. [91] proposed a KMC algorithm based on the use of conditional probabilities

favouring certain transitions of interest, aiming to simulate the growth of gallium arsenide GaAs by molecular beam epitaxy (MBE) with KMC, as did Barnett et al. [8] used KMC to simulate the growth and reconstruction of the silicon (001) surface during MBE; Lu et al. [87] simulated the kinetics and distribution of chain length during radial polymerization; Wang et al. simulated the growth of the copper (100), (110), and (111) facets and introduced the premises of possible correlation support by redefining specific probabilities [150].

In the 2000s, the first advances were made to remove one, two, or all of the limitations of the original KMC method. For example, in 2001, Henkelman and Jónsson [57] developed the first off-lattice KMC algorithm by combining an open saddle point search method (called the dimer method [56]) with the standard KMC algorithm to simulate the diffusion of aluminum (Al) on the Al(100) surface. At each KMC step, 25 open-ended saddle searches were initiated to generate an event list. Although the number of searches was too small to ensure that all events were found, this work still identified new extended low barrier events that significantly altered the growth kinetics. The drawback of this approach is that there is no transition catalog. Indeed, at each KMC step, the information about the previous transitions is lost, making the approach costly and numerically weak. In the following years, several approaches were introduced to reduce the computational cost of off-lattice KMC simulations by introducing a cataloging approach.

In 2005, Trushin et al [137] proposed the self-learning kinetic Monte Carlo method (SLKMC), which is restricted to two dimensions and partially off the lattice. The position of the atoms is not restricted to an arbitrary lattice, but the algorithm for finding the saddle point is "closed" because they use a model to identify the different face-centered cubic (fcc) sites of the potential final local minima. However, by identifying the different configurations with binary keys, they can create a catalog of reusable transitions. This method allows the study of more complex environments and, more importantly, the inclusion of a larger area in the barrier calculation beyond the standard first and second neighbor shells.

In 2008, El-Mellouhi et al. [40] developed the kinetic activation-relaxation technique (kART), an off-lattice method with the ability to generate catalogs on-the-fly that overcomes

all three limitations of the kinetic Monte Carlo algorithm. By coupling activation-relaxation technique nouveau (ARTn) [7, 88, 92], an open search method, with NAUTY [97], a topological classification tool, kART associates local graphs with a unique event list that is generated when new topologies are identified. Rather than being limited to predefined lattice positions, kART allows event catalogs to be generated for any environment, even completely unordered ones. At each KMC step, all relevant generic events are fully reconstructed and converted into specific events to account for all geometric rearrangements due to elastic short and long range deformations.

In the last decade, several other off-lattice or near off-lattice approaches have been proposed, with or without a catalog. Xu et al [158, 159] developed the Self-Evolving Atomistic Kinetic Monte Carlo (SEAKMC) method based on an initial version called adaptive Kinetic Monte Carlo (aKMC) [160]. The SEAKMC method performs saddle point searches only in areas of particular interest, which it calls active volumes. Active volumes are essentially defective environments within the simulation box. Compared to kART, both SEAKMC and kART provide similar results; however, the SEAKMC method is faster in simpler environments such as recombination of a Frenkel pair [107], while the kART method is more flexible in dealing with complex materials [9, 14].

2.6. Conclusions

We have presented the problem of activated processes, which is elegantly approached and treated by the transition state theory (TST). Moreover, the original KMC method is perfectly suited to determine the physical quantities within this theory by their form. Most methods dealing with activated processes use sophisticated methods to characterize saddle points, such as nudged elastic band method [124], the dimer method [56], the string method [152], the eigenvector method [77], the inter minima jump method [51], and global reaction mapping method [108]. Most saddle-point search methods that characterize rare events using potential energy require prior knowledge of the start and end configurations. In many cases, we do not have that knowledge. In other cases, we want to find out what the

set of configurations adjacent to an initial configuration is, and characterize the transition state that separates them. The activation-relaxation technique nouveau (ARTn) [7, 88, 92] is an open-ended saddle method that allows us to describe the energy landscape near a local minimum and to warp a configuration on a path near the lowest energy path to a saddle point. It uses the Lanczos algorithm to find the eigendirection of the smallest eigenvalue of the Hessian of potential energy and steer the configuration in that direction to reach the saddle point. It is the first algorithm to find saddle points in complex, high-dimensional systems. The historical review of the progress of KMC methods in the last 30 years serves as an introduction and perspective for the next chapter, where the kinetic ART (or kART) method is presented.

Chapter 3

Kinetic activation and relaxation technique

3.1. Introduction

The kinetic activation-relaxation technique (kART) [13, 40, 67, 103, 104, 136] is an off-lattice kinetic Monte Carlo (KMC) method with an open-ended search for saddle points and on-the-fly cataloging. Following the standard KMC method, the kART method uses a catalog of events to calculate the exit rate from a local minimum and drive the simulation clock. However, there are three fundamental differences from the standard KMC method. First, instead of geometry, a topological classification of the local environment is introduced so that the algorithm is not bound to predefined lattice positions. Second, the catalog is not fixed at the beginning of the simulation; enabled events are added to the catalog during the simulation as new local environments are visited. Third, all relevant events, including the initial minimum and saddle points, are fully relaxed at each step to ensure that short- and long-range elastic and configurational effects are accurately accounted for. In this chapter, we will discuss the algorithmic and implementation details of kART in detail.

3.2. Basic algorithm of kART

Before we go into detail, it is useful to show the most important steps of the algorithm (see also Fig.3.1).

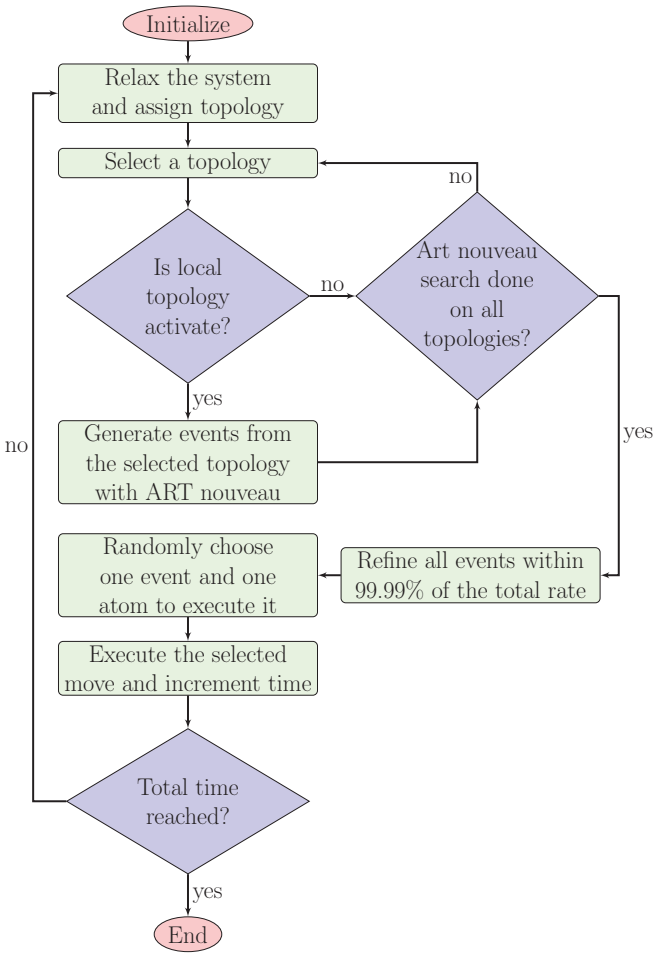

Fig. 3.1. Flowchart of the implementation of kART.

At each kART step, the local environment of each atom is characterised by its local topology, which is evaluated using NAUTY [97, 99], a topological analysis library developed by McKay. All atoms exhibiting a given topology are assumed to be associated with the same list of generic events.

If the topology is known, the generic events associated with it are recovered from the catalogue and inserted into a KMC tree; otherwise, event searches for all newly identified topologies are started using ART nouveau [7, 88, 92], an efficient algorithm developed by Normand Mousseau et al. to search for open-ended transition states. Each event is classified by initial minimum, saddle configuration, and final state topologies and stored in the catalogue.

Once the event catalog is updated, the generic events are ordered as a function of their rate, which is defined using transition state theory as $r_i = \nu_0 e^{-\frac{E_b}{k_b T}}$, where ν_0 is a fixed prefactor fixed at 10^{13} Hz, and E_b, the activation energy for event i, defined as the energy difference between the transition state and the initial minimum.

Events within 99.99% of the total ascending cumulative rate are fully reconstructed and converted to specific events to ensure that elastic and configurational effects are accurately accounted for. At this point, following Bortz et al. [17], the elapsed time until the next event is calculated as $\Delta t = -ln\ \mu / \sum_i r_i$, where μ is a random number in the interval [0,1[] and r_i is the rate associated with event i. The clock is advanced, an event with the correct weight is selected, and the atoms are moved accordingly after a geometric reconstruction.

Each of these steps, of course, involves a number of elements, which we describe in the following sections.

3.3. Topological classification

The topological classification of the local atomic environment is a crucial step in kART, as it helps to (i) categorize complex and off-lattice atomic arrangements, taking into account long- and short-range elastic interactions, and (ii) build a reusable event catalog.

Atomic topologies for a given local configuration are computed using NAUTY. This program is able to quickly identify a graph by its automorphism group, give it a canonical label (characteristic of the group), and recognize its symmetries. Fig.3.2 shows how NAUTY can find the correspondence between two graphs belonging to the same automorphism group. The nodes of these two graphs are ordered by NAUTY in the same way. Since in kART each node of the graph corresponds to an atom, this ordered list allows us to apply the displacements associated with each of the atoms during an activated event.

To identify the topology associated with an atom in the system, Kinetic ART proceeds as follows (Fig.3.3):

(1) Starting from a so-called central atom, a sphere is constructed around this central atom, with a parameter defining the radius of this sphere. The atoms which are in

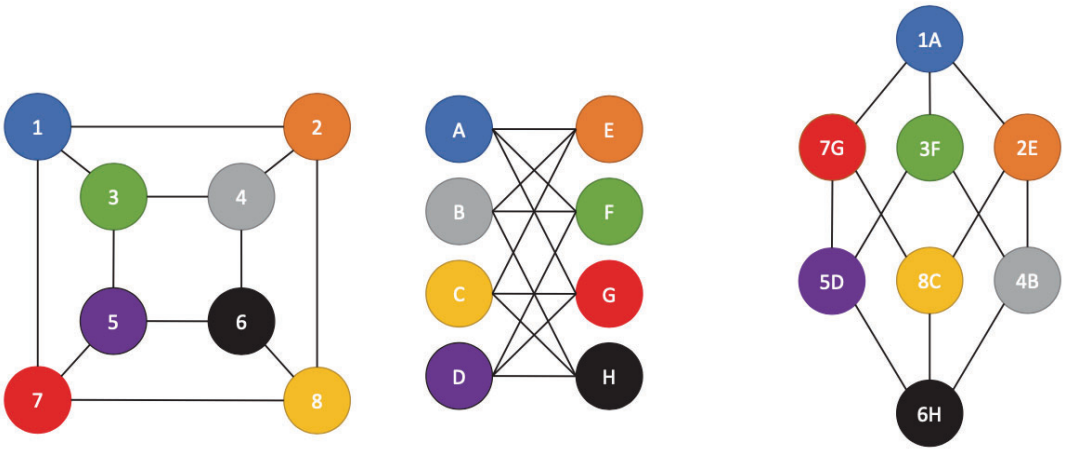

Fig. 3.2. Illustration of two graphs (left and center) by their automorphism group (right) [22, 98].

this sphere form the nodes of the graph. This radius must be chosen so that central atoms with the same initial topology have the same list of transitions. Thus, this radius must minimize the number of inconsistencies that may occur in the lists of transitions of each of these central atoms. For this purpose, one can choose four to six times the average interatomic distance of the system or the typical size of the transitions (the size of the region where the distance between two neighboring atoms is significantly changed by the transition). In summary, this radius must include at least the active local region of all accessible transitions. For example, for a radius of 6 Å, one can obtain between 35 and 50 atoms per sphere for crystalline iron. It depends, in fact, on the local configuration of the central atom considered (pure crystalline region 47 atoms, configuration at the saddle point 37 atoms).

(2) All neighbouring atoms whose distance from each other is smaller than a predetermined threshold are connected (they form the edges of the graph). For crystalline iron, a threshold distance of 2.7 Å is chosen. This parameter lies between the first two crystallographic peaks of crystalline iron (2.45 and 2.86 Å, at room temperature and atmospheric pressure).

(3) Once the diagram is created, it is sent to NAUTY.

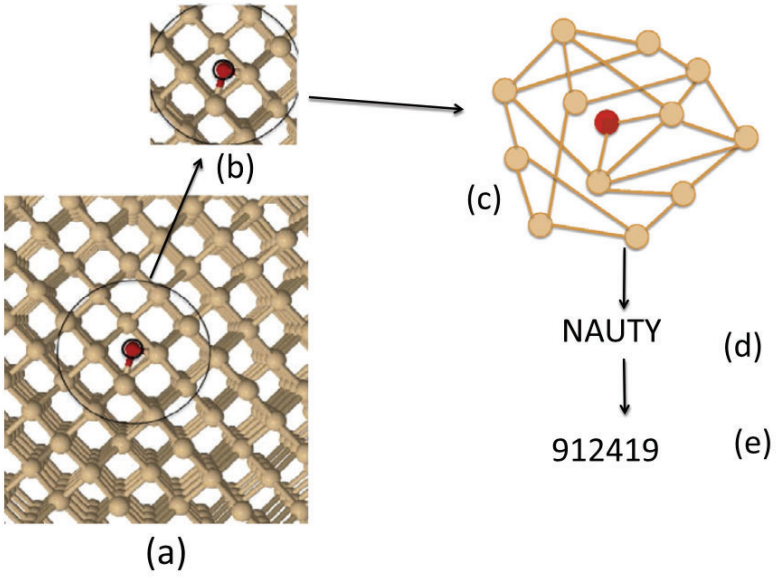

Fig. 3.3. Schematic representation of the topological classification procedure, with the red atom at the centre of the local graph. (a) We select an atom of the configuration and its neighbourhood. (b) Bindings are drawn between these atoms, yielding (c) a connectivity graph that is (d) sent through NAUTY, which returns (e) the automorphic class identifier of the graph and the correspondence between its vertices and those of a reference graph [103].

(4) NAUTY identifies the automorphism group of this graph and provides a numeric key characterizing this automorphism group.

This classification method is stable and allows the environment to be uniquely identified atomically.

3.4. ART nouveau

The search for activated mechanisms is performed using ART nouveau [14, 15], an open climbing method for finding first-order saddle points surrounding a local minimum (a work-flow of ART nouveau is shown in Fig.3.4). From each individual topology in the system, multiple independent searches for saddle points are initiated using a three-step procedure:

3.4.1. Activation

Starting from a local energy minimum q^n, a random deformation (with a certain displacement field $\delta x_A u$, where u is an initial random unitary displacement and the used value

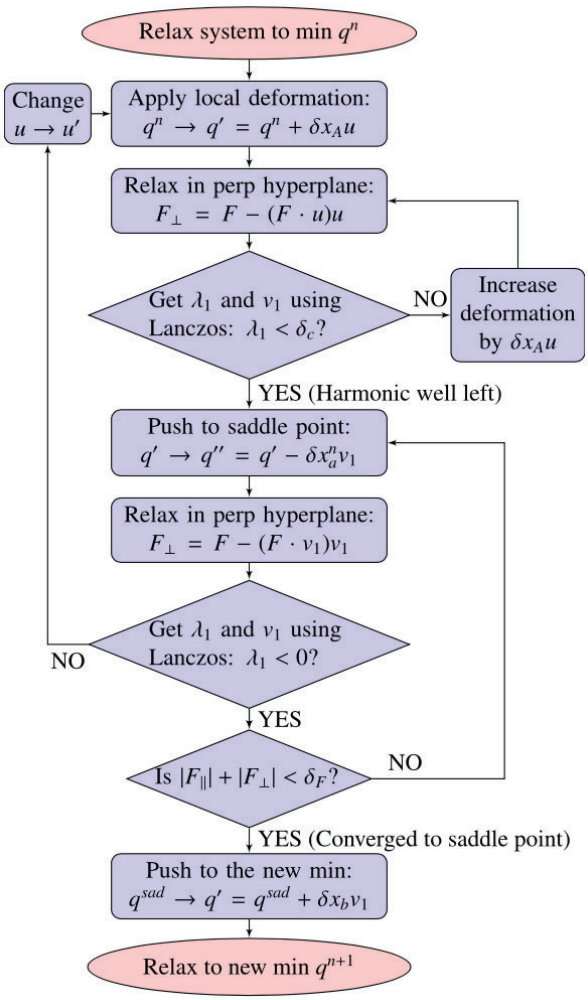

Fig. 3.4. Flowchart of the implementation of ART nouveau [103].

of δx_A is between 0.1 and 0.2 Å) is slowly applied to the central atom of a given topology and its neighbours. To avoid collisions, a relaxation step in the perpendicular hyperplane is performed after each displacement. At the end of each iteration, the lowest eigenvalue λ_i of the hessian and the corresponding eigenvector are calculated using the Lanczos algorithm. This continues until the lowest eigenvalue falls below a certain threshold for negative curvature (δ_c) to ensure that the system is truly outside the harmonic well, or until the maximum number of iterations (generally between 10 and 50 iterations) is reached, in which case a new search is started. The value of δ_c is usually set less than or equal to -1.0 eV $Å^{-1}$.

3.4.2. Convergence at the saddle point

If the activation phase was successful, we still need to converge to the saddle point associated with the negative eigenvalue found during activation. To do this, the system is steered toward the saddle point that follows the direction of the eigenvector ν_1 of the negative eigenvalue λ_1 i.e. $q' \rightarrow q'' = q' - \delta x_a^n \nu_1$, away from the initial minimum. According to the method proposed by Cancès et al. the magnitude δx_a^n must decrease as the saddle point is approached, so it is set to $min(2\alpha, \frac{|F_||}{max(\lambda_1, 0.5)})$, where α is fixed at a value generally between 0.2 Å and 0.5 Å. After each push along the direction of negative curvature, a relaxation step is performed in the hyperplane orthogonal to ν_1. This step is repeated until the total force falls below a specified threshold δ_F to ensure that a first-order saddle has been achieved.

Convergence to the saddle point requires that the lowest eigenvalue remain negative over the entire path, and activation is aborted when this is no longer the case. If this is the case, the system is returned to the initial minimum and a new search is started with a different random value.

3.4.3. Relaxation

Once the system has converged to the saddle point (if the imposed convergence condition is verified), the system is moved away from the initial minimum along the lowest eigenvector by 0.1 times the displacement between the initial and saddle points to prevent the system from falling back to the initial state. The energy is minimized to reach a new minimum q^{n+1}.

At each step, whether leaving the harmonic well, converging to the saddle, or relaxing to a new minimum, all atoms are free to move. There is no restriction on event size or which atoms move the most, allowing for an unbiased exploration of the energy landscape and the creation of a complete catalog. Because of this diversity, and regardless of the topology associated with the initial motion, the events are a posteriori inferred to the atom that moves the most during the event and its topology. The set of initial, saddle, and final points represents an event characterized by three topologies and an energy barrier. For completeness, the events are generally checked for reversibility, ensuring that the saddle point properly connects the

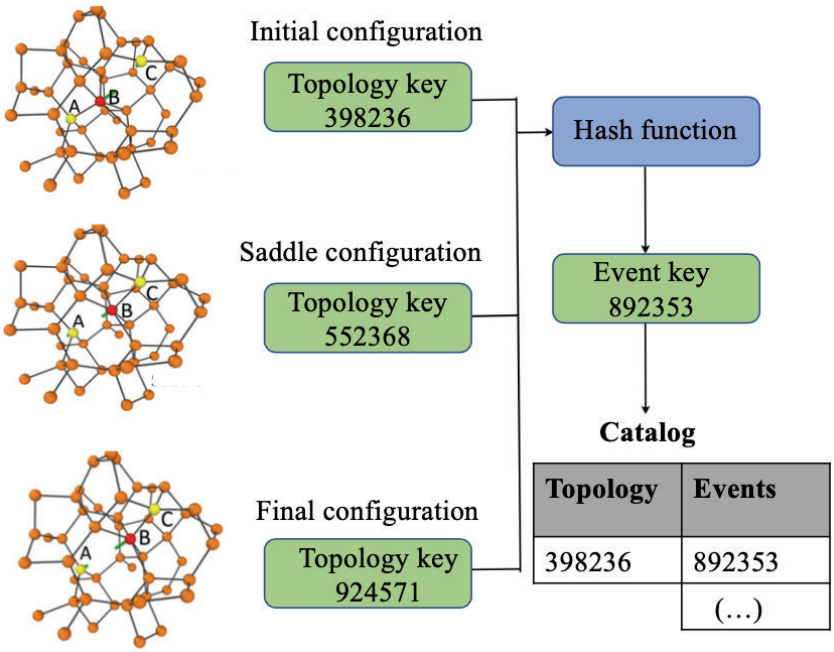

Fig. 3.5. Diagram illustrating the process of identifying an activated event [81].

initial state to the final state, and added to the catalog for both endpoints to ensure detailed equilibrium.

3.5. The event catalog

Using NAUTY and ART nouveau, kART creates a catalog of events as the simulation progresses. The atom to which an event is assigned is the one that undergoes the largest displacement from the initial configuration to the saddle point. If this atom is not identical to the atom where the search was started, the event is focused on this new atom. The topologies of this atom for each of the three configurations (initial, saddle point, and final) are determined using NAUTY. A hash function is used to convert these three topological keys into a unique key to identify the event (see Fig.3.5). These events associated with an initial topology are called generic events. All atoms with the same initial topology also have this event. For each new generic event that is identified, kART automatically generates the reverse event (from the final configuration to the initial configuration). This ensures that kART respects the detailed equilibrium and that the simulation can, in principle, recover

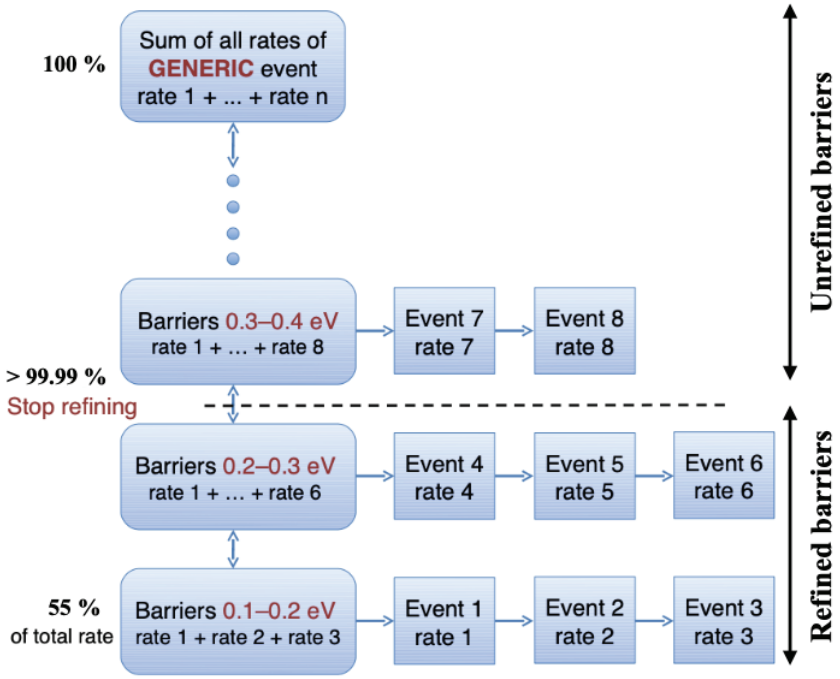

Fig. 3.6. Diagram illustrating the algorithm used for barrier refinement [13].

the previously studied configurations. The entire catalog (the list of known topologies and associated generic events) is stored in a file on disk. This file can be used to restart other simulations on the same system without having to recreate the catalog.

3.6. Long-range elastic deformations

To account for the short- and long-range elastic effects, kART reconverts the events with the smallest activation barriers, whose sum of rates is 99.99% of the total rate. All these barriers are adjusted individually for each atom involved in this event. This process is shown in Fig. 3.6. A histogram of all activation barriers is created in ascending order. The events are reconverged in ascending steps of 0.1 eV. This allows for elastic distortions that can affect the exact value of the activation barrier. Two atoms that have the same topology will have the same event, but they will have slightly different activation barriers, which will affect the kinetics. These customized events are called specific events. These specific events are held in memory during the simulation to speed up convergence, but they are not stored on disk.

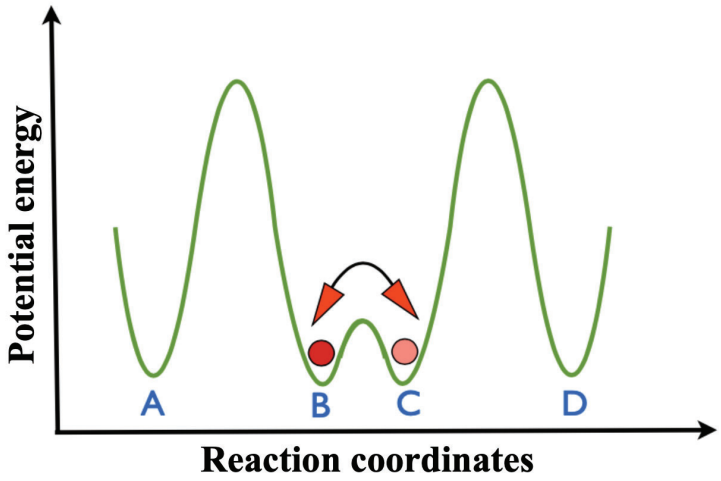

Fig. 3.7. Diagram illustrating an oscillation on the potential energy surface. It will be necessary to observe a very large number of transitions between the states B and C before observing a transition between B and A or C and D.

3.7. The basin method

Activated transitions with small, more or less symmetric activation barriers can completely dominate the kinetics of a system without leading to relaxation or diffusion. Fig.3.7 illustrates this phenomenon on the potential energy surface. The system begins to oscillate between the two configurations very often before finally choosing a transition that allows the system to evolve. The standard KMC algorithm constantly selects these transitions, and a lot of time is wasted simulating these meaningless oscillations.

A basin is defined as a set of adjacent configurations connected by transitions with small, more or less symmetrical activation barriers. It is important to be able to approximate the transitions in these basins without having to explicitly simulate these oscillations.

kART uses the auto-constructing mean-rate method. It is an improvement of the Mean Rate Method algorithm of Puchala et al [112]. This algorithm allows to solve the main equation describing all transitions within the basin without the need to explicitly simulate these oscillations. The rates associated with transitions leading to transitions outside the basin are adjusted to account for the average time spent inside the basin in the initial state.

A matrix **T** representing the probability of making a transition between two configurations inside the basin is obtained as follows

$$T_{ij} = \frac{r_{ij}}{\sum_k r_{ik}} = \tau_i^1 r_{ij} \tag{3.7.1}$$

where r_{ij} is the rate going from basin state i to basin state j, where k runs over all basin and exit states and $\tau_i^1 = \frac{1}{\sum_k r_{ik}}$, the reciprocal of the sum of all rates leaving state i, is the mean residence time in state i each time it is visited. The occupation probability vector of all basin states after in-basin jump m and before jump m+1, $P(m)$ is thus given by repeated application of **T** to the initial occupation probability $P_i(0) = \delta_{is}$, where s is the starting state, as:

$$P(m) = \mathbf{T}^m P(0) \tag{3.7.2}$$

The sum of the occupation probabilities over all possible number of jumps gives the average number each basin state is visited:

$$P^{tot} = \sum_{m=0}^{\infty} \mathbf{T}^m P(0) = (\mathbf{I} - \mathbf{T})^{-1} P(0) \tag{3.7.3}$$

from which the mean residence time in basin state i before leaving the basin can be calculated:

$$\tau_i = \tau_i^1 P_i^{tot} \tag{3.7.4}$$

These residence times are then used to accelerate the basin exit rates from basin state i to exit state j according to

$$< r_{ij} >= \frac{\tau_i}{\sum_k \tau_k} r_{ij} \tag{3.7.5}$$

where k sums over all basin states. The next step KMC is then performed according to the standard algorithm, but using only the accelerated rates of the transitions outside the basin.

The kART basin method also allows new states to be added to the basin while the simulation is in progress. After each out-of-basin transition, the value of the activation barrier and the value of the corresponding reverse barrier are compared to a threshold energy

value. If both values are below this threshold, the new state is considered part of the basin. kART then assumes that we have not actually left the basin, and the new state is added to the **T** matrix. The rates for new out-of-basin transitions are updated. This energy threshold is set during the simulation and must be chosen wisely to capture all transitions that result in oscillatory motion. In practice, it can be seen that the selected threshold is too small if the simulation starts to oscillate repeatedly. The simulation can then be restarted with a larger threshold energy to capture these new transitions within the basin. In general, the threshold value is adjusted several times during a simulation.

3.8. kART-LAMMPS coupling

The coupling between kART and LAMMPS [1, 111] (Large-scale Atomic/Molecular Massively Parallel Simulator) is an encapsulation in the form of a library of LAMMPS within kART. This allows kART to perform three tasks. The first task is to access a large set of interatomic potentials that have been extensively tested by the LAMMPS community. This saves users of kART (and ARTn, since the coupling between ARTn and LAMMPS has also been done) from having to write a separate routine for each class of energy potentials. This is a considerable time for users, but also for developers of kART. Second, the local force calculation, which was already present in kART before the coupling, has been fundamentally rewritten. This allows the forces to be computed locally, restricting the computation of forces to a spherical subset centred on an atom affected by ARTn search or during event refinement. It is even possible to perform only local force calculations, but it is preferable to check beforehand that the effects of elastic deformations are correctly captured. The third task is to be able to parallelize the synchronised computation of the forces in addition to the asynchronous parallelization of the ARTn search. This will certainly be a great advantage of the kART method if the calculation of the local forces is compatible with the parallelized calculation of the forces.

3.9. Interatomic potential

An empirical potential is an analytical function that represents the potential energy of an atom of the material as a function of a certain number of adjustable parameters. The advantage of using these functions is that they allow rapid evaluation of the forces between individual atoms with little computational effort. Calculating the interactions between atoms using an empirical potential is fast and allows simulation of systems with a large number of atoms and over relatively long times. In this work, we use the embedded atom method empirical potential (EAM) proposed by Foiles and Baskes [31], which represents an approximate energy in terms of the sum of the separation functions between an atom and its neighbors. The total energy within the EAM model is calculated as follows:

$$E_{tot} = \frac{1}{2}\sum_{i,j}\phi_{ij}(r_{ij}) + \sum_{i} F_i\left(\sum_{i\neq j}\rho_j(r_{ij})\right) \tag{3.9.1}$$

Where $\phi_{ij}(r_{ij})$ is the pair-interaction energy between atoms i and j separated by the distance r_{ij}, F_i is the embedding energy of the atom i, $\sum_{i\neq j}\rho_j(r_{ij})$ is the host electron density induced by the surrounding atoms j at the location of the atom i. The electron-density function assigned to atom j is $\rho_j(r_{ij})$. The pair interaction, electron density and embedding functions depend on the type of the atom.

3.10. Applications and limitations of kART

In the last decade and more, kART has become one of the most effective methods for simulating the structural evolution of various types of materials and structures, although it is still under development, such as the characterization of the potential energy surface of point defects in crystalline silicon (c-Si) [135], crystalline iron (c-Fe) [18, 116], and crystalline nickel (c-Ni) [90]; relaxation kinetics after ion bombardment damage in c-Si [12, 66]; the relaxation kinetics of amorphous silicon (a-Si) [68]; C diffusion mechanisms in Fe surfaces [115]; the kinetics of point defects in the presence of extended defect kinetics in Fe [20, 117]; the effects of point defect motion in ordered alloys and disordered alloy NiFe [89]; defect diffusion

in alloy 55Fe-28Ni-17Cr [121]. About the work that is the subject of this dissertation, we studied the effects of pressure C diffusion in grain boundaries in Fe, and the kinetic evolution of vacancy clusters in c-Fe will be discussed in Chapters 4 and 5, respectively.

Despite the applicability and great success of kART to various problems related to defects in materials, kART, like all numerical methods, has certain limitations. One of the problems of kART is the occasional trapping of the system in nondiffusive barriers. Despite the development of the bac-MRM method, it remains a major challenge to automate the resolution. As described above, the bac-MRM method computes the average escape time from a pool of flickering states. While this solution represents a huge efficiency gain over simple KMC, the basin setup can be time-consuming. However, once the system leaves the basin and transitions to a new state, the entire basin must be rebuilt, which can significantly slow down the simulation. To address this issue, we newly proposed a local basin approach to handling low-barrier events in the kART. This algorithm detects, on the fly, groups of flickering states and consolidates them into local basins, which we treat with bac-MRM. In this way, when an accepted event occurs in one part of the system, only the basins that are physically close to the affected region are destroyed, while the others remain in the catalog. We will discuss this in detail in Chapter 6.

3.11. Conclusion

The kinetic activation and relaxation technique (kART) is a kinetic Monte Carlo method that successfully overcomes the limitations of the original KMC method. It has become one of the most powerful methods for simulating the structural evolution of defects in materials. In the next chapters, we will present the results we have obtained in the form of articles. In the first and second articles, we have studied the effects of pressure on the C diffusion mechanisms in the grain boundary of α-iron and the diffusion mechanisms of vacancy clusters. In the third article, we will discuss in detail the application of the local basin approach to the kART.

Chapter 4

Pressure effect on diffusion of carbon at the $85.91^\circ < 100 >$ symmetric tilt grain boundary of $\alpha-$iron

4.1. Objective

Diffusion of impurities in materials is both a fundamental and a technological problem. However, because it is difficult to characterize atomic motion using experimental techniques, there are still many unresolved questions about how impurities move, especially in the presence of extended defects. The objective of this paper is to study the effects of pressure on the diffusion of C in an Fe box with a grain boundary. This is relevant to problems such as carbon dusting, but also to understanding how local variations in pressure combined with strain and defects can affect the behavior of impurities that are often characterized under perfect conditions.

Authors in order: Md Mijanur Rahman, Fedwa El-Mellouhi, Othmane Bouhali, Charlotte S. Becquart, and Normand Mousseau

Status : This article has been published in the "Physical Review Materials" journal. Reference: PhysRevMaterials.5.043605

Author contributions:

- Md Mijanur Rahman (MMR) performed all simulations and data analysis.

- MMR wrote the first version of the article.
- Normand Mousseau (NM), Fedwa El-Mellouhi (FEM), Othmane Bouhali (OB), and Charlotte S. Becquart (CSB) contributed to the writing of the article.
- NM supervised all this work.

4.2. Résumé

Le mécanisme de diffusion du carbone dans le fer joue un rôle essentiel dans les processus de carburation, la fabrication de l'acier et la corrosion par effritage des métaux. Dans ce travail, en utilisant la technique d'activation-relaxation cinétique (ARTc), un algorithme de Monte Carlo cinétique hors réseau avec construction de catalogue à la volée qui permet de suivre la diffusion sur de grandes échelles de temps en tenant pleinement compte des effets chimiques et élastiques couplé à un potentiel EAM, nous étudions l'effet de la pression sur les propriétés de diffusion du carbone dans un joint de grains à inclinaison symétrique de fer, α 85.91° $< 100 >$, jusqu'à une pression de 12 kbar à une seule température de 600K. Nous trouvons que si l'effet de la pression peut fortement modifier la stabilité et la diffusivité du carbone dans le joint de grains de manière qui dépend étroitement de l'environnement local et de la nature de la déformation: la pression isotrope et uniaxiale peut conduire à des effets opposés et non monotones concernant énergie de ségrégation et barrières d'activation. Ces observations sont pertinentes pour comprendre l'évolution des matériaux hétérogènes, où les variations de pression locale peuvent altérer la diffusion du carbone à travers le matériau.

4.3. Abstract

The diffusion mechanism of carbon in iron plays a vital role in carburization processes, steel fabrication, and metal dusting corrosion. In this work, using the kinetic activation-relaxation technique (kART), an off-lattice kinetic Monte Carlo algorithm with on-the-fly catalog building that allows obtaining diffusion properties over large time scales taking full account of chemical and elastic effects coupled with an EAM potential, we investigate the effect of pressure on the diffusion properties of carbon in 85.91° $< 100 >$ symmetric tilt

grain boundaries (GB) of α-iron up to a pressure of 12 kbar at a single temperature of 600K. We find that while the effect of pressure can strongly modify the C stability and diffusivity in the GB in ways that depend closely on the local environment and the nature of the deformation: isotropic and uniaxial pressure can lead to the opposite and non-monotonous effects regarding segregation energy and activation barriers. These observations are relevant to understanding the evolution of heterogeneous materials, where variations of local pressure can alter the carbon diffusion across the material.

4.4. Introduction

Metal dusting is a severe form of corrosion causing a catastrophic degradation of metals and alloys at high temperatures in carbon-supersaturated gaseous environments. Engineering alloys such as low-alloy and stainless steels, as well as heat-resisting iron-, nickel-, and cobalt-base alloys, catalyze gas processes that release carbon, leading to the formation of deposits at the surface of the alloy and, over time, to failure. In petrochemical plants and gas-to-liquid (GTL) production facilities, metal dusting has been observed in steel equipment. The so-called Fischer-Tropsch synthesis deposits carbon not only on the catalysts but also on the steel equipment, leading to dusting corrosion. The onset of metal dusting for iron-base alloys is initiated with the saturation of the alloy matrix with carbon/carbides, usually in a localized manner, a process called carburization. In our earlier works, we focused on carburization by characterizing the reaction of iron with CO as well as the diffusion and segregation of carbon within the grain boundaries of the metal. [2, 15, 23, 24, 25, 115, 116, 117, 119]

In this work we aim to turn our attention towards realistic scenarios that occur at various stages of dusting corrosion, drawing comparisons with experiments whenever possible, focusing more particularly on the effect of pressure on C diffusion in Fe, particularly at grain boundaries (GBs). The diffusion of carbon interstitial atoms around GBs in iron has long been an area of interest for researchers due to its impact on various mechanical properties of steel such as corrosion resistance, and embrittlement, but also at it serves as a rich system for modelling and simulation [132, 133]. Over the years, these mechanisms have been

computationally studied at ambient pressure, i.e. the lattice and atomic positions are both relaxed to obtain the atomistic parameters at zero pressure [27, 64, 149, 155]. While limited information is available regarding the effect of pressure on carbon diffusion in iron through GBs, internal or external pressures can build up in the grains due to local deformation. These may reach a magnitude of a few GPa [82, 162, 163], inducing problems such as structural instability, stress corrosion cracking, distortion, etc. [83, 96, 118] It is thus necessary to have a clear description of the effects of pressure on defect diffusion in order to understand the behavior of heterogeneous materials such as carburized steels at the atomic scale.

Because of the microscopic nature of these processes, atomistic simulations are needed to provide an understanding of the details controlling these segregation and diffusion mechanisms that are difficult to obtain from experiments. While standard simulation tools, such as molecular dynamics, offer significant information on atomistic details of these diffusion mechanisms, they are often unable to reach the extended time scale over which many of these processes take place. Standard kinetic Monte Carlo (KMC) simulations provide a solution to reaching long-time dynamics, but, they are constrained to lattice-based displacements that fail to capture the full diversity of diffusion mechanisms as well as elastic deformations, especially around extended defects such as GB [20]. Over the years, numerous improvements have been proposed to standard KMC simulations, in order to overcome these limitations leading to a new interest in the fundamental mechanisms associated with defect diffusion in materials. The recent development of on-the-fly off-lattice kinetic Monte Carlo methods such as the kinetic activation–relaxation technique (kART) [13, 40, 103] lifts those limitations and allows us to map these processes in details. kART is an off-lattice kinetic Monte Carlo method with on-the fly catalog building capabilities which enables to properly describe diffusion mechanism over experimentally-relevant time scales. It enables to reach simulated times many orders of magnitude longer those reachable by MD simulation while incorporating exact elastic effects and identifying the atomistic details of diffusion mechanisms at every step.

In this study, using kART we investigate the effect of pressure on the diffusion mechanism C atom within a GB of α-iron. More precisely, we explore the energy landscape and kinetic pathways. Then, diffusion coefficients are calculated to quantify the effect of stress on diffusivity. The paper is organized as follows: the methodology, including a brief overview of kART, the model employed and the computational details, is presented in section 5.5. Then, simulation results are presented and discussed in section 4.6 and 4.7 respectively. Finally, the conclusion is given in section 4.8.

4.5. Methodology

4.5.1. Kinetic-Activation Relaxation Technique (kART)

The kinetic activation relaxation technique (kART) [13, 40, 103] is an off-lattice kinetic Monte Carlo (KMC) method with on-the-fly catalog building. kART is built around three tools: (i) NAUTY [97], which allows a topological characterization of the local environment surrounding each active atom; (ii) the activation-relaxation technique (ART nouveau or ARTn) [7, 88, 92], an open-ended saddle-search methods for exploring the local energy landscape and (iii) a KMC algorithm,[146] that evaluates the time between two steps and selects the event. The basic principles are briefly described below:

At the beginning of each KMC step, the local environment surrounding each atom is characterized by their local topology evaluated with NAUTY, a topological analysis library developed by McKay [97]. Graphs are generated by considering a sphere with a predefined radius (6 Å for the current system) around each atom in the system that contains around 75 atoms and drawing edges between all atoms within a cut-off distance of 2.7 Å of each other, a value that ensure that mostly only first-neighbor atoms are included. This connectivity graph is sent to NAUTY which returns a unique identifier characteristic of its automorphic group.

If the topology is known, events associated with it are recovered from the catalog and placed in a KMC tree; otherwise, 100 ARTn searches are launched to identify the events associated with this topology. The ARTn search takes place in three steps: (i) first, the

system is pushed in an arbitrary direction until the lowest eigenvalue of the Hessian matrix, determined using the Lanczos algorithm, becomes negative to confirm that the system is out of the harmonic well; (ii) then the system is pushed along the direction of the negative curvature and the force is minimized in the hyperplane perpendicular to this direction after each push until the total force becomes lower then a predefined threshold value, indicate that a first order saddle point is reached; and (iii) the system is then push over the saddle point and relaxed into a new minimum.

Once the catalog is fully updated and the tree is completed for the current atomistic configuration, generic events are ordered according to their rate, defined as:

$$\Gamma_i = \nu_0 e^{-\frac{E_b}{k_B T}} \tag{4.5.1}$$

where ν_0 is a fixed prefactor which is fixed at 10^{13} Hz and E_b, the activation energy for event i defined as the energy difference between the transition state and the initial minimum [42, 43, 78]. Once the event tree is completed, the lowest-energy barrier events that make up to 99.99 % of the rate are fully reconstructed and reconverged into specific events to ensure that elastic and configurational effects are exactly taken into consideration. When this is done, specific rates and the overall KMC timestep are evaluated again, with the refined barriers, and an event is chosen according to standard KMC algorithm [146]. The elapsed time t is computed according to a Poisson distribution as:

$$t = -\frac{\ln \mu}{\sum_i \Gamma_i} \tag{4.5.2}$$

where μ is the random number uniformly distributed between 0 and 1.

To sum up, kART makes use of a unique topology classification coupled with an unbiased, open-ended search for saddle points, while considering short- and long-range interactions due to elastic effects. An extensive catalog of the events are created on-the-fly which speeds up the simulation as the system evolves. In the past, kART has been used in various systems to describe diffusion of point defects in metals and semiconductors and more complex systems with grain boundaries and amorphous silicon [67, 89, 117].

4.5.2. Handling flickering states

KMC simulations can become inefficient in the presence of low energy barriers that dominate the kinetics, as each step is then associated with a very small clock increase. In some cases, these events are flickers, a set of states, separated by low-energy barriers deep in a energy basin and that do not contribute to the evolution of the system. To avoid getting trapped by flickers, we use the basin auto constructing mean rate method (bac-MRM) [13, 112] to solve analytically the average residence time for the in-basin states. This method computes on-the-fly a statistically exact analytic solution of the connected flickering states and their escape rate as the energy landscape is explored, at the cost of specific trajectories. The bac-MRM is applied to all states connected by barriers and energy difference lower than a predefined threshold (0.5 eV is used in this study).

4.5.3. Interatomic potential

In order to access relevant length and time scales, we employ an empirical force-field to describe the system. The Fe-Fe interactions are handled by the Embedded Atom Method (EAM) interatomic potential developed by Ackland and Mendelev [100] while the Fe-C interaction part was developed by Becquart and collaborators [10, 138]. The combined potential provides a good agreement with DFT calculations in bulk system [116]. This potential has been used with success to model the effect of the stress field of an edge dislocation on carbon diffusion, the formation of carbon Cottrell atmospheres in bcc-iron as well as the elastic constants of the martensite [28, 134, 139]. For all calculations, kART uses the LAMMPS library to compute the forces and energies [1, 111].

4.5.4. Simulation details

Two simulation boxes are used in this work. The first one consists in a perfect cubic BCC bulk crystal containing 2000 iron atoms. The second box is a BCC system containing 25537 atoms featuring a $85.91° < 100 >$ tilt GB with dimensions of $34.332\,\text{Å} \times 113.090\,\text{Å} \times 76.595\,\text{Å}$. To allow periodic boundary conditions in all directions, the box contains two GBs separated

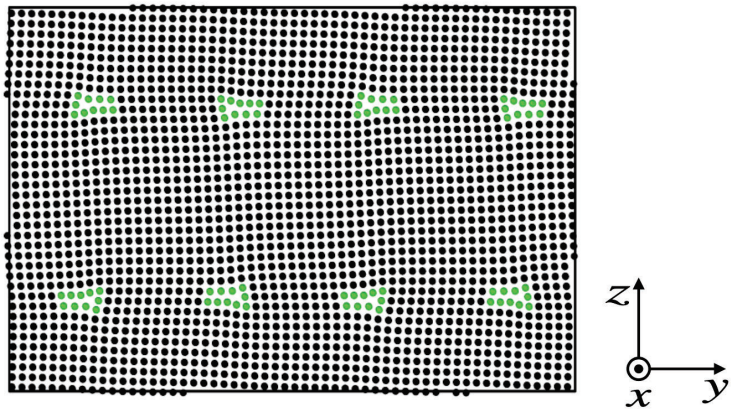

Fig. 4.1. Atomic arrangement representation of the 85.91° < 100 > tilt GB in BCC Fe after 1 ns of initial relaxation using molecular dynamics (MD) at zero pressure and temperature 600 K prior to starting kART simulations. Black circles represent Fe atoms having a crystalline BCC local environment, while green circles represnt atoms having a non-bcc environment surrounding the GB. The GB rotation axes < 100 > are parallel to the x axis out of planes, while GB planes are perpendicular to the z axis

by a distance equal to half the box size in the z direction. The 85.91° < 100 > structure is a general GB with GB energy per unit area, $E_{GB} = 37.118\ meV/\text{Å}^2$. This GB Fe system was chosen because of its structural stability, and the presence of a number of sites where C can be trapped, allowing us to focus on the effect of deformation impurity diffusion. An atomistic representation of the GB is shown in Fig.4.1. To determine the appropriate simulation volume, the system boxes, with a C interstitial, are equilibrated at the targeted pressure at 600 K temperature by perfoming NPT ensemble with LAMMPS. The volume is then fixed for kART simulations.

For each simulation, the ground state (GS) energy is defined as the lowest energy minimum identified during the run, E_{GS}. The activation energy for an event is defined as the energy difference between the initial minimum E_{min} and the saddle E_{sad} (i.e., the barrier crossed between two adjacent minima) or

$$E_b = E_{sad} - E_{min}. \tag{4.5.3}$$

The effective barrier is defined as the total barrier crossed when jumping from one GS to another GS.

The square displacement (SD) is computed as usual,

$$SD = \sum_{i}^{N} (r_i(t_n) - r_i(0))^2, \tag{4.5.4}$$

where N is the number of particles and $r_i(t_n)$, the position of atom i at KMC step n.

To ensure sufficient statistics, the diffusion coefficient of carbon interstitial atom calculated using the embedded discrete time Markov chain (EDTMC) described as follows:

(1) choose an initial state i;

(2) generate a uniform random number u ϵ (0,1];

(3) select the next event j probabilistically such that $\sum_k^{j-1} p_{ik} < u \leq \sum_k^j p_{ik}$, where, p_{ik} is the probability to jump from state i to state k ;

(4) update the total selection number of state j by adding 1;

(5) update the current state j $\rightarrow$ i;

(6) return to step ii.

EDTMC uses the transition matrix obtained from kART and that includes all the structurally different sites in which C visited and the mapped connectivity between the sites and their associated relative transition rates. For all coefficient diffusion results presented here, we run 600 million EDMC steps to obtain the relative frequency distribution $\bar{\Pi}$:

$$\bar{\Pi} = \begin{bmatrix} \pi_1 & \pi_2 \dots & \pi_m \end{bmatrix} \tag{4.5.5}$$

where, π_i represents the proportion of times that site i is selected and m is the total number of structurally different sites in the system, for instance, in the case of perfect bulk crystal there are structurally three different sites directed along x, y or z (shown in Appendix A Fig. S1).

After obtaining the relative frequency distribution, we then calculate the average time $< t >$ and average square displacement $< SD >$:

$$< t >= \sum_{i=1}^{m} \pi_i \tau_i \tag{4.5.6}$$

$$< SD_l >= \sum_{i=1}^{m} \sum_{j=1}^{m} \pi_i p_{ij} (\lambda_{ij}^l)^2 \tag{4.5.7}$$

with $l = x,y,z$ and,

$$< SD >=< SD_x > + < SD_y > + < SD_z > \tag{4.5.8}$$

where, τ_i is the mean residence time at site i, p_{ij} is the transition probability from site i to site j and $p_{ij} = 0$; $\forall$ i=j. λ_{ij}^l correspond to the $l = x,y,z$ components of the displacement vectors for the jump form site i to site j respectively.

The total diffusion coefficient is calculated as:

$$D = \frac{< SD >}{2n_d < t >} \tag{4.5.9}$$

where, n_d is the dimensionality of the motion (1-3).

4.6. Results

4.6.1. Carbon in bulk iron

First we analyze the effect of pressure on the evolution of a single C atom in crystalline α-Fe. In the ground state, the C atom occupies the octahedral interstitial position, located in the middle of one of the three edges of the cubic unit cell (shown in the Appendix A Fig.S1); it migrates, following its dominant pathway, by going through an adjacent tetrahedral site that represents the transition state. With respect to the orientation of the two closest Fe atoms closest, three octahedral variants directed along x, y or z can be identified. These are energetically equivalent in the perfect BCC lattice, but split into two non-equivalent types under uniaxial deformation: a distortion along x axis divides the octahedral sites into O_x and $O_y \equiv O_z$ (shown in Appendix A Fig. S2).

Recently, Tchitchekova *et al.*, using a method called Linear Combination of Stress States (LinCoSS), evaluated the effects of simple-heterogeneous uniaxial and shear stresses on the migration energies of C in bulk Fe [134]. In this section, we reproduce this result for a C in

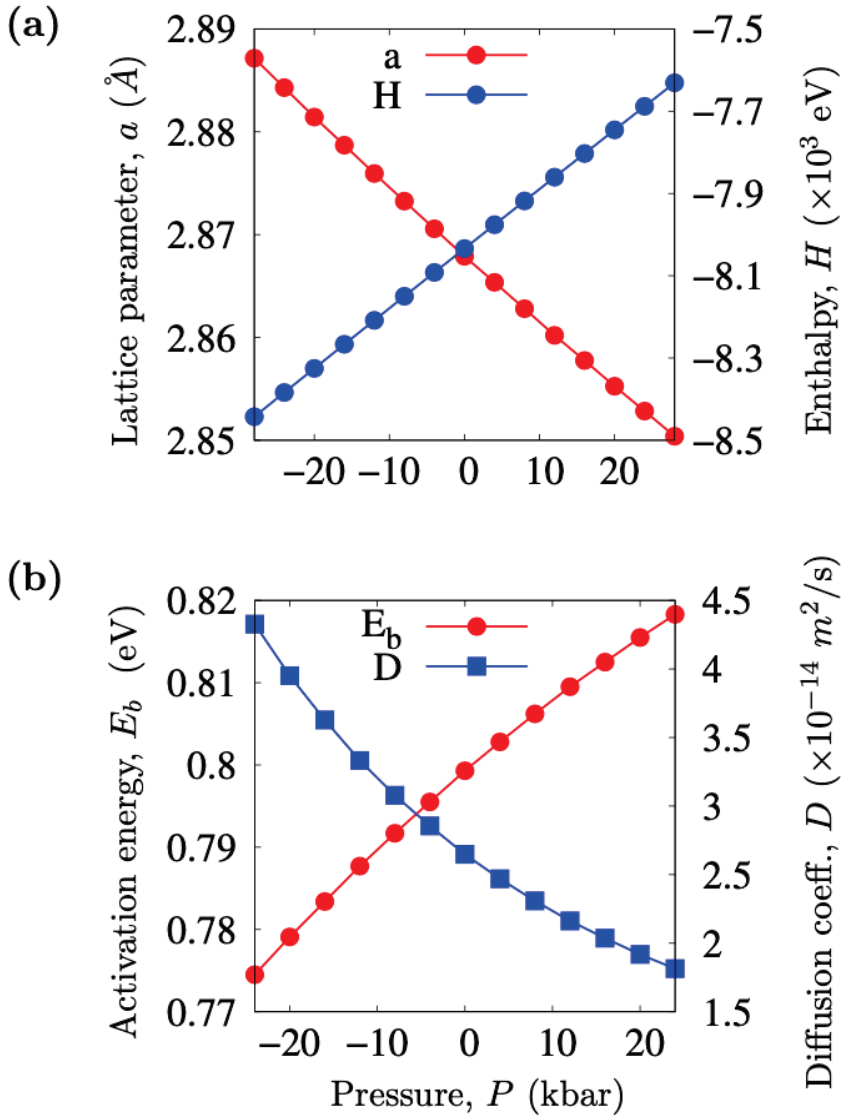

Fig. 4.2. (a) Enthalpy variation for a single carbon in 2000-atom Fe bulk crystal (blue circles) and crystal lattice parameter (red circles) as a function of isotropic pressure. (b) Variation of the activation energies (red circles) and diffusion coefficients (blue squares) as a function of pressure for a single carbon atom in the same system. Diffusion coefficient is calculated with EDTMC and Eq. 4.5.9.

bulk Fe with a thermally-adjusted density corresponding to 600 K, but also consider isotropic deformations and extract the diffusion coefficient for each of these deformations.

The variation of the crystalline lattice parameter and of the system's enthalpy as a function of isotropic pressure are shown in Fig.4.2a while the evolution of the activation energy for an interstitial C atom as it jumps from one octahedral site to a nearest octahedral site and the diffusivity of C as a function of pressure are plotted in Fig.4.2b. Both the

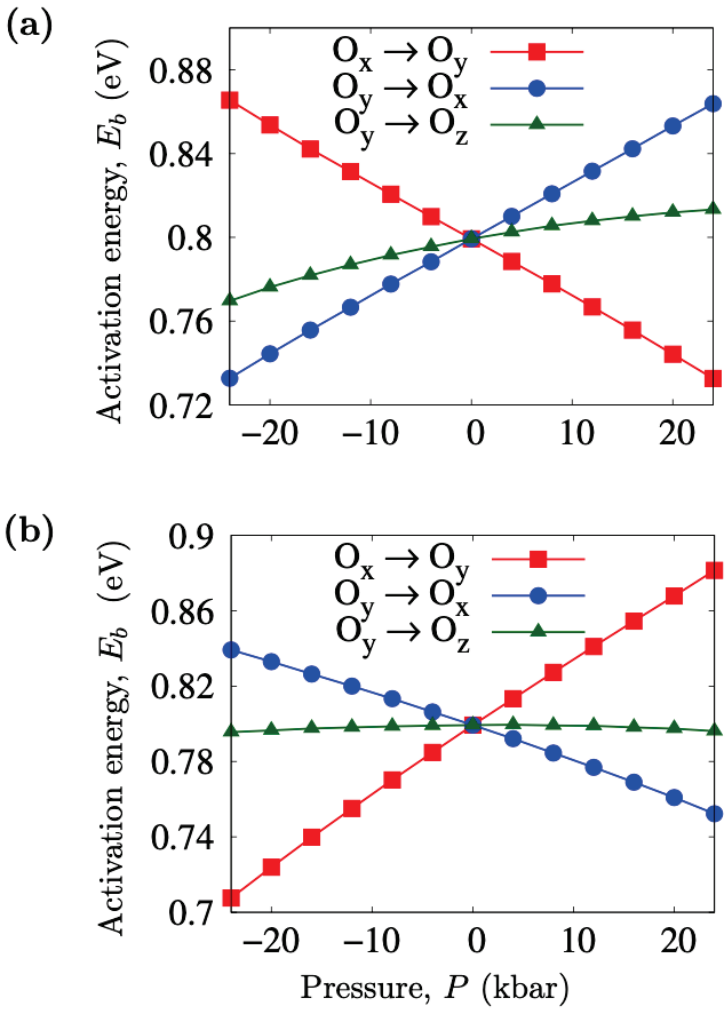

Fig. 4.3. Variation of the activation energy for C diffusion in the bulk iron at 600 K as a function of (a) uniaxial and (b) under biaxial stress. The red square, blue circle, and green triangle represent the carbon diffusion between octahedral variants $O_x \rightarrow O_y$, $O_y \rightarrow O_x$ and $O_y \rightarrow O_z$ respectively.

diffusion activation energy and the total enthalpy show a positive correlation with isotropic pressure over the full range considered here. The variation of activation energies E_b and that of the total enthalphy follows a quadratic form with the values for the constant, linear and quadratic parameters listed in the Appendix A Table S1.

The effects of uniaxial pressure (along x axis) and biaxial pressure (along y and z axes) are shown in Fig.(3-4). Fig. 4.3a and Fig. 4.3b present the activation energy for an interstitial C atom as it jumps from one octahedral site to a nearest octahedral site as a function of uniaxial pressure and biaxial pressure respectively. Activation energies from O_x to $O_y(\equiv O_z)$, from

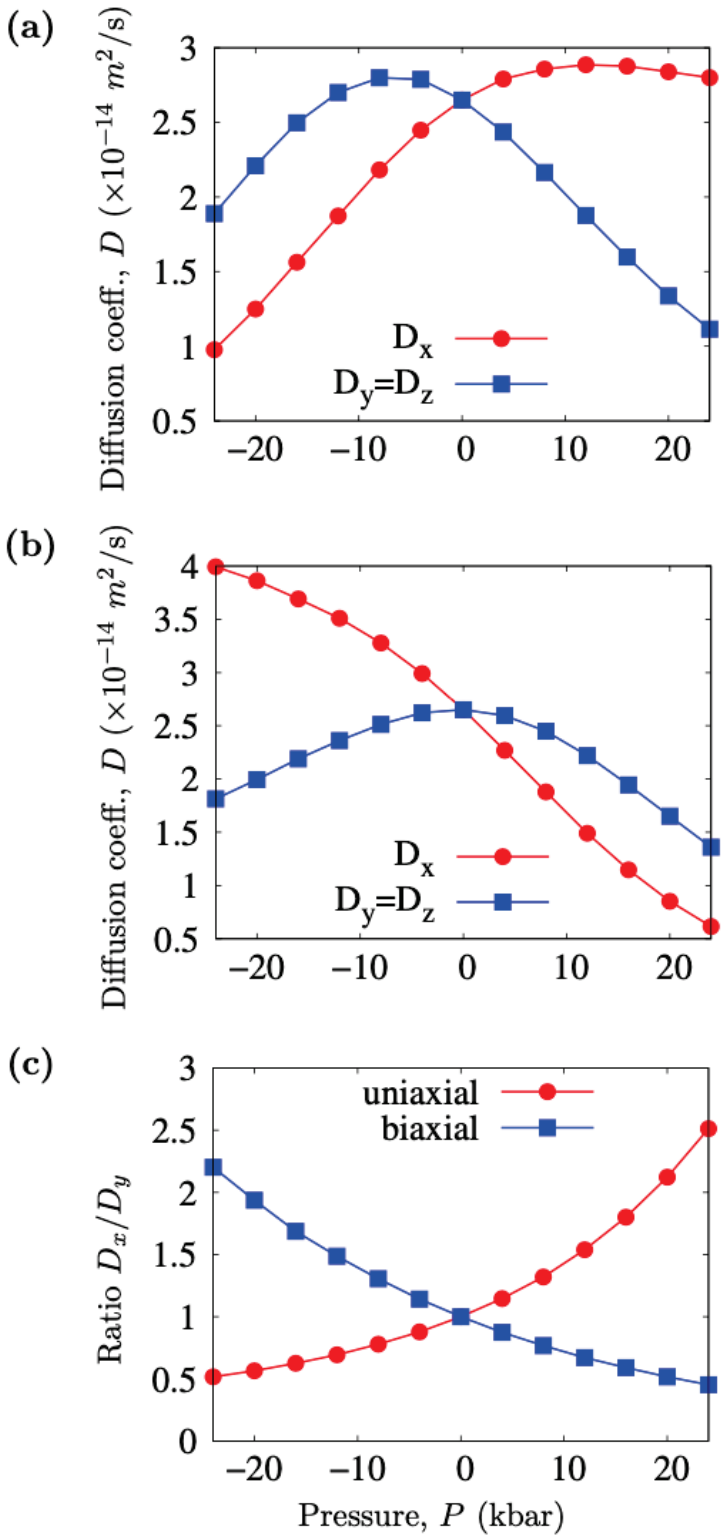

Fig. 4.4. C diffusion coefficient in the bulk crystal at 600 K as a function of (a) uniaxial stress, (b) under biaxial and (c) ratio D_x/D_y. All the values are calculated using EDTMC and Eq. 4.5.9.

Table 4.1. Values of the coordination number, shortest Fe-C bond length and segregation energies of the four most stable sites at the GB region at different pressures.

Site	Coordination No.	0 kbar		Isotropic pressure				Pressure applied along x-axis				Pressure applied y and z axes			
				12 kbar		-12 kbar		12 kbar		-12 kbar		12 kbar		-12 kbar	
		d^{min}_{Fe-C} (Å)	E_{seg} (eV)	d^{min}_{Fe-C} (Å)	E_{seg} (eV)	d^{min}_{Fe-C} (Å)	E_{seg} (eV)	d^{min}_{Fe-C} (Å)	E_{seg} (eV)	d^{min}_{Fe-C} (Å)	E_{seg} (eV)	d^{min}_{Fe-C} (Å)	E_{seg} (eV)	d^{min}_{Fe-C} (Å)	E_{seg} (eV)
S_0	8	2.029	-0.745	2.028	-0.822	2.031	-0.660	2.023	-0.740	2.033	-0.735	2.032	-0.814	2.010	-0.673
S_1	5	1.764	-0.20	1.763	-0.220	1.765	-0.174	1.768	-0.190	1.763	-0.206	1.763	-0.230	1.766	-0.164
S_2	5	1.775	-0.164	1.774	-0.198	1.775	-0.123	1.776	-0.120	1.773	-0.178	1.772	-0.214	1.775	-0.080
S_3	5	1.819	-0.057	1.818	-0.089	1.820	-0.017	1.813	0.013	1.823	-0.091	1.823	-0.126	1.812	0.028

$O_y(\equiv O_z)$ to O_x and from O_y to O_z follow a quadratic curve (values of the linear parameters and quadratic parameter listed in the Appendix A Table S1). Fig. 4.4a and Fig. 4.4b show the C diffusion coefficient at temperature 600K at each directions as a function of uniaxial and biaxial pressure respectively. Calculated activation volume V^{act} , activation barrier E^{act} and diffusion prefactor D_0 are listed in the Appendix A Table S2. We find that $D_y(\equiv D_z) < D_x$ under uniaxial compression and $D_y(\equiv D_z) > D_x$ under uniaxial expansion with the the ratio D_x/D_y is approximately inversed when the pressure changes sign (see Fig.4.4c).

Under uniaxial compression along the x-axis, the O_y and O_z octahedral sites are more energetically stable sites than the O_x octahedral sites by as much as 0.132 eV at 24 kbar (shown in Appendix A Fig. S2), with barriers going from O_y (O_z) to O_z (O_y) lower by as much as 0.051 eV as compared with O_y (O_z) to O_x. Consequently the lowest-energy diffusion pathway for C interstitial goes from O_y to O_z to O_y, channeling the C atom along the contracted axis. Therefore, the axial compression promotes axial diffusion. On the contrary, axial expansion promotes transverse in-plane diffusion along the chain (O_y or O_z) $\rightarrow O_x \rightarrow$ (O_y or O_z) $\rightarrow O_x$..... (detailed C diffusion trajectories obtained with kART under uniaxial deformation are shown in Appendix A Fig.S3).

Since the contraction along x direction is equivalent to expansion along y and z direction, biaxial deformation just reverse the tendancy : biaxial compression promotes C diffusion along the y-z in plane while the biaxial expansion promotes x-channeling diffusion.

4.6.2. Carbon in the Grain boundary

To relieve the pressure created on the crystalline network, interstitial impurities such as C tend to segregate towards defects, such as grain boundaries (GB), where there is more free

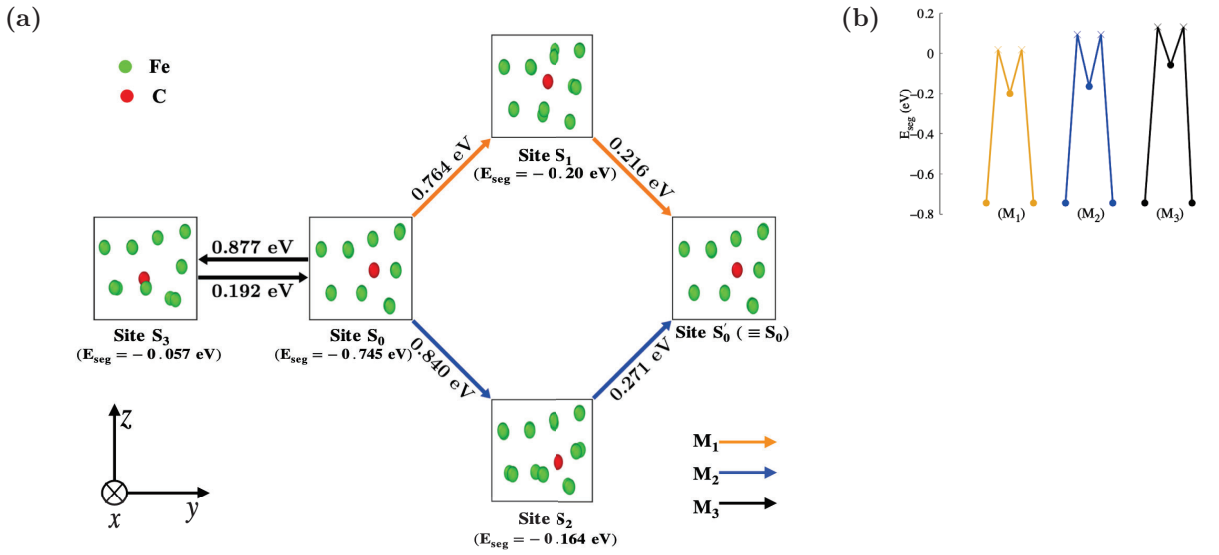

Fig. 4.5. (a) Atomistic representation of three most frequent diffusion mechanisms of carbon atom at the dislocation core in GB at zero pressure. The orange, blue and black lines indicate mechanisms M_1, M_2 and M_3 respectively. M_1 and M_2 can move the C atom into a new final configuration (S_0') (equivalent to the initial configuration (S_0) with the impurity jumping by one lattice spacing along the x direction); M3 brings the C atom back to its initial configuration (S_0). It does not contribute to the net diffusion. (b) The minimum energy pathway for the different mechanisms is shown, where the circles and crosses represent minimum and saddle points, respectively. E_{seg} is the relative energy with respect to the bulk ground state for C.

volume than on the crystalline bulk side. This segregation propensity depends, of course, on specific binding sites at the GB and is characterized by the segregation energy defined as the difference between the energy of the system with C in a particular site and that in the octahedral site in the crystal side. A negative value of segregation energy means that the grain boundary site is energetically more favorable than the bulk site and signals a general flux from the bulk to these sites at the GB.

As demonstrated in our previous work [117], the disorder associated with GB generates a variety of atomic environments, facilitating the formation of sites more energetically favorable to the presence of carbon than interstitial crystalline sites. Depending on the specific nature of the interface between the grains, these favorable sites could be connected to accelerate or to slow down carbon diffusion as compared to the bulk. In the specific case studied here, we add that, segregation energies as well as related C migration barriers are reported

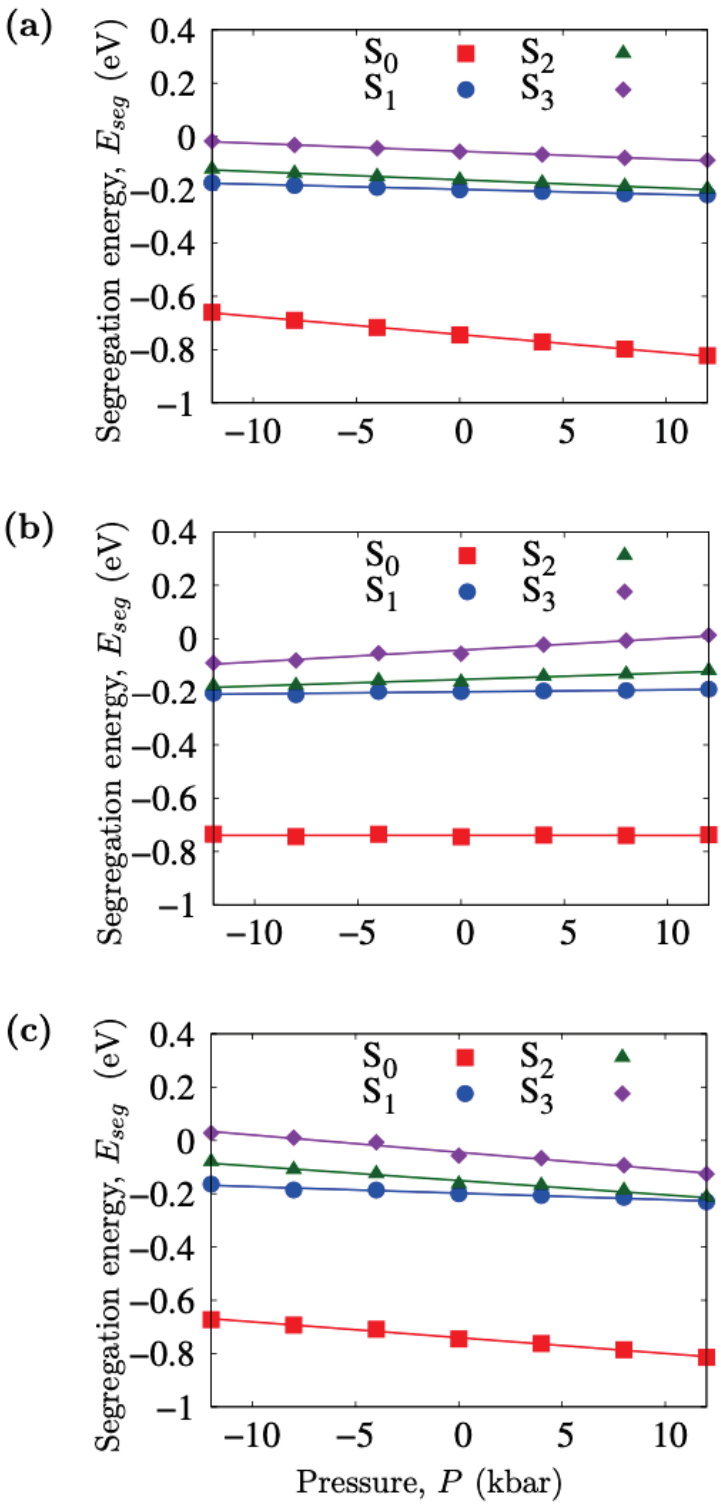

Fig. 4.6. Segregation energy as a function of pressure for a C atom at the 85.91° GB:(a) under isotropic pressure, (b) pressure along the x-direction and (c) pressure applied along the plane perpendicular to the GB plane. Red square, blue circle, green triangle and violet diamond are correspond to carbon at the site S_0, S_1, S_2 and S_3 respectively.

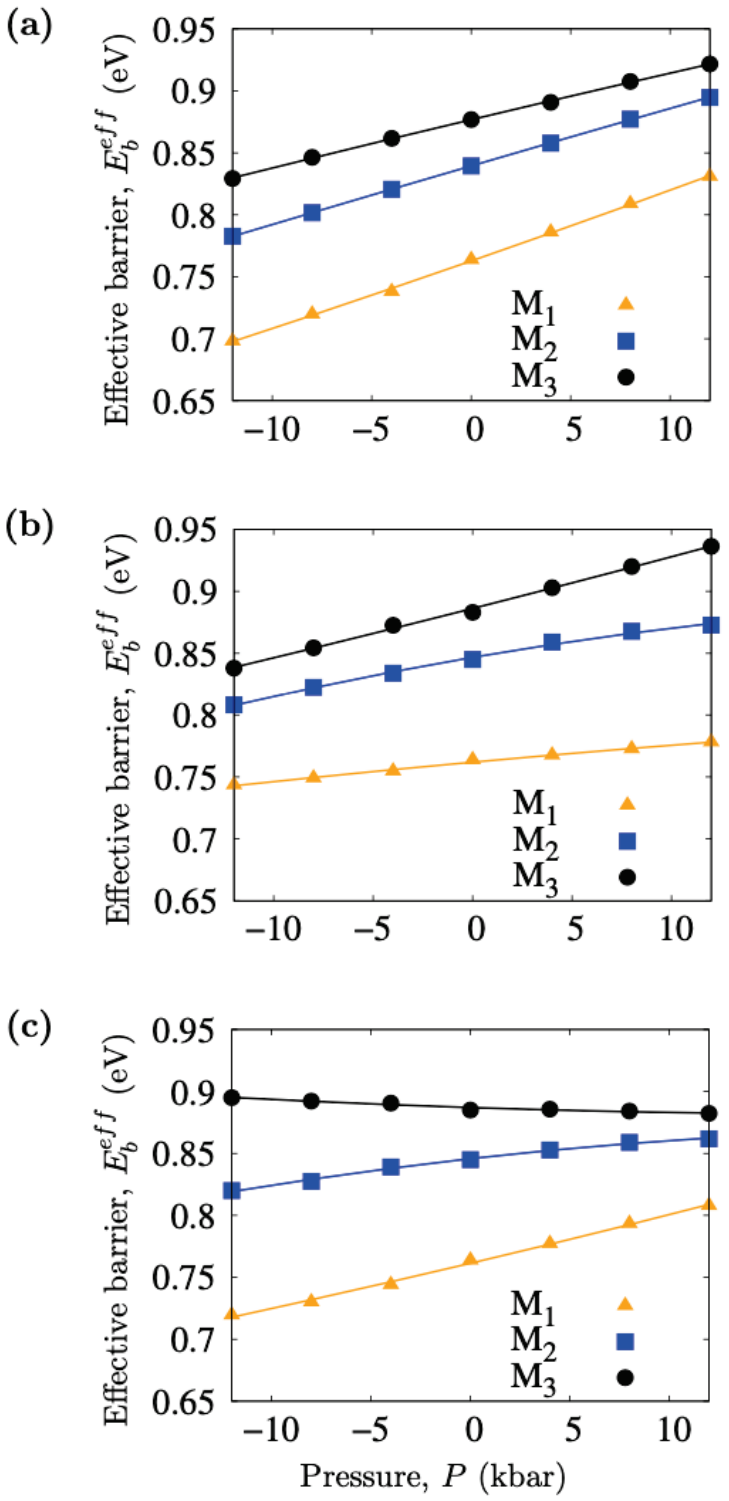

Fig. 4.7. Variation of the effective barrier of the diffusion mechanism M_1, M_2 and M_3 as a function of pressure: (a) under isotropic pressure, (b) pressure along the x-direction and (c) pressure applied along the plane perpendicular to the GB plane.

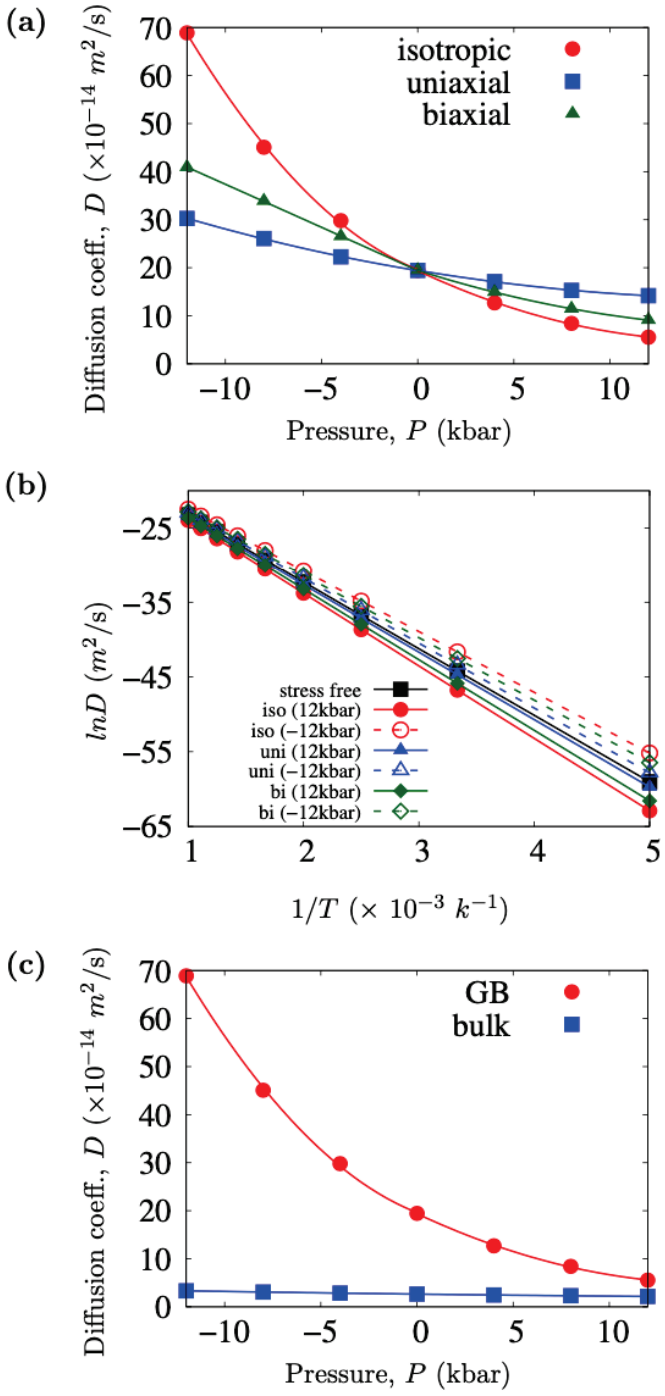

Fig. 4.8. (a) Variation of the C diffusion coefficient at the GB as a function of pressure: red circle, blue square, and green triangle represent the applied pressure isotropic, along x-axis, and along y and z axes respectively. (b) Arrhenius plot of the diffusivity of C in GB: red, blue and green line represent for the applied pressure isotropic, along x-axis, and along y and z axes respectively. Black line refers to stress-free conditions. (c) Variation of the diffusion coefficient of C as a function of isotropic pressure: red circle and blue square represent C at the GB and crystalline bulk respectively. Results are presented here are calculated using Eq. 4.5.9.

in the current work differ from the value found in our previous work [117] as they are identified differently: sites identified in the previous work were generated kinetically through C migration from the bulk to the GB[117] while a direct extensive search for C sites, with simulations launched from different GB sites, was performed for the current work to identify the thermodynamically preferential sites. While this approach leads to different diffusion pathways, it does not affect the validity of our previous analysis.

kART search for C diffusion pathways at the 85.91° GB finds 6 different connected sites, with a segregation energy ranging from -0.745 eV to 0.180 eV at zero pressure. Fig.4.5 represents the four most energetically favorable sites for carbon segregation (S_0 to S_3), along with their segregation energy, measured with respect to the bulk ground state for C at zero pressure, and activation energies for diffusion between these sites. Further details, including shortest Fe-C bond length, coordination number and segregated energies under various static deformations, are listed in Table 4.1. The coordination number is defined as the number of neighboring Fe atoms within a cut-off distance of 2.47 Å from the C atom. As previously found for this specific grain boundary [117], even the highest energy states along the dominant diffusion pathways at the GB are lower than the bulk ground state, which indicates a strong segregation tendency of C atoms to the GB. At the GB, the lowest-energy state at the GB is labeled S_0 (situated at the center of the dislocation core of the GB), with a segregation energy of -0.745 eV. Among the four lowest-energy states (S_0 to S_3), S_0 shows the highest coordination number, with the longest Fe-C nearest neighbor distance associated with a low-stress environment as compared with the bulk site (Table 4.1).

Fig.4.6(a-c) represents the variation of the segregation energies for these four lowest-energy sites as a function of isotropic pressure as well as uniaxial (along x-axis: direction of GB) and biaxial (along y and z axes: plane perpendicular to the GB direction) deformations. Within a range of -12 to 12 kbar, the segregation energy of the C at each binding site tends to evolve linearly, although the slope varies with specific sites. The displayed relative energy shows that all C binding sites at the GB become more stable as compared to the interstitial octahedral sites of the crystal side under isotropic compression. As the pressure is increased

from 0 to 12 kbar, the segregation energy of C at the most stable site (S_0) increases in stability by 0.077 eV, whereas the segregation energy of C at sites S_1, S_2 and S_3 increases in stability by 0.02, 0.034, and 0.032 eV respectively. A similar behavior is observed under biaxial pressure. However, sites S_1, S_2, and S_3 are even more favored, as compared to the case of isotropic pressure, with increasing the pressure (values listed in table 4.1). Under biaxial compression, the two Fe nearest-neighbors are displaced along the x direction, leaving more space for the C atom. Interestingly, the segregation energy of sites S_0 remains unaffected by uniaxial deformation, since the radius of the dislocation core is unaffected by the deformation. Hence, the increment (or decrement) in the total energy of the C at site S_0 and the octahedral site in the crystal side are almost same under uniaxial pressure. By contrast to isotropic and biaxial pressure the sites S_1, S_2 and S_3 are destabilized under uniaxial compression.

After characterizing the change in stability of the dominant segregation sites under pressure, we now turn to the effect of pressure on the C activation energies and diffusion pathways at the 85.91° GB. C diffusion at the GB is complex as compared with that of the crystalline bulk. As demonstrated in a previous work [117], at zero pressure, C diffusion occurs through several pathways that move through the most favorable GB sites (the energy details of all available events and the histogram of the activation energy barrier for selected events at 600 K for a single C at GB during the 12000 KMC steps are shown in the Appendix A Fig.S3 and Fig.S4 respectively). Fig.4.5 provides an atomistic representation of the three most frequent C diffusion local pathways at the GB that we label as M_1, M_2 and M_3. Each pathways is a two steps process: C diffuses from the ground state (site S_0) to a metastable state (S_1,S_2 or S_3), then from this metastable state to a new GS (site $S_0' = S_0$). While, after these two jumps, M_1 and M_2 can reach a new lower-energy state, dubbed S_0', M_3 systematically brings the C back to its initial position when following the lowest-energy pathways and, as such, does not contribute to diffusion. M_1 exhibits the lowest maximal energy barrier, which makes mechanism M_1 the most probable. At zero pressure, the first step of mechanism M_1 requires crossing an energy barrier of 0.764 eV to reach S_1. From there the C then crosses a 0.216 eV barrier to complete the migration into a new S_0 site. The second (M_2) and

third (M_3) low-energy diffusion mechanism are associated with effective barriers of 0.840 and 0.877 eV respectively compared to 0.810 eV in the bulk.

The variation of the effective energy barriers for the three dominant pathways at the GB along with their selection's frequency as a function of pressure is shown in Fig.4.7. Within a pressure range -12 to 12 kbar, the effective barrier associated with M_1, M_2 and M_3 varies linearly with pressure, but at different rate. In the case of isotropic deformation, as the pressure is increased from 0 to 12 kbar, the effective barriers associated with the dominant diffusion mechanism (M_1) increase by 0.111 eV, whereas the effective barriers for mechanism M_2 and M_3 increase by 0.055 and 0.045 eV respectively. Since, the energy gap between the pathway's effective barriers narrows as pressure is increased, the less probable mechanisms (such as M_3) become more frequent under isotropic compression at temperature 600 K. In the case uniaxial deformation, on the contrary, the energy gap between the pathway's effective barriers widen and mechanism M_1 become even more dominant under compression. As the pressure is increased from 0 to 12 kbar the effective barriers associated with the diffusion mechanism M_1, M_2 and M_3 increase by 0.014, 0.028, and 0.053 eV respectively. By contrast to the isotropic and uniaxial pressure, effective barriers associated with the diffusion mechanism M_3 decreases under biaxial compression. As the pressure is increased from 0 to 12 kbar, the effective barriers associated with the diffusion mechanism (M_3) decrease by 0.003 eV, whereas the effective barriers for mechanism M_1 and M_2 increase by 0.078 and 0.017 eV respectively.

C diffusion at 85.91° $<100>$ tilt GB is largely restricted to the interface and diffusion take place mostly along the x-axis (diffusion trajectories obtained with kART at different pressure are shown in Appendix A Fig.S6).

To extract a converged diffusion coefficient, we turn, as discussed in the method section, to a Markov chain solution on a transition probability matrix (the size of which ranges from 5×5-7×7 depending of the nature of the deformation) that incorporates the full set of events identified with kART, irrespective of their energy barrier. Fig.4.8a shows the variation of C diffusion coefficient at the GB under isotropic pressure along the x, y and

z-axes at temperature 600 K. Fig.4.8b represents the Arrhenius plot for C diffusivity in GB. The calculated activation volume V^{act} , activation barrier E^{act} and diffusion prefactor D_0 are listed in the Appendix A Table S2. We find that it decreases (increases) linearly under lattice compression (expansion), but at different rates. Under lattice compression, as the pressure is increased from 0 to 12 kbar the diffusion coefficient of C at the GB is decreased by 1.39×10^{-13} m^2s^{-1} (net effective barrier increase: 0.068 eV), 5.30×10^{-14} m^2s^{-1} (net effective barrier increase: 0.01 eV) and 1.03×10^{-13} m^2s^{-1} (net effective barrier increase: 0.046 eV) for the isotropic, uniaxial and biaxial pressure respectively. On the other hand, under lattice expansion as the negative value of pressure is increased from 0 to 12 kbar the diffusion coefficient of C at the GB is increased by 4.95×10^{-13} m^2s^{-1} (net effective barrier decrease: 0.067 eV), 1.09×10^{-13} m^2s^{-1} (net effective barrier decrease: 0.020 eV) and 2.15×10^{-13} m^2s^{-1} (net effective barrier decrease: 0.047 eV) for the isotropic, uniaxial and biaxial pressure respectively.

Fig.4.8c compares the results for a similar set of calculations for the C diffusion coefficient at the GB and in the crystalline bulk under isotropic pressure at 600 K. We find that the applied pressure strongly affects C diffusivity at the GB as compared to bulk. At zero pressure, C diffusion at the GB is faster than in the crystalline bulk: the diffusion coefficient of C at GB is 1.94×10^{-13} m^2s^{-1} (corresponds to an effective barrier 0.772 eV), which is order of magnitude higher as compared with 2.65×10^{-14} m^2s^{-1} (corresponds to a barrier of 0.810 eV) in the crystalline bulk. The diffusivity of C at GB decreases rapidly as compared in bulk when isotropic pressure increases: as the pressure is increased from 0 to 12 kbar the diffusion coefficient of C at GB decreased by 1.39×10^{-14} m^2s^{-1} (net effective barrier increase: 0.068 eV) compared with 4.9×10^{-15} m^2s^{-1} (net barrier increase: 0.01 eV) in the crystalline bulk.

4.7. Discussion

To understand the impact of pressure on impurity diffusion at grain boundaries, we first establish a reference case by considering impurity diffusion in the bulk crystal under

isotropic, uniaxial and biaxial deformations. In agreement with simulations done on a system equilibrated at $T = 0$ K, [134] we find that the activation energy barrier increases under istropic pressure. We show that this leads to a non-linear reduction in the diffusion coefficient, as should be expected. A similar observation was made in experiments of vacancy-mediated In diffusion in Cu [84, 85], which suggest that this slowing down, in a dense metallic system is associated with the reduced space available along the diffusion pathway between two stable states.

Uniaxial and biaxial compressions, by breaking symmetry, introduce divergence in activation energy as a function of jump directions for the interstitial C, with some barriers decreasing while others increase under increasing pressure, leading to a non-monotonous effect of pressure on the diffusion coefficient, a phenomenon that does not seem to have been reported previously. This non-monotonous effect can be explained by the fact that, in addition to making the lattice stiffer, increasing pressure raises the formation energy for an interstitial. Along some diffusion directions, the enthalpy at the stable site increases faster than that at the transition state, leading to an effective reduction in the diffusion barrier.

These effects are made more complex at the grain boundary due to an increased richness in the energy landscape. This explains why results on various GBs differ. For example, Lojkowski *et al*, looking at In diffusion at a Cu grain boundaries, find that diffusivity increases with pressure [84, 85] while it decreases by an order of magnitude for Zn diffusing along tilt GBs in Al as the pressure is raised to 12 kbar[73].

Recently, Karki *et al.* [70] performed first-principles simulations, based on density functional theory, on the {310}/[001] tilt GB in MgO. They showed that native defects and impurities (Ca, Al, and proton) favorably segregate to the GB with the segregation considerably increasing with pressure. They also remarked that the impurity diffusion is faster at the GB as compared to the bulk as the pressure is increased as they showed that migration energies for host ions and impurities at the grain boundary are smaller than the bulk values, more so at higher pressures with their values being as low as 1.5 eV at 100 GPa compared to the bulk values of 4 eV.

Using kART, we obtain a more complete picture of the energy landscape of our system, C at the $85.91° < 100 >$ tilt GB. We find that, while segregation energy tends to become more favorable to the GB with respect to the bulk for a C interstitial with increasing isotropic pressure, the gain depends on specific sites, with some barely changing moving over a 24 kbar pressure change. Moreover, we observe that the orientation of pressure with respect to the GB changes the result : applying a pressure normal to the GB reduces the available free volume at the GB and, therefore, reduces the segregation energy, while a pressure parallel to the GB plane increases the formation enthalpy in the bulk while preserving a larger free volume, and increasing the energy gain of moving to the GB.

Pressure will also affect the various transition states differently as is shown in our detailed analysis of its effect for the three dominant transition states at the GB. While all three barriers increase linearly under increasing isotropic and normal pressure, albeit with a different slope, this is not the case for pressure applied parallel to the GB plane, which could, at high enough pressure, lead to a change in the dominant diffusion mechanisms and the overall diffusion. This suggests that inhomogeneities in materials, that can create large local pressure fluctuations, will increase the complexity of impurity diffusion and could favor mechanisms that are missed in analyses that do not explore the full landscape but could affect the overall properties of the material. kART provides a complete picture about evolution of C within a representative grain boundary under the influence of pressure, thus mimicking realistic working conditions and providing unique long-time description of the evolution of the system. The resulting full energy landscape on the impact of pressure on the C diffusion in iron once combined with surface phenomena can be regarded as one of the key parameters to determine the threshold and peak carburization rates of Fe surfaces.

4.8. Conclusions

Using the kinetic activation-relaxation technique, an off-lattice kinetic Monte Carlo method with on-the-fly catalog generation, we study pressure effect on the C diffusion in GB of α-iron providing detailed information regarding mechanisms and pathways that is

difficult to obtain through standard simulation methods. Our results show a richness in the diffusion mechanisms as well as a complex balance between elastic and chemical effects.

In particular, the effect of pressure can strongly modify the C stability and diffusivity in GB. These effects vary between isotropic and uniaxial pressure, with segregation energies of various metastable sites moving in opposite directions, in some cases. This can have a major impact on the evolution of heterogeneous materials, with variations of local pressure that would strongly alter diffusion across the material.

More work is required to better characterize this behavior and extract general rules. Clearly, additional simulations are needed to assess how multiple C interstial atoms or other defects such as vacancies and substitutional atoms diffuse at GBs under pressure; simulations are underway. The detailed analysis of the energy landscape provided by kART, however, shows that it is necessary to take specific mechanisms into account, with the possibility of developing precise control on the evolution of impurities in complex materials under local and global deformations.

4.9. Supplementary materials

see appendix A

4.10. Acknowledgment

This work has been supported by the Qatar National Research Fund (QNRF) through the National Priorities Research Program and the Canada Research Chairs program and by grants from the Natural Sciences and Engineering Research Council of Canada (NSERC). We are grateful to Calcul Québec/Compute Canada (CQ/CC) for generous allocations of computer resources.

4.11. Code availability

Various ART nouveau implementations are available freely for download from `http://normandmousseau.com`. The most recent packages for kART and ART nouveau are available freely from the authors upon request.

Chapter 5

Structural evolution of vacancy clusters in $\alpha-$iron: A kinetic activation-relaxation technique study

5.1. Objective

In this article, the stability of vacancy clusters in crystalline $\alpha-$iron and the processes associated with their aggregation and diffusion mechanisms are investigated. By using the power of the k- ART method, we have been able to study in detail all the activated events that determine the kinetics of such a system, and this for a very large number of configurations.

Authors in order: Md Mijanur Rahman, Fedwa El-Mellouhi, and Normand Mousseau

Status : This article has been submitted to the "Physical Review Materials" journal.

Author contributions:

- Md Mijanur Rahman (MMR) performed all simulations and data analysis.
- MMR wrote the first version of the article.
- MMR, Normand Mousseau (NM), and Fedwa El-Mellouhi (FEM) contributed to the writing of the article.
- NM supervised all this work.

5.2. Résumé

L'évolution des lacunes dans les matériaux est un facteur essentiel dans la détermination de leurs résistances physique et mécanique. Dans ce travail, nous étudions la diffusion des lacunes dans le fer α en utilisant la technique d'activation-relaxation cinétique (ARTc), une méthode de Monte Carlo cinétique hors réseau avec construction de catalogue à la volée basée sur l'activation-relaxation technique nouvelle (ARTn), couplée à un potentiel de méthode d'atomes embarqués (EAM). Nous nous concentrons sur l'évolution d'une à huit lacunes et fournissons, pour ces systèmes, une image détaillée du paysage énergétique, de la cinétique globale et des mécanismes de diffusion associés à ces défauts. Nous montrons les énergies de formation, les barrières d'activation pour l'état fondamental des huit systèmes et les barrières de migration pour la diffusion de ces systèmes. Cette étude dévoile une richesse dynamique insoupçonnée, même pour ce système simple, qui ne peut être découverte que par des approches globales et systématiques telles que la technique d'activation-relaxation cinétique. L'environnement énergétique complexe contrôlant la cinétique des petits amas de lacunes, que nous trouvons ici, démontre que des règles simples ne suffisent pas à développer une approche robuste de contrôle prédictif et de prévention des processus d'endommagement associés aux grappes de lacunes dans les métaux de structure.

5.3. Abstract

The evolution of vacancies in materials is a principal factor in the determination of their physical and mechanical strengths. In this work, we investigate vacancy diffusion in α-iron using the kinetic activation-relaxation technique (kART), an off-lattice kinetic Monte Carlo method with on-the-fly catalog building based on the activation-relaxation technique nouveau (ARTn), coupled with an embedded atom method (EAM) potential. We focus on the evolution of one to eight vacancies to provide a detailed picture of the energy landscape, overall kinetics, and diffusion mechanisms associated with these defects. We show formation energies, activation barriers for the ground state of all eight systems, and migration barriers for those diffuse systems. This study points to an unsuspected dynamic richness, even for this

simple system, which can only be discovered by comprehensive and systematic approaches such as the kinetic activation-relaxation technique. The complex energetic environment controlling the kinetics of small vacancy clusters, we find here, demonstrates that simple rules are not sufficient to develop a robust approach to predictive control and prevention of damage processes associated with vacancy clusters in structural metals.

5.4. Introduction

Vacancies, isolated and in clusters, are key defect structures for determining a material's physical and mechanical properties. Vacancies are created inside materials under deformation [106, 130], irradiation [16, 44, 55], or after quenching [109, 114]. Once formed, they can further aggregate and form nano-scale defects, such as stacking faults, cracks, voids, gas bubbles, dislocation loops, etc. [41, 127, 128, 129] The subsequent evolution of these defect structures strongly affects the material's properties, producing effects such as embrittlement, strengthening, crack resistance, ductility or creep behaviors [26, 30, 54, 156], which can lead to property degradation and possibly component failure. Thus, understanding the formation and evolution of vacancy clusters is an interesting topic for materials used in extreme environments.

Despite decades of extensive research, understanding the formation and evolution of vacancy clusters remains a formidable challenge. The atomic-scale details of vacancy cluster diffusion are generally difficult to observe experimentally. Thus, atomistic simulations are needed to understand the interaction and migration of vacancy clusters at this scale. For this, however, we need a proper description, using either *ab initio* approaches or accurate empirical potentials, as well as comprehensive sampling methods. *Ab initio* calculations based on density functional theory (DFT) [75] provide an accurate approach to investigating atomic details and therefore have been used in numerous studies on vacancy clusters [32, 37, 46, 61, 69, 140, 148]. However, due to their costs, these methods offer a limited capacity to sample energy landscape and most work limit themselves to finding a transition state between given initial and final states based on an initial guess for the connecting

trajectory. Only the pathway closest to the initial guess is explored, leaving other possible pathways unexplored. This can be problematic with complex energy landscapes, where multiple nontrivial but relevant pathways may be present. Moreover, DFT methods are too expensive to apply to large systems or to allow extensive sampling. While standard simulation tools such as molecular dynamics [3] coupled with empirical potentials could provide useful information on atomistic details of these diffusion mechanisms, they often cannot reach the extended time scale over which many of these processes occur. Kinetic Monte Carlo approaches [142, 146] provide a solution to reaching longtime dynamics; however, the standard implementation requires an upfront knowledge of the relevant barriers and cannot consider crucial elastic deformations. While results from such simulations are enlightening, their quantitative validity is limited since the full details of local atomic configurations can significantly affect diffusion kinetics. This is why we need a method such as the kinetic Activation Relaxation Technique (kART) [40, 103], a unique off-lattice kinetic Monte Carlo algorithm with on-the-fly catalog-building capabilities, which lifts those limitations and allows us to map these processes in detail. kART ensures an efficient and extensive sampling of energy landscapes as it incorporates exact elastic effects at both minima and saddle points for a precise kinetic description of complex materials ranging from defects in metals to the long-time evolution of amorphous materials.

In this study, we focus on vacancy cluster diffusion in α-Fe, a central component of the ferritic steels widely used in aeronautic and nuclear industries. This system has received considerable attention over the years [11, 18, 21, 36, 38, 46, 49, 50, 62, 69, 76, 94, 95, 120, 125, 147], with main efforts going towards elucidating the structure of the vacancy clusters formed during deformation or irradiation. It is well-known, for example, that the most common vacancy clusters in α-Fe are cavities [62, 94]. However, their formation mechanism and kinetic evolution are less well understood. An extensive characterization of vacancy cluster formation and possible diffusion pathways is still missing. Such a work would provide a complete picture of the various diffusion mechanisms and evaluate the possible richness of the energy landscape associated with this phenomenon.

For this purpose, we employ k−ART, coupled with a reliable and well−tested embedded atom method (EAM) potential, to achieve this goal. Using this approach, we characterize the associated energy landscape and clustering mechanisms of vacancy clusters. We focus, more specifically, on the diffusion and clustering of one to eight vacancies in crystalline α−iron. We show that even these simple assemblies, from one to eight vacancies, can present complex reorganizations that considerably affect their diffusion properties. The paper is organized as follows: the methodology, including a brief overview of k−ART, the model employed, and the computational details, are presented in Sec. II. Then, simulation results are presented and discussed in Secs. III and IV, respectively. Finally, the conclusion is given in Sec. V.

5.5. Methodology

5.5.1. Kinetic-Activation Relaxation Technique (kART)

kART is a kinetic Monte Carlo algorithm with on-the-fly event catalog building capacity and exact elasticity treatment. While details of kART implementation can be found elsewhere [13, 40, 102], here we provide a brief overview of the basic algorithm and the specific parameters used in this study.

At the beginning of each KMC step, the local environment surrounding each atom is characterized by its local topology. kART generates a local connectivity graph involving each atom and its surroundings. Here, we use a cutoff of 2.7 Å for drawing a link between two atoms and a radius of 6.0 Å around the central atom for the maximum graph size. Graphs are then analyzed using the NAUTY[97] package, a topological analysis package that it used to provide a unique identifier associated with the graph's automorphic group and the permutations allowing to restore of the reference graph. If the topology is known, events related to it are recovered from the catalog and placed in a KMC tree; otherwise, the catalog is updated by launching a series of activation-relaxation technique nouveau (ART nouveau or ARTn) [7, 88, 93] searches to identify the diffusion mechanisms associated with this topology. Once the catalog is fully updated and the tree is completed for the current

atomistic configuration, generic events are ordered according to their rate, defined as

$$\Gamma_i = \nu_0 e^{-\frac{E_b}{k_B T}} \tag{5.5.1}$$

where ν_0 is a fixed prefactor which is fixed at 10^{13} Hz and E_b, the activation energy for the event i defined as the energy difference between the transition state and the initial minimum[42, 43, 78]. Once the event tree is completed, the lowest-energy barrier events that make up to 99.99 % of the rate are fully reconstructed and reconverged into specific events. In this manner, low barriers are fully relaxed according to actual geometry and, therefore, exactly include short and long-range elastic effects. Then the specific rates and overall KMC time step are estimated again with the refine barriers. Finally, the event is selected according to the standard KMC algorithm[146]. The elapsed time t is computed according to a Poisson distribution as

$$t = -\frac{\ln \mu}{\sum_i \Gamma_i} \tag{5.5.2}$$

where μ is a random number uniformly distributed between 0 and 1. To avoid being trapped by low barrier events associated with non-diffusive mechanisms, we use the basin accelerated mean-rate method (bacMRM) [13, 112], which solves them analytically. To fully characterize the kinetics on all relevant time scales, we start all simulations with a basin threshold of 0.1 eV and increase it as flickering occurs.

5.5.2. Force fields

Force fields are calculated with the Large-Scale Atomic/Molecular Massively Parallel Simulator (LAMMPS) [1, 111] by linking its library to kART. To speed up the computation, we use double parallelization to generate events and force calculations on multiple processors. In the present study, we use the Fe-C EAM potential developed by Becquart *et al.* [10, 138] for Fe-C and Ackland and Mendelev [100] for Fe-Fe interactions. Both potentials provide an excellent agreement with DFT calculations in bulk Fe.

5.5.3. Simulation details

We characterize the diffusion pathways of vacancy clusters in a perfect cubic bcc bulk crystal containing 2000 Fe atoms with periodic boundary conditions. The supercell is oriented in the cubic directions, i.e. x in [100], y in [010], and z in [001]. For each system containing one to five and eight vacancies, we perform runs at 600K, as defined in the calculation of the rate. The variation in the total energy of the system containing the largest cluster as a function of the box size was checked to ensure the size was sufficiently large. In all cases, the simulation box is a cubic box with a length of 28.553 Å, corresponding to a lattice parameter of 2.8553 Å in agreement with the literature for the BCC Fe structure. The system's energy is first minimized at $T = 0$ K using LAMMPS before kART simulations are launched.

The ground state (GS) energy is defined for each simulation as the lowest energy minimum identified during the run, E_{GS}. The activation energy for an event is defined as the energy difference between the initial minimum E_{min} and the adjacent saddle E_{sad} (i.e., the barrier crossed between two adjacent minima) or

$$E_b = E_{sad} - E_{min}. \tag{5.5.3}$$

The migration energy is defined as the difference between the energy of the highest saddle point crossed along a path connecting one local minimum to another and E_{min}.

The square displacement (SD) is computed as usual:

$$SD = \sum_{i}^{N} (r_i(t_n) - r_i(0))^2, \tag{5.5.4}$$

where N is the number of vacancies and $r_i(t_n)$, the position of vacancy i at KMC step n.

To describe the energy cost for the formation of a vacancy cluster with respect to the perfect lattice, the formation energy per vacancy for the n-vacancy cluster is defined as

$$E_{nv}^f = \frac{E_{nv}^F}{n} = \frac{1}{n}(E_{N-n}^{tot} - \frac{N-n}{N} E_N^{tot}), \tag{5.5.5}$$

where E^F_{nv} is the formation energy for an n-vacancy cluster, E^{tot}_{N-n} is the total energy of the supercell with (N–n) atoms and an n-vacancy cluster, and $E^{tot}_N = -8025.965$ eV is the total energy of the corresponding defect-free supercell containing N atoms (2000 atoms in our case).

To compare the thermodynamic stability of line dislocation, the binding energy per vacancy for the n-vacancy cluster is given by

$$E^b_{nv} = \frac{1}{n}(\sum_n E^f_{1v} - E^F_{nv}) = E^f_{1v} - E^f_{nv} \tag{5.5.6}$$

where $E^f_{1v} = 1.722$ eV is the formation energy of an isolated vacancy. Positive binding energy indicates a preference for the n-isolated vacancies to form an n-vacancy cluster, and higher binding energy denotes greater stability.

5.5.4. Vacancy structure notation

The complex vacancy configurations are described in terms of the vacancy-pair separation distances. The number of vacancy pairs in a m-vacancy structure is $P(m) = m!/\,(2!(m-2)!)$. For example, the bound structure of the tri-vacancy complex has $P(3) = 3!/(2! \times 1!) = 3$ vacancy pairs. Using d_i to represent the separation distance between two vacancies that are i-th neighbors, the bound structure of the m-vacancy complex can be described by these distances: $mV(N_{d_1}, N_{d_2}, N_{d_3}, N_{d_4}, N_{d_5}, N_{d_6})$, where N_{d_i} is the total number of i-th nearest-neighbor (NN) distances between pairs of vacancies in the structure. For instance, 3V(2,1,0,0,0,0) illustrates the bound cluster configuration with two 1NN and one 2NN vacancy-pair separation distances.

As discussed below, the binding energy for divacancies in the fifth and sixth neighboring configurations is below room temperature (at -0.021 and -0.011 eV, respectively). The inclusion of positions in the fifth and sixth neighbors is therefore sufficient to describe the aggregation kinetics.

5.5.5. Calculation of lifetimes

To study the vacancy cluster lifetime and diffusivity, we construct a complete transition matrix that allows recovering the associated rate of all the possible states where the system can move from the ground state until the system reaches a state where one of the vacancies in it moved further away than the fourth nearest-neighbour (4NN) distance from any of the remaining cluster vacancies.

The diffusion coefficient and thermal lifetime are calculated using the Markov chain solution described as follows:

(1) choose the ground state for a vacancy cluster of that size as initial state i;

(2) generate a uniform random number u ϵ (0,1];

(3) select the next event j probabilistically such that $\sum_k^{j-1} p_{ik} < u \leq \sum_k^j p_{ik}$, where, p_{ik} is the probability to jump from state i to state k ;

(4) update the current state j $\rightarrow$ i;

(5) generate a second uniform random number μ ϵ (0,1];

(6) update times as, $\tau = \tau - \frac{\ln \mu}{\sum_k \Gamma_k}$, where, Γ_k is the transition rate from state i to state k;

(7) return to step 2.

The lifetime of the cluster is defined as the time at which one of the vacancies in it moves further away than the 4NN distance from any of the remaining cluster vacancies. Cluster mobility is studied by tracing the diffusion of the cluster. The same simulation is repeated $N_{sim} = 5$ million times in order to obtain sufficient statistics. The diffusion coefficient is calculated as

$$D = \frac{1}{N_{sim}} \sum_i^{N_{sim}} \frac{R_i^2}{6\tau_i}, \tag{5.5.7}$$

where R_i^2 is the squared displacement during the lifetime τ_i, of the cluster, in simulation i.

5.6. Results

5.6.1. Validation

As a validation test, we analyze the diffusion of a single Fe vacancy. The formation energy of monovacancy calculated using EAM potential is 1.722 eV, consistent with previous simulations and experimental results (see Table.2 in Ref.[95]). The vacancy self-diffusion takes place through a first nearest-neighbor (1NN) jump with 100% probability. This 1NN jump occurs either through a direct transition, from the ground state, GS (at $E_{GS} = -8020.231$ eV) to a new GS by crossing an energy barrier of 0.64 eV, or in two steps, from the GS to a metastable state at $E_{min} = 0.549$ eV above the GS by crossing an energy barrier of 0.64 eV, from this state a second barrier with a 0.091 eV energy brings the system back into a new GS. The barrier heights agree with literature values [69, 95].

For further validation, the interactions between two vacancies are analyzed, as they are position in the first, second, third, fourth, fifth, and sixth nearest neighbor sites of each other (denoted as 1NN, 2NN, 3NN, 4NN, 5NN, and 6NN sites). The interaction for the 2NN state is strongly attractive (with a binding energy of approximately 0.240 eV), as seen in previous studies [18, 37, 69], while it is only slightly attractive for the 1NN and 4NN states (with a binding energy of 0.141 eV and 0.029 eV, respectively). For their part, 3NN, 5NN, and 6NN sites show a negative binding energy of -0.022 eV, -0.021 eV, and -0.011, respectively, indicating a repulsive interaction. For larger clusters, the most stable configurations tend to maximize the number of 2NN and 1NN vacancy pair-separation distances.

5.6.2. Structure and stability

To proceed further, we analyze the thermal stability of the clusters, which are classified into three groups according to the shape characteristics of the initial clusters: linear, planar, and body clusters. Vacancies in the linear clusters are positioned along either [100], [110], or [111] directions, respectively. The planar clusters lie on the [110] plane. The body clusters are separated into two groups: tetrahedral type, with tetrahedral features or s combination

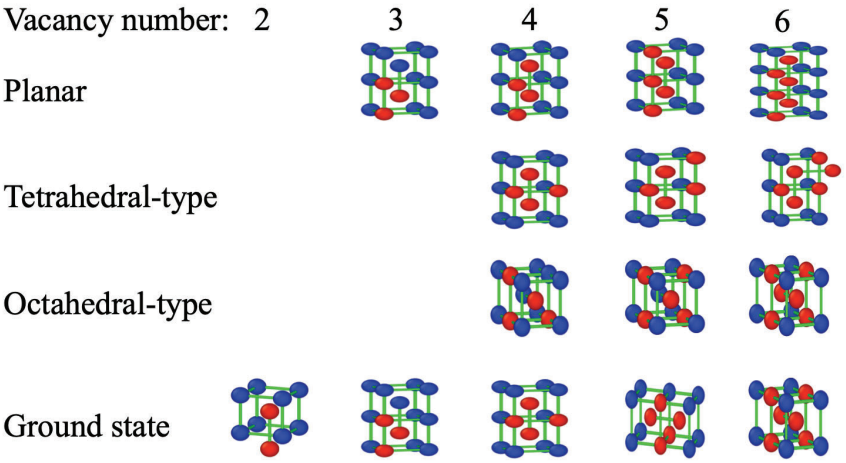

Fig. 5.1. Schematic representation of the configurations for planar and body clusters with one to six vacancies. Blue and red circles represent crystalline Fe atoms and vacancies, respectively.

Table 5.1. Formation energies (E^F_{nv}), binding energies (E^b_{nv}), and migration energies (in eV) for pathways between the six dominant bound states for the di-vacancy complex.

From / To	1NN	2NN	3NN	4NN	5NN	6NN
E^F_{nv}	3.303	3.204	3.466	3.415	3.465	3.455
E^B_{nv}	0.141	0.240	-0.022	0.029	-0.021	-0.011
1NN	-	0.716	0.694	-	0.577	-
2NN	0.617	-	-	0.429	-	-
3NN	0.857	-	-	0.676	-	-
4NN	-	0.641	0.626	-	0.589	0.630
5NN	0.738	-	-	0.638	-	-
6NN	-	-	-	0.670	-	-

of the tetrahedron; and octahedral type, which tends to form octahedral structure based on the relevance of cluster structures. The configurations for the planar and body clusters with 2–6 vacancies are shown in Fig. 5.1.

Fig. 5.2 presents the formation and binding energies per vacancy for different cluster types as functions of vacancy number. The binding energy generally increases with the vacancy number for each cluster type, indicating the preference for further cluster growth. Moreover, the binding energies for the tetrahedral- and octahedral-type clusters are higher and have larger energy gradients. In contrast, the binding energies of the linear and planar clusters are lower and have smaller gradients. This is expected as the tetrahedral- and octahedral-type clusters, with lower surface to volume ratio, should be more stable and have higher growth tendencies.

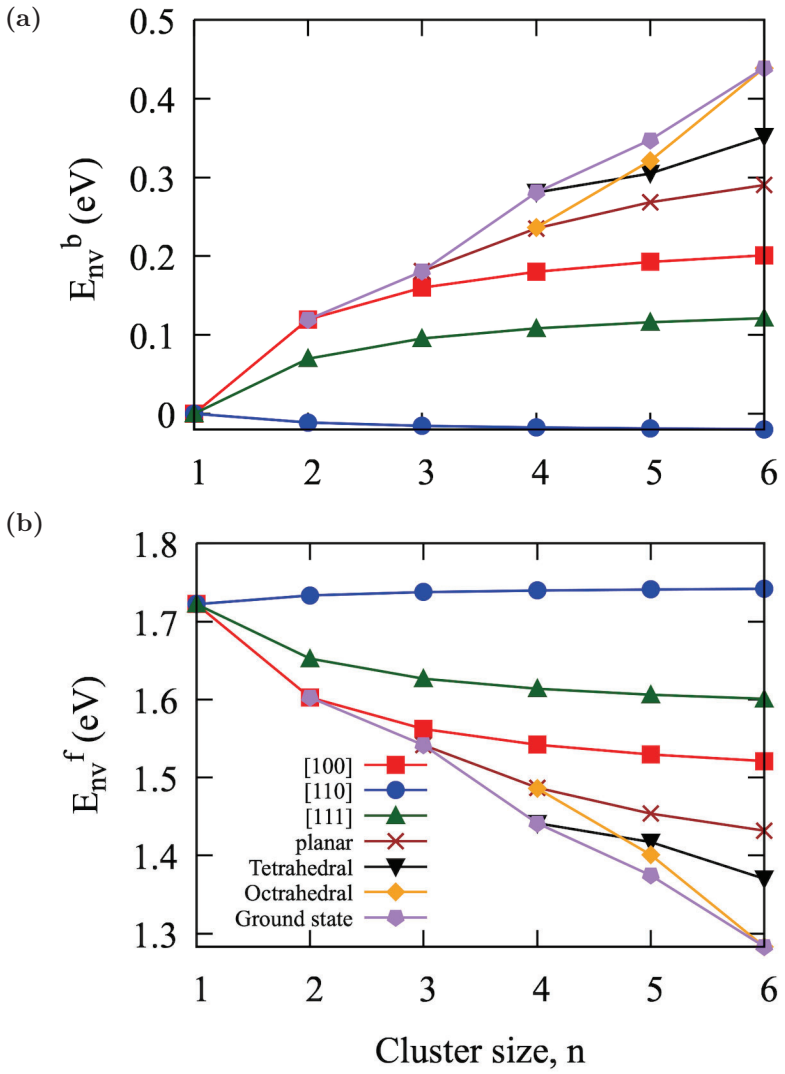

Fig. 5.2. (a) Binding energies and (b) formation energies for different vacancy cluster types in α-iron.

5.6.3. Small vacancy clusters (2-4 vacancies)

We now turn to vacancy aggregation and diffusion mechanisms of small vacancy clusters containing two to four vacancies. Simulations start with the defects placed at a large enough distance (around 10.2 Å) from each other to ensure minimal interaction. The detailed activation energy, binding energy at the local minima, and squared displacement as a function of time for two to four Fe vacancies in a bcc crystal at 600K are shown in Fig. 5.3. The selected and sampled activation energies as a function of the KMC step, as well as the number of

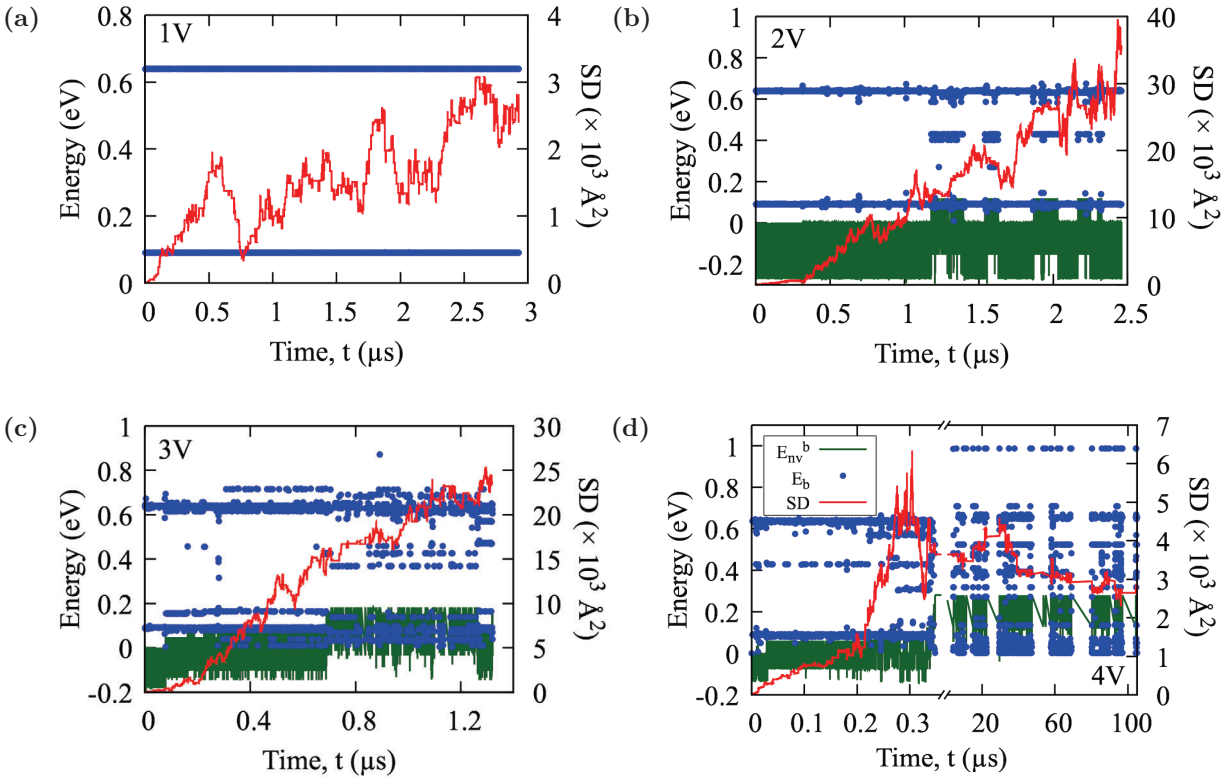

Fig. 5.3. Activation-energy (left, blue symbols), binding energy at the local minima (left, green line) and squared displacement (right, red line) as a function of time for one to four Fe vacancies in a bcc crystal at 600K: (a) one, (b) two, (c) three, and (d) four vacancies.

Table 5.2. Formation energy (E^F_{nv}) and migration energies (in eV) for pathways between the eight dominant bound states for the tri-vacancy complex. The bound structures of the tri-vacancy complex are defined as $3V(N_{d_1}, N_{d_2}, N_{d_3}, N_{d_4}, N_{d_5}, N_{d_6})$, where N_{d_1}, N_{d_2}, N_{d_3}, N_{d_4}, N_{d_5}, and N_{d_6} represent the total number of 1NN, 2NN, 3NN, 4NN, 5NN, and 6NN vacancy-pair separation distances, respectively.

From / To	3V(2,1,0,0,0,0)	3V(0,2,0,0,0,1)	3V(0,2,1,0,0,0)	3V(1,1,0,1,0,0)	3V(0,1,0,2,0,0)	3V(1,0,0,1,1,0)	3V(0,0,0,2,1,0)	3V(0,0,1,2,0,0)
E^F_{nv}	4.625	4.685	4.709	4.780	4.867	5.031	5.127	5.128
3V(2,1,0,0,0,0)	0.653	-	0.605	0.475	-	0.364	-	-
3V(0,2,0,0,0,1)	-	-	-	-	-	-	-	-
3V(0,2,1,0,0,0)	0.691	-	-	0.60	0.461	-	-	0.233
3V(1,1,0,1,0,0)	0.631	-	0.671	-	0.521	-	-	-
3V(0,1,0,2,0,0)	-	-	0.619	0.608	-	-	0.380	0.415
3V(1,0,0,1,1,0)	0.773	-	-	-	-	-	-	-
3V(0,0,0,2,1,0)	-	-	-	-	0.640	-	-	-
3V(0,0,1,2,0,0)	-	-	0.653	-	0.676	-	-	-

events in the catalog per step for events involving vacancy movement, are shown in Appendix B, Fig.B.1. The schematic representation and energetic descriptions of the dominant diffusion mechanisms are shown in Fig. 5.4.

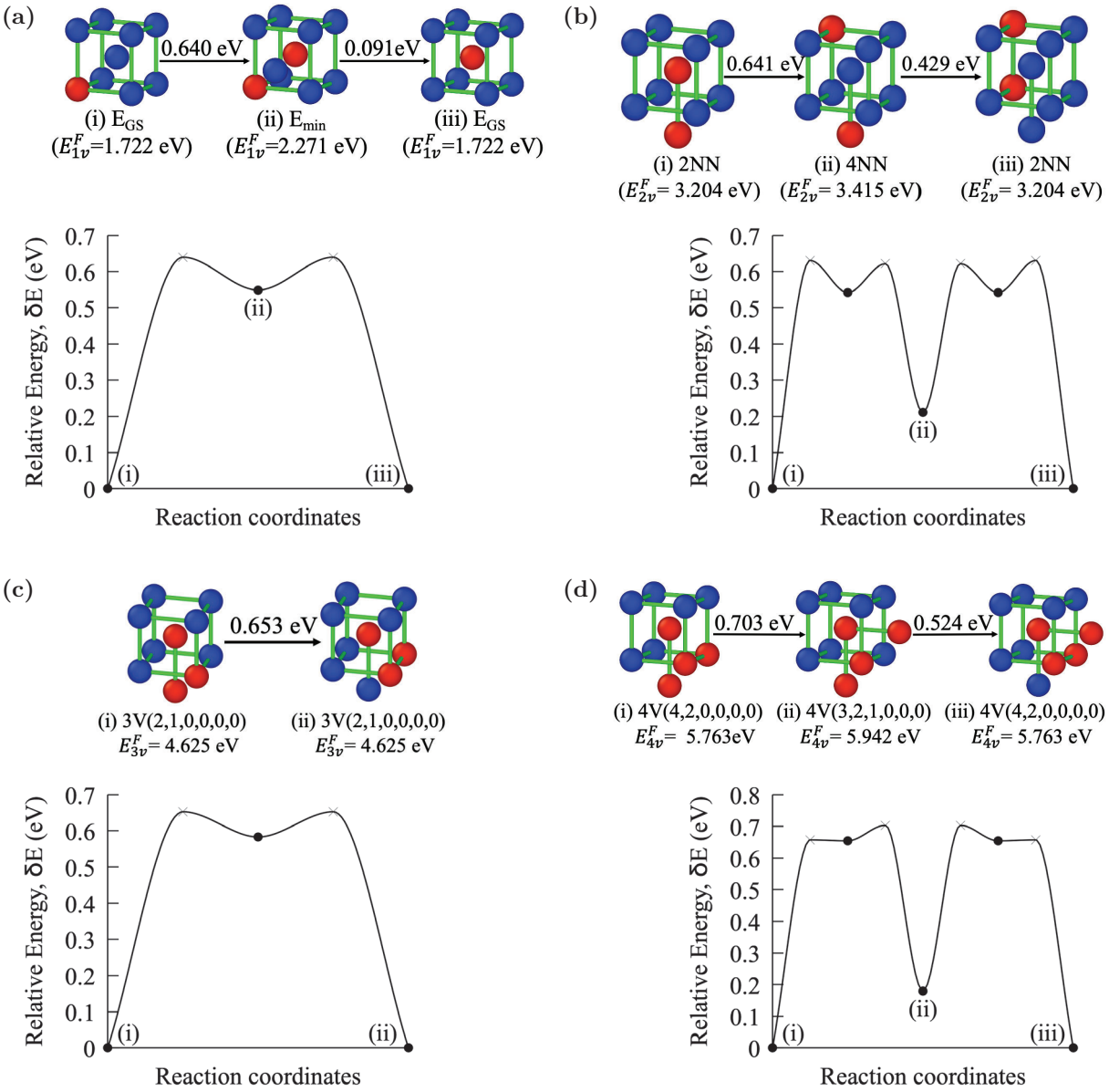

Fig. 5.4. Schematic representation and energetic descriptions of the dominant diffusion path for (a) one, (b) two, (c) three, and (d) four vacancies in bcc Fe at 600K. In the schematic diagrams, the blue and red spheres represent crystalline Fe atoms and vacancies, respectively. In the energetic description, the cross and filled circle represent the saddle points and minima, respectively. The indices (I, II, and III) are used to identify states and explain the diffusion mechanism. The bound structures of three and four vacancies are indicated as $3V(N_{d_1}, N_{d_2}, N_{d_3}, N_{d_4}, N_{d_5}, N_{d_6})$ and $4V(N_{d_1}, N_{d_2}, N_{d_3}, N_{d_4}, N_{d_5}, N_{d_6})$, respectively. Where N_{d_1}, N_{d_2}, N_{d_3}, N_{d_4}, N_{d_5}, and N_{d_6} represent the total number of 1NN, 2NN, 3NN, 4NN, 5NN, and 6NN vacancy-pair separation distances, respectively.

Due to elastic interactions, the two vacancies aggregate rapidly, in less than 1.2 μs and 2173 KMC steps, into a dimer with two-point defects at a 2NN distance from each other,

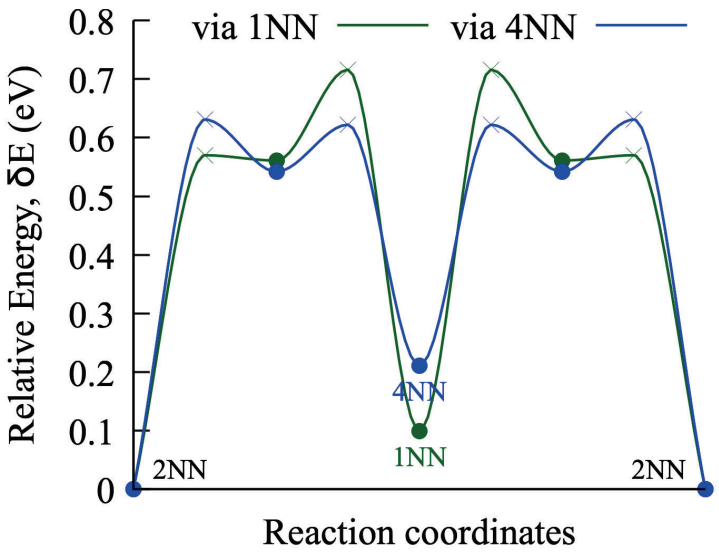

Fig. 5.5. Energetic descriptions of the migration between 2NN to 1NN(green) and 2NN to 4NN (blue) for di-vacancy. The Cross and filled circle represent the saddle points and minima, respectively.

Table 5.3. Formation energy (E^F_{nv}) and migration energies (in eV) for pathways between the ten dominant bound states for the tetra-vacancy complex. The bound structures of the tetra-vacancy complex are defined as $4V(N_{d_1}, N_{d_2}, N_{d_3}, N_{d_4}, N_{d_5}, N_{d_6})$, where N_{d_1}, N_{d_2}, N_{d_3}, N_{d_4}, N_{d_5}, and N_{d_6} represent the total number of 1NN, 2NN, 3NN, 4NN, 5NN, and 6NN vacancy-pair separation distances, respectively.

From / To	4V(4,2,0,0,0,0)	4V(3,2,1,0,0,0)	4V(3,2,0,1,0,0)	4V(4,1,1,0,0,0)	4V(2,2,0,2,0,0)	4V(2,2,1,1,0,0)	4V(3,1,0,1,1,0)	4V(3,1,1,1,0,0)	4V(1,2,1,2,0,0)	4V(2,1,1,1,1,0)
E^F_{nv}	5.763	5.942	5.945	6.014	6.093	6.127	6.195	6.196	6.262	6.376
4V(4,2,0,0,0,0)	-	0.524	-	0.555	-	0.410	-	-	-	0.376
4V(3,2,1,0,0,0)	0.703	-	0.483	0.407	0.498	-	-	0.272	-	-
4V(3,2,0,1,0,0)	-	0.485	-	-	-	0.478	-	-	0.373	-
4V(4,1,1,0,0,0)	0.804	0.479	-	-	-	-	-	-	-	0.284
4V(2,2,0,2,0,0)	-	0.648	-	-	-	-	-	-	0.432	-
4V(2,2,1,1,0,0)	0.773	-	0.660	-	-	0.511	0.595	-	-	-
4V(3,1,0,1,1,0)	-	-	-	-	-	0.664	-	-	-	0.389
4V(3,1,1,1,0,0)	-	0.525	-	-	-	-	-	-	-	0.318
4V(1,2,1,2,0,0)	-	-	0.690	-	0.619	-	-	-	0.377	-
4V(2,1,1,1,1,0)	0.988	-	-	0.654	-	-	0.570	0.499	-	0.318

representing the ground state. Table 5.1 summarizes the energy landscape for the di-vacancy complex, providing information regarding formation, binding, and migration energies for states with vacancies in the 1st to 6th nearest neighbor positions. The di-vacancy migrates through two dominant processes, where the configuration changes from the second nearest neighbor (GS) to the first nearest neighbor and back to the second nearest neighbor and from the second nearest neighbor to the fourth nearest neighbor and back to the second nearest neighbor. The energy barrier for each of these migration paths is shown in Fig. 5.5,

where the green line represents the energy barrier for migration via the first nearest-neighbor configuration, and the blue line represents the energy barrier for migration via the fourth nearest-neighbor configuration. Mostly, the di-vacancy migrates by oscillating between the 2NN and 4NN states, with an energy barrier of 0.641 eV. The 1NN pathway may be expected to be the dominant mechanism, as one may predict the transition to the lower-energy 1NN state to have a lower energy barrier. However, the 2NN to 1NN transition has an energy barrier of 0.716 eV, making it kinetically less favorable. The diffusion mechanisms and barrier heights match previous studies using either ab initio approaches or empirical potentials[37].

The three isolated vacancies aggregate to form the ground state in 0.71 μs and 1583 KMC steps, with two 1NN and one 2NN vacancy pair-separation distances, forming an isosceles triangle. This cluster is characterized by a binding energy of 0.68 eV (0.23 eV per vacancy) as measured from the three isolated vacancies. Once vacancies reach the ground state, eight configurations dominate the dynamics of the system, representing more than 95 % of all accepted configurations. Table 5.2 summarizes the energy landscape for the eight most stable tri-vacancies bound compounds, providing information regarding formation, and migration energies for states. For simplicity, These bound structures of the tri-vacancy complex are defined as 3V(a,b,c,d,e,f), where a, b, c, d, e, and f represent the total number of 1NN, 2NN, 3NN, 4NN, 5NN, and 6NN vacancy pair-separation distances, respectively. For instance, 3V(2,1,0,0,0,0) illustrates the bound cluster configuration with two 1NN and one 2NN vacancy pair-separation distances. The dominant diffusion mechanism for the tri-vacancy bound compound is a one-step process associated with a rotation that involves migrating one vacancy from the ground state to a first neighbor site without breaking the triangle, crossing a barrier of 0.653 eV shown in Fig. 5.4. The barrier height is in good agreement with previous literature results [11, 69]. The cluster is stable and can be broken only by crossing a 0.691 eV barrier, which involves migrating a vacancy to a nearest-neighbor site forming a complex of two 2NN and one 3NN vacancy pair-separation distance, 0.084 eV above the GS. Then from this state, the system is back into a new GS by crossing a second barrier with an energy of 0.605 eV.

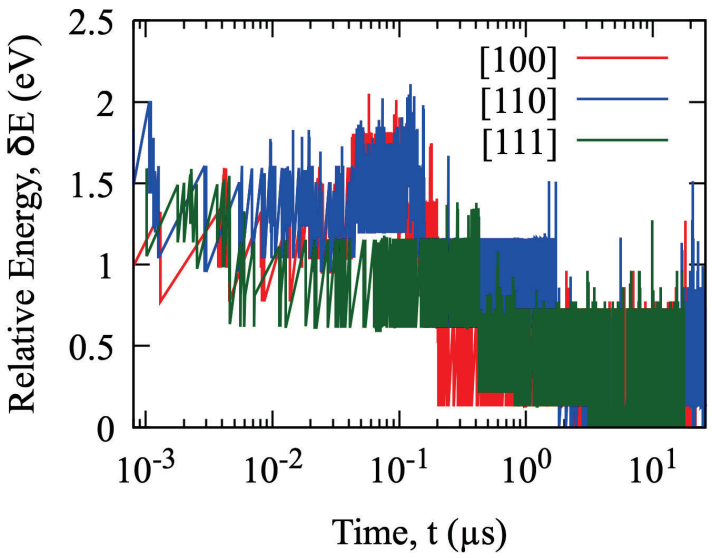

Fig. 5.6. Energy evolution of five vacancies as a function of time at 600K: red, blue, and green lines for initial line dislocation structures along [100], [110], and [111], respectively.

Starting from four isolated vacancies, the ground state for the tetra-vacancy is reached in about 0.51 μs and 1482 KMC steps. The ground state is characterized by four vacancies forming a complex of four 4NN and two 2NN vacancy pair-separation distances. As measured from four isolated vacancies, the binding energy for the ground state is 1.36 eV or 0.34 eV per vacancy. Table 5.3 summarizes the energy landscape for most ten stable tetra-vacancies bound compounds, providing information regarding formation, and migration energies for states. The dominant diffusion mechanism for the tetra-vacancy complex is described in Fig. 5.4. Diffusion takes place in two steps by the migration of one vacancy that jumps to 1NN position at each step. From the ground state, the system reaches a higher energy state at 0.179 eV above the GS by crossing an energy barrier of 0.703 eV; from this state, a second barrier with an energy of 0.524 eV brings the system back into a new GS. The barrier height we find here agrees with the previous literature values using different empirical potentials [36].

5.6.4. 5-vacancy cluster

Having characterized the vacancies aggregation and diffusion mechanism of small vacancy clusters containing two to four vacancies, we now look at the energy landscape and diffusion

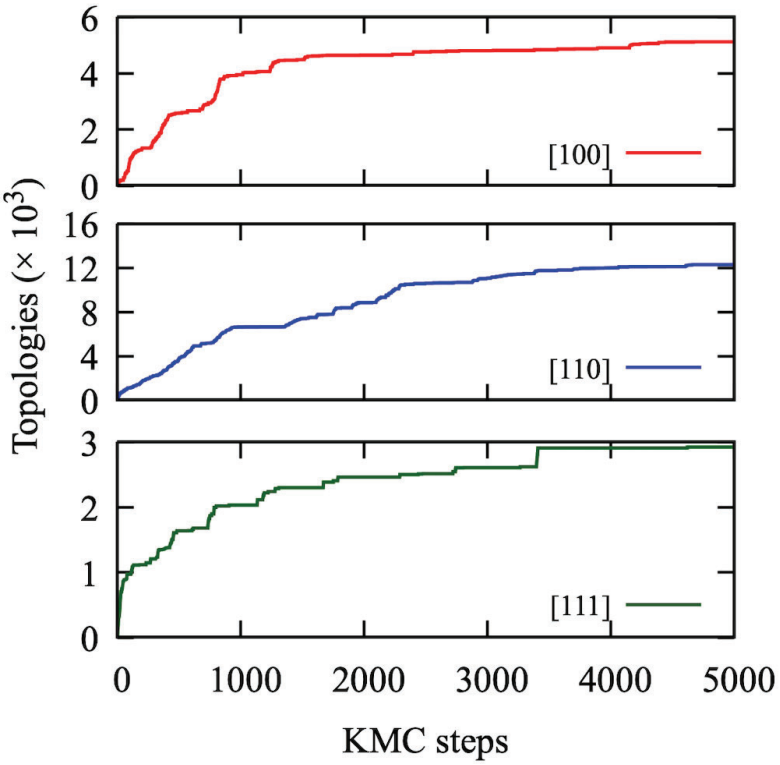

Fig. 5.7. Evolution of the number of topologies as a function of KMC steps for initial line dislocation contains five vacancies along [100] (top), [110] (middle), and [111] (bottom).

Table 5.4. Formation energy (E^F_{nv}) and migration energies (in eV) for pathways between the ten dominant bound states for the Penta-vacancy complex. The bound structures of the penta-vacancy complex are defined as $5V(N_{d_1}, N_{d_2}, N_{d_3}, N_{d_4}, N_{d_5}, N_{d_6})$, where N_{d_1}, N_{d_2}, N_{d_3}, N_{d_4}, N_{d_5}, and N_{d_6} represent the total number of 1NN, 2NN, 3NN, 4NN, 5NN, and 6NN vacancy-pair separation distances, respectively.

From / To	5V(6,3,1,0,0,0)	5V(4,4,2,0,0,0)	5V(5,3,1,1,0,0)	5V(4,3,0,2,0,1)	5V(4,3,2,0,1,0)	5V(4,3,1,2,0,0)	5V(5,2,2,1,0,0)	5V(3,3,3,1,0,0)	5V(4,2,2,2,0,0)	5V(0,5,4,0,1,0)
E^F_{nv}	6.873	7.002	7.084	7.234	7.257	7.258	7.333	7.468	7.497	7.509
5V(6,3,1,0,0,0)	-	0.509	0.528	-	-	-	0.348	0.429	-	
5V(4,4,2,0,0,0)	0.638	0.803	-	-	-	0.293	-	-	0.412	0.480
5V(5,3,1,1,0,0)	0.740	-	0.513	0.501	-	0.621	0.477	0.363	0.381	-
5V(4,3,0,2,0,1)	-	-	0.651	-	-	-	0.623	-	-	-
5V(4,3,2,0,1,0)	-	-	-	-	-	-	0.477	-	-	0.574
5V(4,3,1,2,0,0)	-	0.548	0.795	-	-	-	0.429	-	0.362	-
5V(5,2,2,1,0,0)	0.808	-	0.726	0.723	0.552	0.504	-	0.590	0.268	-
5V(3,3,3,1,0,0)	1.024	-	0.748	-	-	-	0.725	-	-	-
5V(4,2,2,2,0,0)	-	0.906	0.794	-	-	0.601	0.432	-	-	-
5V(0,5,4,0,1,0)	-	0.987	-	-	0.826	-	-	-	-	-

mechanisms for five-vacancy clusters. kART simulations are launched from line dislocation oriented in three crystallographic orientations constructed by removing five atoms at [100], [110], and [111] directions, respectively, from the 2000-atom box. Each system is run for 5000 KMC steps, representing 21.8 μs, 25.9 μs and 17.7 μs of simulation time at 600 K for

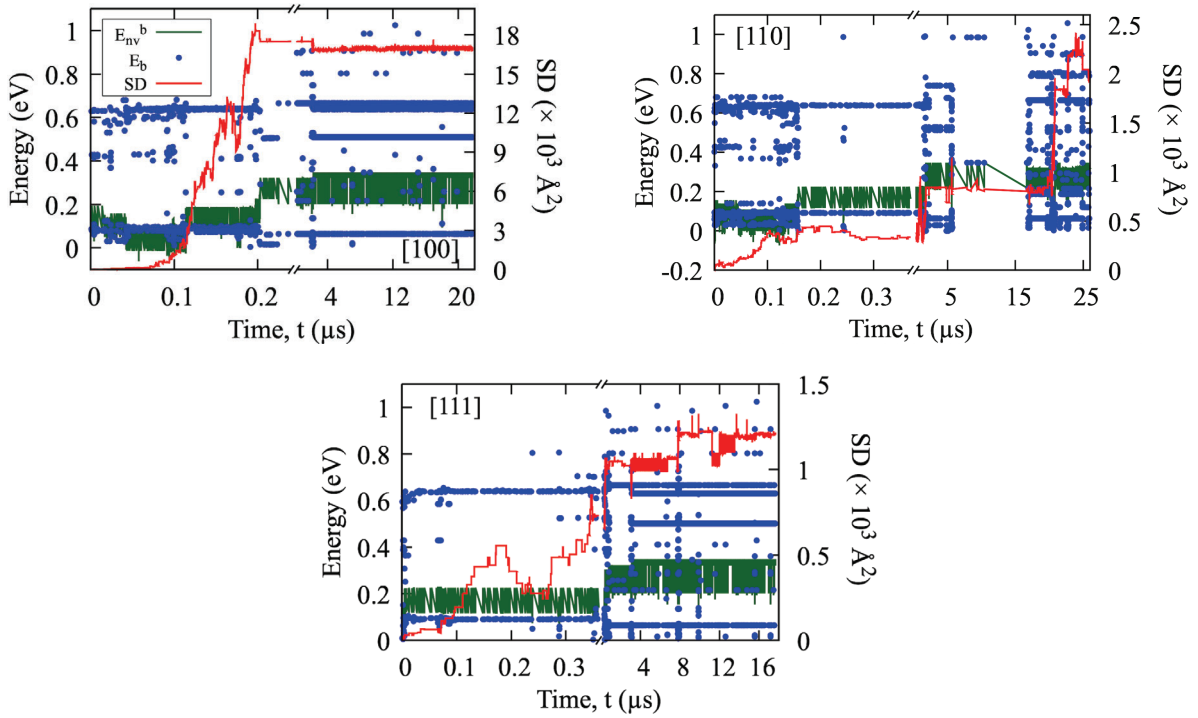

Fig. 5.8. Activation-energy (left, blue symbols), binding energy at the local minima (left, green line) and squared displacement (right, red line) as a function of time for the line dislocation of five vacancies along [100] (top left), [110] (top right), and [111] (bottom center) direction in a bcc Fe at 600K.

$LD^5_{[100]}$, $LD^5_{[110]}$ and $LDS^5_{[111]}$, respectively, which allows the complete characterization of the dynamic evolution of these defects.

Fig.5.7 represents the cumulative topologies as a function of KMC step. At the end of the simulations for $LD^5_{[100]}$, $LD^5_{[110]}$, and $LD^5_{[111]}$ systems, 5122, 12296 and 2923 topologies in total are analyzed for new events over 5000 KMC steps, respectively. Among these topologies, the number of unique topologies visited for $LD^5_{[100]}$, $LD^5_{[110]}$ and $LD^5_{[111]}$, are 219, 550, and 139, respectively. There are two main features of the cumulative topology plot, which can be described as the exploration of new topologies or oscillations between already encountered topologies. The exploration of new topologies is illustrated by the increase in cumulative topologies, where the simulation visits unexplored configurations. Plateaus on the topology curve indicate the recycling of topologies already encountered.

Figs. 5.6 and 5.8 present the energy evolution and the detailed activation energy, binding energy at the local minima, and squared displacement as a function of time at 600 K,

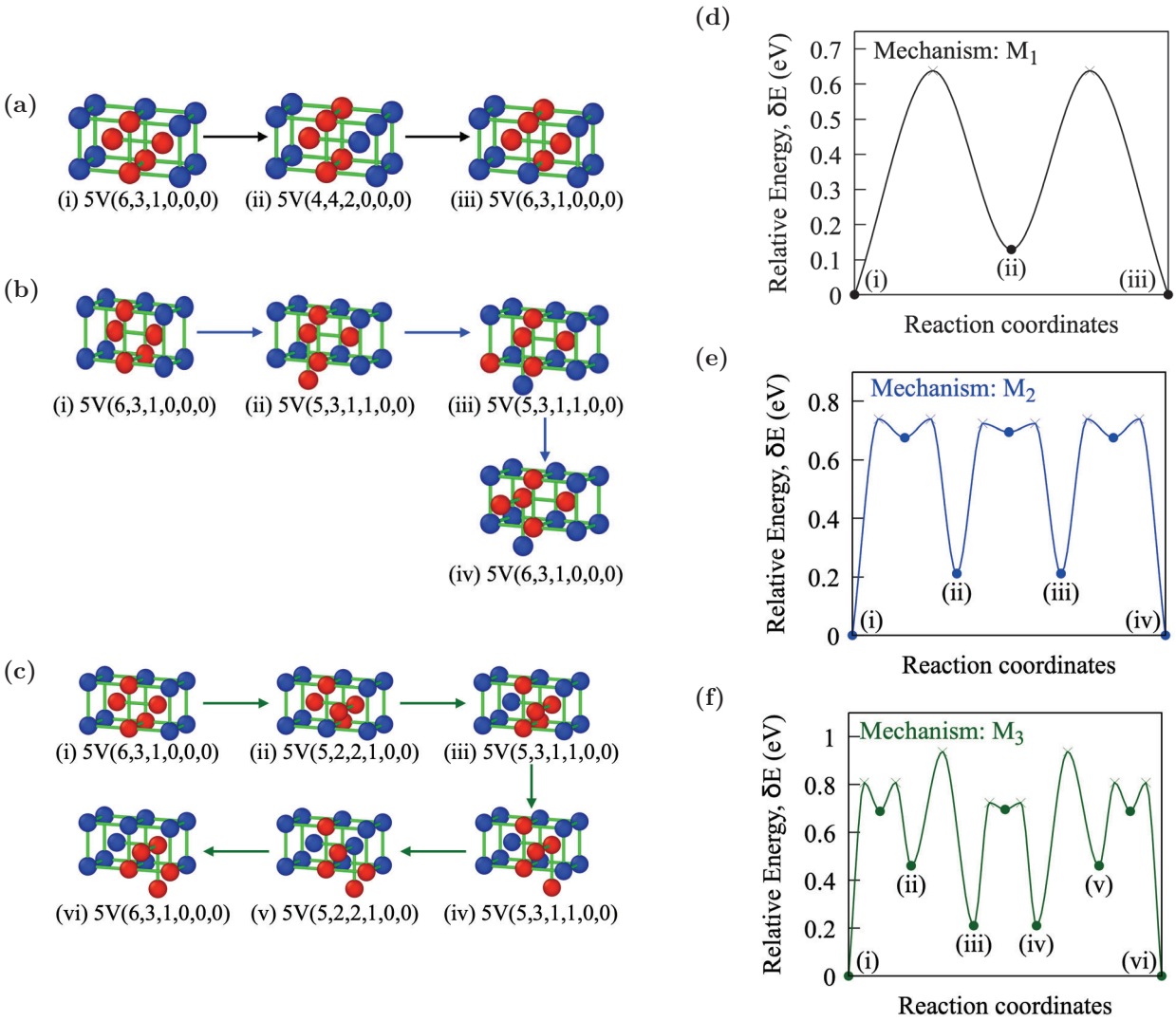

Fig. 5.9. Schematic representations of diffusion pathways — a, b, and c — and corresponding energetic evolution — d, e, and f — for the three most dominant diffusion mechanisms M_1, M_2, and M_3, respectively associated with the five-vacancy cluster in bcc Fe at 600K. In the schematic diagrams, the blue and red spheres represent crystalline Fe atoms and vacancies, respectively. The cross and filled circles on the energetic graphs represent the saddle points and minima, respectively. Indices (I, II, III, etc.) are used to identify states and explain the diffusion mechanism. The bound structures are defined as 5V(a,b,c,d,e,f), where a, b, c, d, e, and f represent the total number of 1NN, 2NN, 3NN, 4NN, 5NN, and 6NN vacancy pair-separation distances, respectively.

respectively. The selected and sampled activation energies as a function of KMC step, as well as the number of events in the catalog per step for events involving vacancy movement, are shown in Fig. B.2. As expected, the LD structure for the five vacancies is quite

unstable and rapidly collapses into a five-vacancy bound complex irrespective of the initial orientation. The ground state (GS), composed of six 1NN, three 2NN, and one 3NN vacancy pair-separation distance, is reached in about 2.3 μs (1519 KMC steps), 1.8 μs (1935 KMC steps), and 3.1 μs (1789 KMC steps) for $LD_{[100]}$, $LD_{[110]}$, and $LD_{[111]}$, respectively. Therefore, the initial $LD_{[100]}$, $LD_{[110]}$, and $LD_{[111]}$ structures are 0.78, 1.83, and 1.16 eV, respectively, above the GS. Going back to the initial LD structure, the system would need to cross significant effective barriers of 2.13, 2.44, and 1.75 eV, respectively, as measured from the ground state. The collapse of all three LD structures occurs in the same manner, triggered by one atom entering at the corner of the LD structure, requiring an activation barrier of 0.630, 0.607, and 0.595 eV for LD^5_{100}, LD^5_{110}, and LD^5_{111} respectively. The first few steps of the collapse for each of the three LD structures are shown in Appendix B Fig.B.3.

Once vacancies reach the ground state, ten configurations dominate the dynamics of the system, representing more than 90 % of all accepted configurations. Table 5.4 summarizes the energy landscape for the ten most stable penta-vacancy bound compounds, providing information regarding formation and transition energies for these states. Fig.5.9 represents the three most dominant diffusion mechanisms denoted as M_1, M_2, and M_3 for this complex. Mechanism M_1 is completed going through one intermediate state. From the ground state, the system moves to a bound state (0.129 eV above the GS), with a composition of four 1NN, four 2NN, and two 3NN vacancy pair-separation distances by crossing an activation barrier of 0.638 eV, followed up with a transition of 0.509 eV system move to the new GS to complete the migration. Mechanism M_2 is symmetrical and visits two intermediate bound configurations. From the ground state, the system moves to the bound state (0.211 eV above the GS), which has a composition of five 1NN, three 2NN, one 3NN, and one 4NN vacancy pair-separation distances, crossing a 0.740-eV, then a 0.513 eV barrier, to bring the system into a new intermediate bound state with the same structure. Finally, the system reaches a translated GS by crossing a 0.528 eV barrier. Like M_2, mechanism M_3 is also symmetrical and is completed through four intermediate bound states having an overall migration barrier of 0.937 eV.

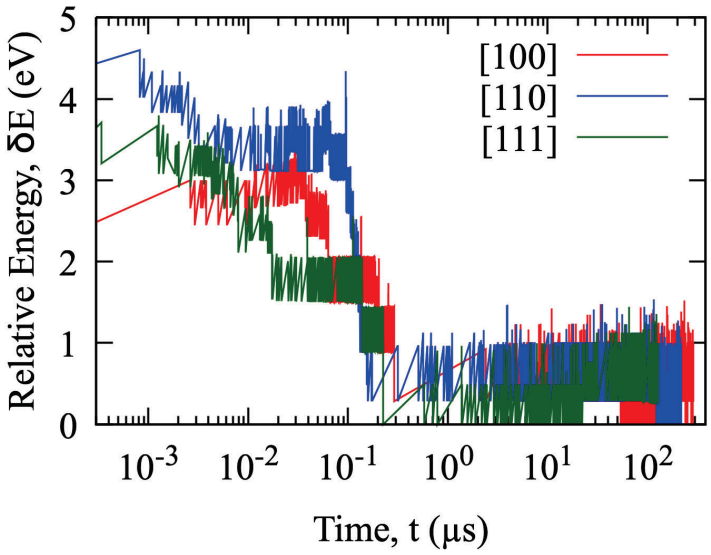

Fig. 5.10. Energy evolution of eight vacancies as a function of time at 600K: red, blue, and green lines for the initial line dislocation structures along [100], [110], and [111], respectively.

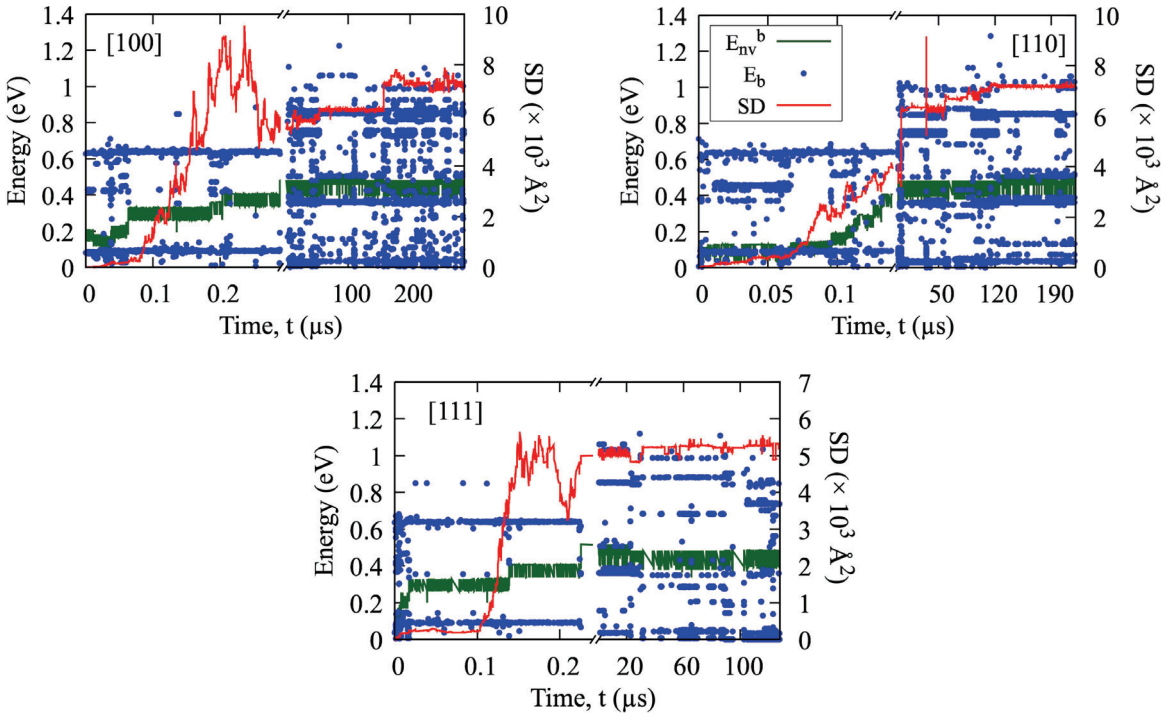

Fig. 5.11. Activation-energy (left, blue symbols), binding energy at the local minima (left, green line) and squared displacement (right, redline) as a function of time for the line dislocation of eight vacancies along [100] (top left), [110] (top right), and [111] (bottom center) direction in a bcc Fe at 600K.

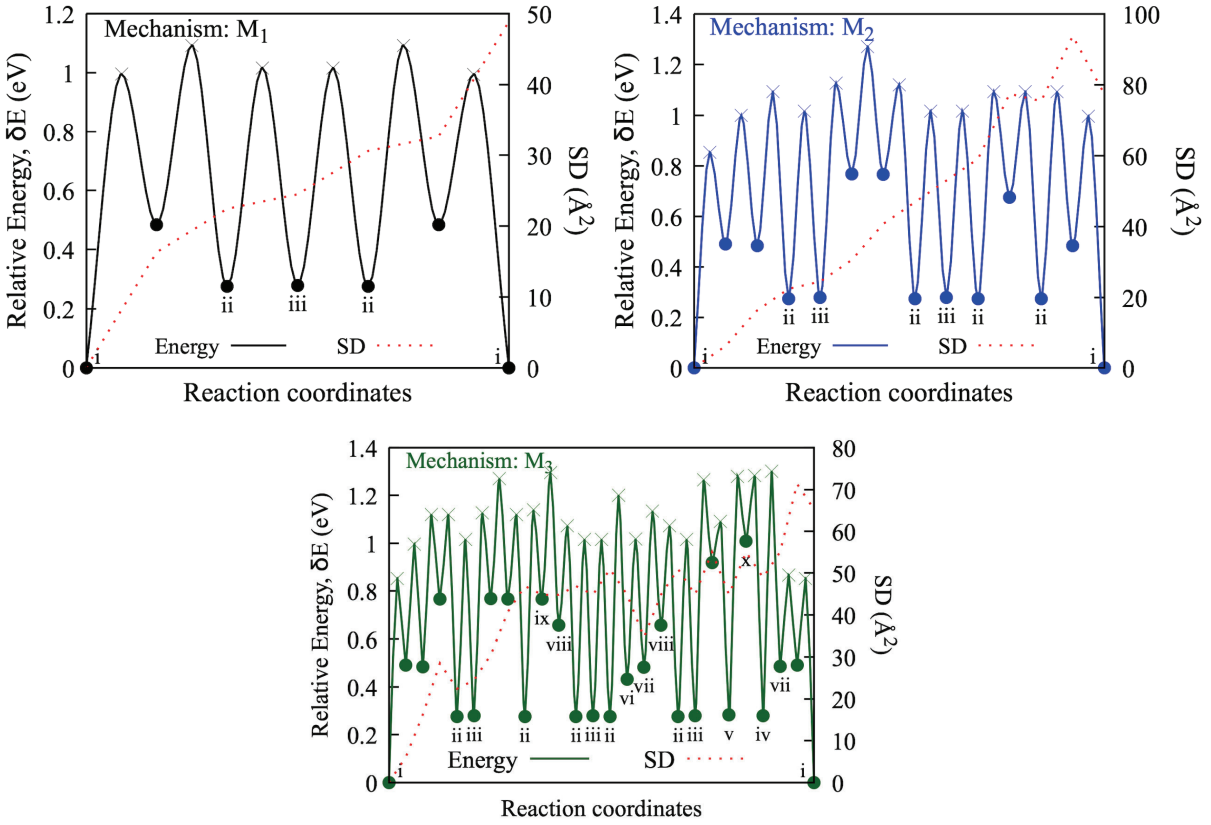

Fig. 5.12. Energy barriers and square displacement for the diffusion mechanism (ground state to ground state) of 8-vacancy cluster. Numeric numbers (i to x) represent the bound states, where (i) 8V(12,8,4,4,0,0), (ii) 8V(12,7,5,3,1,0), (iii) 8V(12,7,5,4,0,0), (iv) 8V(12,7,4,4,1,0), (v) 8V(12,7,4,4,0,1), (vi) 8V(10,8,6,2,2,0), (vii) 8V(11,7,5,4,1,0), (viii) 8V(10,7,4,6,0,1), (ix) 8V(11,6,4,5,1,1), and (x) 8V(10,6,4,5,2,1).

5.6.5. 8-vacancy cluster

To see how the collapse of the line dislocation (LD) structure occurs as the LD size increases, we analyze the LD structure containing eight vacancies along [100], [110], and [111] directions. These systems are run for 7000 KMC steps representing 280 μs, 250 μs, and 122 μs of simulation time for $LD_{[100]}$, $LD_{[110]}$, and $LD_{[1111]}$, respectively at 600K. At the end of the simulations, around 6202, 7331, and 6347 topologies have been analyzed for new events for $LD_{[100]}$, $LD_{[110]}$, and $LD_{[1111]}$, respectively. Among these, the number of unique topologies visited, i.e., selected during the kinetics, for $LD^5_{[100]}$, $LD^5_{[110]}$ and $LD^5_{[111]}$, are 298, 332, and 253, respectively. Fig.5.10 plots the energy evolution and Fig.5.11 the detailed activation energy, binding energy at the local minima, and squared displacement as a function of time

at 600 K. The selected and sampled activation energies as a function of the KMC step, as well as the number of events in the catalog per step for events involving vacancy movement, are shown in appendix B, Fig.B.4. As for the 5-vacancy LDs, the structures collapse into an eight-vacancy bound compact complex, but over a time scale 2 to 10 times longer: the ground state (GS) is reached in about 53.9 μs (2566 KMC steps), 112.8 μs (5132 KMC steps), and 0.2 μs (663 KMC steps) for $LD_{[100]}$, $LD_{[110]}$, and $LD_{[111]}$, respectively. This is accompanied by a relaxation of 2.45, 4.25, and 3.12 eV, respectively, from the initial $LD_{[100]}$, $LD_{[110]}$, and $LD_{[1111]}$ structures. Going back to the initial LD structure, the system must cross significant effective barriers of 3.69, 5.02, and 3.85 eV, respectively, as measured from the ground state.

The ground state of the eight vacancy cluster has a combination of twelve 1NN, eight 2NN, four 3NN, and four 4NN vacancy pair-separation distances. This cluster is characterized by a binding energy of 4.139 eV (0.517 eV per vacancy). While a large number of states are accessed during the simulation, three actual diffusion events take place after the bound complex is formed. Including various oscillations, mechanism M_1 takes place over 74 KMC steps over 1 μs, mechanism M_2 takes place over 376 KMC steps over 4.9 μs, and mechanism M_3 takes place over 423 KMC steps over 21.5 μs. Reducing the process to its essential steps, the diffusion mechanisms M_1, M_2, and M_3 for the eight-vacancy cluster can be reduced to 6, 13, and 25 jumps, respectively, as shown in Fig.5.12. For the mechanisms, M_1, M_2, and M_3, the migration energy over pathways connecting ground states, is 1.093, 1.271, and 1.30 eV, respectively, with M_1 being the most probable diffusion mechanism at 600 K.

5.6.6. Lifetime and diffusion coefficients of vacancy-cluster

The average thermal lifetime and diffusion coefficient for the various clusters are listed in Table 5.5. Both the two- and three-vacancy clusters show a diffusion coefficient of the same order of magnitude as a single vacancy at 4.7×10^8 Å$^2 s^{-1}$, and 4.7×10^8 Å$^2 s^{-1}$ respectively. The average thermal lifetime for the two- and three-vacancy clusters is 0.036 μs and 0.2 μs respectively. The bound two- and three-vacancy cluster compounds diffuse for 24 and 224

Table 5.5. Average cluster lifetimes and diffusion coefficients for different vacancies at 600 K

Cluster	Average thermal lifetime (s)	Diffusion coefficient ($Å^2\ s^{-1}$)
1V	-	7.17×10^8
2V	$(3.6 \pm 0.01) \times 10^{-8}$	$(4.7 \pm 0.01) \times 10^8$
3V	$(2.0 \pm 0.01) \times 10^{-7}$	$(2.2 \pm 0.01) \times 10^8$
4V	$(3.0 \pm 0.01) \times 10^{-6}$	$(1.1 \pm 0.02) \times 10^7$
5V	$(1.3 \pm 0.01) \times 10^{-5}$	$(9.0 \pm 0.04) \times 10^5$
8V	-	1.8×10^4

steps on average before dissociating. By further increasing the number of vacancies in the cluster (four and five vacancy clusters), the diffusion coefficient is considerably decreased. The diffusion coefficient of four- and five-vacancy clusters are one and three orders of magnitude lower than that of a single vacancy: 1.1×10^7 $Å^2 s^{-1}$ and 9×10^5 $Å^2 s^{-1}$ respectively. Their lifetime at 600 K is 3 μs and 13 μs. In terms of steps, the bound four and five vacancy cluster compound diffuse for 122 and 145 steps on average before dissociating. Even a cluster of eight vacancies can be mobile with a diffusion coefficient of 1.8×10^4 $Å^2 s^{-1}$ associated with a relatively high migration energy (> 1 eV).

5.7. Discussion

The kinetics of vacancies play an essential role in determining the properties of a material. Understanding the aggregation and diffusion mechanisms of vacancies is, therefore, a crucial step in further exploring the mechanical/electrical properties of structural materials associated with the formation of vacancies by deformation or radiation [6, 33, 53, 72, 86]. However, experimental approaches are generally unable to provide the required detailed microscopic information that would allow us to fully understand this role. Direct calculations can compensate for experimental limitations in the case of simple point defects, but the rapidly increasing complexity of the energy landscape of even small clusters requires automated search tools such as the kinetic activation-relaxation technique (kART).

Accessing large time scale and system sizes, kART simulations presented here provide a detailed characterization of vacancy aggregation and clustering diffusion processes and the associated energy landscapes, showing a relatively complex picture even for the simplest systems. This picture is well characterized with kART, since the catalog is updated and expanded at every step as new topologies are explored.

We analyze the energy landscape associated with bcc crystalline Fe containing one to eight vacancies. The more complete energy landscape generated here and obtained with simulations that reached several hundred microseconds allows us to identify new mechanisms. Comparison with previously published works [46, 95] for the monovacancy diffusion, using EAM force fields, confirms that the correct basic diffusion mechanisms are recovered for this system. For small vacancy cluster diffusion with two to four defects, the mechanisms predicted and diffusivity trends match those seen in the literature [36, 37, 46, 69]. For di-vacancy, a global minimum energy with a V–V distance separation of the second nearest neighbor (2NN) is found, in agreement with previous MD and DFT studies. The mechanism of migration of the di-vacancy in iron consists of an oscillation not only between 2NN and 1NN states but also, largely, between 2NN and 4NN states, even though the 1NN state is strongly bound compared to the 4NN state. These thermodynamically counter-intuitive diffusion mechanisms of di-vacancy could easily be misidentified when using simpler approaches, e.g., the nudged elastic band method (NEBM). Although these mechanisms have been captured with traditional KMC and careful analysis of DFT results [37], here they arise naturally without any special consideration or bias. For tri-vacancy cluster, the migration energy of the dominant diffusion mechanism is 0.64 eV, very close to the diffusion barrier for mono-vacancy. Previously, using DFT-NEBM, Fu *et al.* [46] obtained an activation energy of 0.35 eV lower than the value that we find here; however, the general mechanism matches the one presented here. However, D. Kandaskalov et al. [69] repeated the DFT study and reported results of two types of numerical simulations: in the first simulation, the Fe atom is fixed between the two nearest vacancies, and in the second simulation, it is placed in the center of a four-vacancy. In the first case, the mechanism obtained, with a 0.64-eV barrier,

matches the mechanism found here while the second simulation leads to a 0.36-eV barrier that has not been generated here, even with additional ARTn searches.

Looking at the tetra-vacancy, we find that the dominant mechanism has a 0.703-eV barrier, a little higher than the values found in previous DFT calculations [46, 69]. This could be due to image interactions introduced by the small unit-cell supercell used or to accuracy issues with the EAM potential. A recent DFT work, however, indicates significant finite size effects affecting the height of the calculated energy barriers[25]. Nevertheless, the match in the mechanism pathway is reassuring and indicates the key physics is being captured by the potential. The barrier height we find here agrees with the previous literature value using different empirical potentials[36]. Furthermore, during simulation, we find that degenerate or quasi-degenerate saddle points are not so rare. These states play an important role in cluster diffusion. Even though larger vacancy clusters are less mobile, they can still move, and we identified diffusion mechanisms for 5- and 8-vacancy clusters. A number of diffusion mechanisms for vacancy clusters with barriers higher than 1 eV are also identified with kART. Since these are much rarer, however, we did not discuss them here in detail, but the presence of strain, defects, or other impurities could lower the barrier and make them relevant.

Methods such as kART, which includes both elastic and kinetic effects, greatly facilitate this characterization as compared to standard approaches where these pathways must be deduced one by one, an approach that rapidly becomes impossible when dealing with long-range elastic effects or complex systems.

5.8. Conclusion

Using the kinetic activation-relaxation technique (kART) coupled with an embedded-atom method (EAM) potential, we study the vacancy aggregation and clustering diffusion processes in α-Fe. Our results show a richness in the diffusion mechanisms as well as a complex balance between elastic and chemical effects. By reaching physically-relevant timescales without presuppositions regarding mechanisms and elastic effects, this approach provides a

detailed and reliable representation of the migration pathways of vacancy clusters, including rare pathways that are orders of magnitude less likely to occur in pure Fe than the dominant ones.

We find that the diffusion barriers of vacancies do not change monotonically with cluster size. Moreover, the number of possible barriers is much larger than previously identified. Even focusing on the barriers relevant at 600 K, we find considerable complexity that prevents the use of simplistic diffusion models. Degenerate or quasi-degenerate saddle points, for example, are much more common than generally thought. As discussed, these states play a significant role in cluster diffusion. As for the diffusion coefficient, we find that divacancies and trivacancies diffuse on the same order of magnitude as monovacancies. The stabilization of vacancy clusters is achieved both by energetics, with larger vacancy clusters having lower energy, and by kinetics: the thermal lifetime of vacancy clusters increases with cluster size. Yes, these larger clusters are less likely to interact with each other, as their diffusion coefficient decreases significantly with size.

Overall, these results provide a much deeper understanding of the microscopic and kinetic picture of vacancy clusters in $\alpha-$Fe; a qualitative understanding that should be valid for all bcc metals. The complex energetic environment controlling the kinetics of small vacancy clusters presented here demonstrates that simple rules are not sufficient to develop a robust approach to predictive control and prevention of damage processes associated with vacancy clusters in structural metals. More work is needed to better characterize this behavior and derive general rules. It is clear that additional simulations are needed to capture the energy landscape of vacancy cluster diffusion in other materials or the presence of strains, defects, or impurities; simulations to this end are underway.

In summary, if the use of empirical potential limits the general application to defect kinetics, the agreement with DFT calculations for some of the simpler mechanisms suggests that the main results presented here are physically relevant. On a qualitative level, these show that even in systems as simple as the one presented here, complex diffusion mechanisms can be important. Recovering dominant diffusion, but also trapping mechanisms (for instance,

the transition between 2NN state to 1NN state for di-vacancy cluster), requires much more than the simple identification of a few configurations by symmetry analysis or through molecular dynamics, as the latter cannot deliver a detailed characterization for temperatures well below melting mainly because some of the transformations require dwelling metastable states that cannot endure in these high temperatures and can only play a dynamical and structural role at a lower temperature.

Accelerated methods such as the kinetic ART provides detailed and rich information regarding mechanisms that we did not know existed until now. The systematic use of such methods will continue to enrich significantly our understanding of diffusion at the atomistic level in materials.

5.9. Supplementary materials

see appendix B

5.10. Access to codes

The most recent packages for kART and ARTn are available freely upon request. Please contact Normand Mousseau (normand.mousseau@umontreal.ca).

5.11. Acknowledgment

This work has been supported by the Qatar National Research Fund (QNRF) through the National Priorities Research Program and the Canada Research Chairs program and by a discovery grant (NM) from the Natural Sciences and Engineering Research Council of Canada (NSERC). We are grateful to Calcul Québec/Compute Canada (CQ/CC) for generous allocations of computer resources.

Chapter 6

A local basin approach to the kinetic activation-relaxation technique

6.1. Objective

The goal of this article is to find a way to deal more efficiently with systems in which multiple independent oscillators dominate the kinetics of the system. We propose a local basin approach for dealing with these oscillating basins in kART, which is discussed in detail in this article.

Authors in order: Md Mijanur Rahman and Normand Mousseau

Status : In preparation.

Author contributions:

- Normand Mousseau (NM) and Md Mijanur Rahman (MMR) conceived the project.
- MMR performs the implementation.
- MMR wrote the first version of the article.
- MMR and NM contributed to the writing of the article.
- NM supervised all this work.

6.2. Résumé

Les simulations cinétiques de Monte Carlo peuvent devenir inefficaces en présence de barrières à faible énergie qui dominent la cinétique, car chaque étape est associée à une très petite augmentation du temps de la simulation. Dans certains cas, ces événements sont des oscillateurs, un ensemble d'états séparés par des barrières de basse énergie au fond d'un bassin énergétique et qui ne contribuent pas à l'évolution du système. Nous proposons un algorithme pour détecter, à la volée, des groupes d'états oscillants et les consolider en bassins locaux, que nous traitons avec la méthode d'auto-construction de bassins (bac-MRM), une approche de type équation-maître basée sur la méthode du taux moyen. Le bac-MRM calcule une solution analytique statistiquement exacte des oscillateurs reliés en bassin local (définit par proximité spatiale) et de leur taux d'échappement au fur et à mesure que le paysage énergétique est exploré le long de trajectoires spécifiques. Dans cet article, nous discutons en détail de la mise en œuvre des simulations de la technique de relaxation de l'activation cinétique du bassin local qui contiennent simultanément des bassins locaux et des événements hors bassin.

6.3. Abstract

KMC simulations can become inefficient in the presence of low-energy barriers that dominate the kinetics, as each step is associated with a very small clock increase. In some cases, these events are flickers, a set of states separated by low-energy barriers deep in an energy basin that does not contribute to the evolution of the system. We propose an algorithm to detect, on-the-fly, groups of flickering states and to consolidate them into local basins which we treat with the basin-auto-constructing Mean Rate Method (bac-MRM), a master equation-like approach based on the mean-rate method. The bac-MRM computes a statistically exact analytic solution of the locally connected flickering states (as defined by their spatial proximity) and their escape rate as the energy landscape is explored, at the cost of specific trajectories. In this article, we discuss in detail the implementation of the local basin

kinetic activation relaxation technique simulations that contain local basins and non-basin events simultaneously.

6.4. Introduction

The microstructural evolution of metals and alloys is still a major challenge. In many systems, microstructural evolution is governed by a series of rare events that often have large activation barriers and occur on time scales that are simply beyond the reach of standard atomistic simulation techniques such as the molecular dynamics (MD) method [3] . Therefore, the kinetic Monte Carlo (KMC) method [142, 146] is often the method of choice when time scales of milliseconds to hours need to be reached. Rather than studying the vibrational motion of atoms, as is done in MD, the KMC method can achieve long time scales by determining a sequence of state-to-state jumps. These state-to-state jumps of the system form what is called a Markov chain. In a standard KMC implementation, a catalog of process rates with their rates is provided at the beginning. Then, in each KMC step, an atomic process with probability proportional to its rate is randomly selected from the catalog, time is updated, the system transitions to a new state, and the list of possible transitions for the system's new state is updated. If the basic assumptions of KMC are satisfied, namely that the first exit time is exponentially distributed, the statistics obtained from the KMC simulation of rare events can be as accurate as the statistics from MD.

Despite the higher computational efficiency of KMC, challenges remain in dealing with the small barrier problem. In KMC, the dynamics is dominated by the lowest barrier energy of a system. When the energy landscape consists of basins with numerous states connected by very low energy barriers compared to the barriers required to leave those basins, the algorithm is trapped into computing non-diffusive events, which significantly reduces its efficiency in two ways. First, it limits the achievable simulation time, since the low energy internal barriers produce a high total sum of rates and thus a short average KMC time increment. Second, computational resources are bound to exploring the states within a

basin without providing much information since effective diffusion usually occurs outside the energy basins.

With respect to the low barrier problem, we implement a local basin approach for kART, an off-grid kinetic Monte Carlo algorithm with flying catalog structure. Flickering basins are widely spaced and spatially and geometrically protected, they are treated as single events and limit the information loss between events. The internal kinetics of the basin are solved analytically using the Accelerated Basin Method (bacMRM) [13, 112]. The transition rates that allow the basin to exit are corrected by considering the correlations between the states of the basin. In this way, when an accepted event occurs in a part of the system, only the basins that are physically close to the affected region are destroyed, while the others remain in the catalog. Since relevant barriers are reconstructed at each KMC step, the introduction of local basins will not change the overall kinetics of the simulation as long as the interaction between these basins is small enough not to change the basin states and their event list. This article is organized as follows: After a brief overview of kART in section 6.5, the local basin algorithm is presented in section 6.6. Finally, a conclusion is drawn in section 6.7.

6.5. Standard kART algorithm

The standard kART [13, 40, 103] algorithm starts from an initial configuration relaxed into a local energy minimum. The local environment of each atom is characterised by its local topology, which is evaluated using NAUTY [97], a topological analysis library developed by McKay. To do this, all atoms within a sphere of predefined radius (which depends on the system under study but is typically chosen to be between 5 and 7 Å, a region encompassing between 40 and 80 atoms) surrounding an atom are selected as vertices of a graph. Edges are drawn between atoms that have fewer than one first neighbour. The automorphic group of the resulting graph is then computed, providing a unique identifier and sufficient information to recover permutations and symmetry operations between two automorphic configurations. All atoms sharing a given topology are assumed to be associated with the same list of events.

This hypothesis can be tested in the event reconstruction phase. If it fails, new cut-offs are introduced to ensure a clear correspondence between topology and geometry.

For each topology, a search for activated pathways is started using ART nouveau [7, 88, 92], an efficient algorithm for finding open-ended transition states. Each event is classified by initial minimum, saddle configuration, and final state topologies and stored in the catalogue.

Once the event catalogue is updated, the generic events are ordered depending on their rate, which is calculated as follows:

$$r_i = \nu_0 e^{-\frac{E_b}{k_B T}} \tag{6.5.1}$$

where ν_0, a prefactor that determines the attempt frequency, and E_b is the activation energy for the event i defined as the energy difference between the transition state and the initial minimum [42, 43, 78]. In the kinetic ART code, ν_0 can be computed for each event within the harmonic approximation or given a constant value (generally 10^{13} Hz).

Events within a given fraction (we generally use 99.99%) of the total ascending cumulative rate are fully reconstructed and reconverged into specific events to ensure that elastic and configurational effects are exactly taken into consideration. At this point, following Bortz et al. [17], the elapsed time to the next event is computed as:

$$\Delta t = -\frac{ln\mu}{\sum_i r_i} \tag{6.5.2}$$

where μ is a random number in the [0,1[interval and r_i is the rate associated with event i. The clock is pushed forward, an event is selected with the proper weight, and the atoms are moved accordingly after a geometrical reconstruction.

Once in this new configuration, the process starts again: the topology of all atoms belonging to the local environment of the new state is constructed; if an unknown topology is found, a series of ART nouveau searches is started; otherwise, the process proceeds to the next step. After all events have been updated, the low-lying barriers are relaxed again before the KMC algorithm is applied. These steps are repeated many times to simulate the evolution of the system.

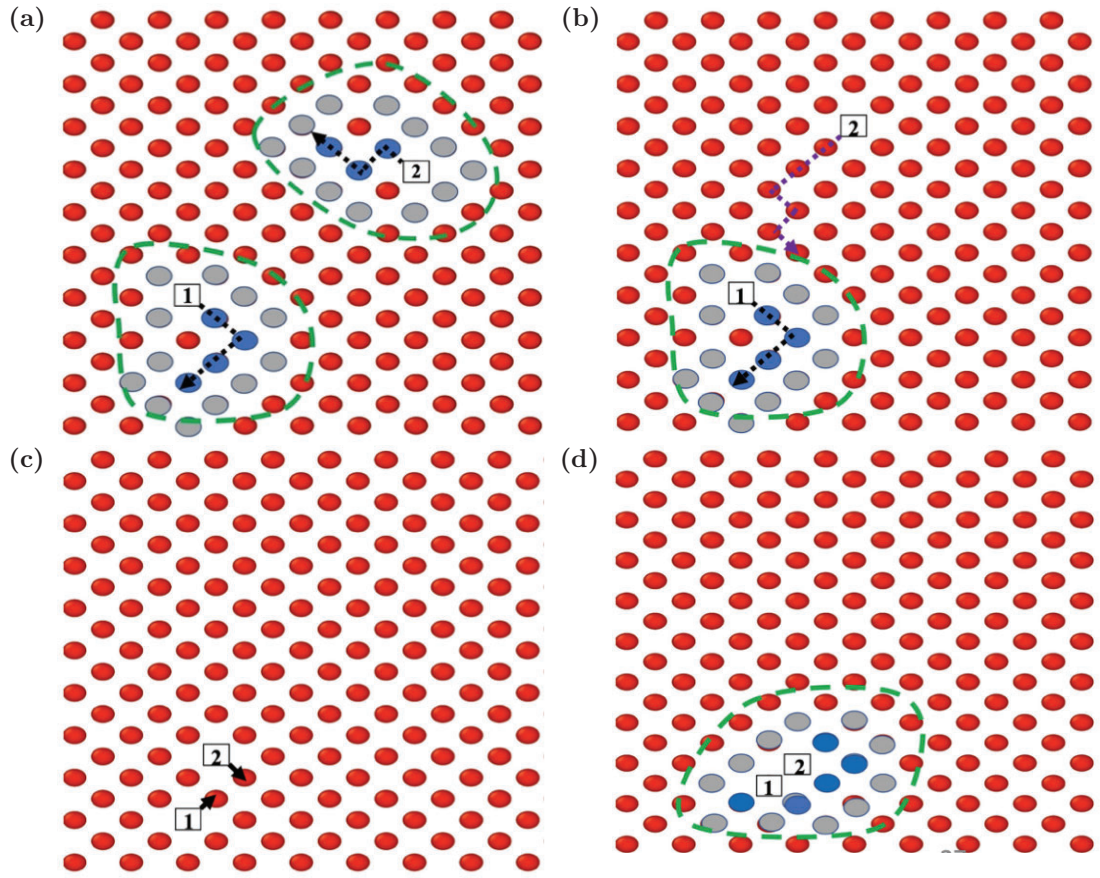

Fig. 6.1. Schematic representation of the local basin approach for two vacancies evolving on a square lattice: vacancies V_1 and V_2, represented by the two labelled squares, are initially trapped. The basin events are represented by the black dotted arrows. The blue and grey circles represent the locations within the basin and the exit locations, respectively. The green dashed line represents the active zone of the basin. The sequence of events is as follows: (a) the two vacancies are spatially protected, the mean residence time t_1 and t_2 are plotted (here $t_2 < t_1$), (b) V_2 exits the basin, diffuses and collides with the spatial protection of V_1, non-basin events are indicated by a violet dotted arrow, (c) V_2 attaches to V_1, and (d) a diffusing entity of two vacancies.

6.6. Local basin algorithm

The schematic representation of the approach of the local basin for two vacancies evolving on a square lattice is shown in Fig.6.1. Let us consider that the vacancies V_1 and V_2 are initially trapped in flickering basins that are geometrically far apart. These flickering basins are treated as single events and limit the information loss between events. kART uses the basin-auto constructing mean rate method (bacMRM) to determine the mean dwell time for the states within the basin. A basin with such states is constructed on-the-fly using a

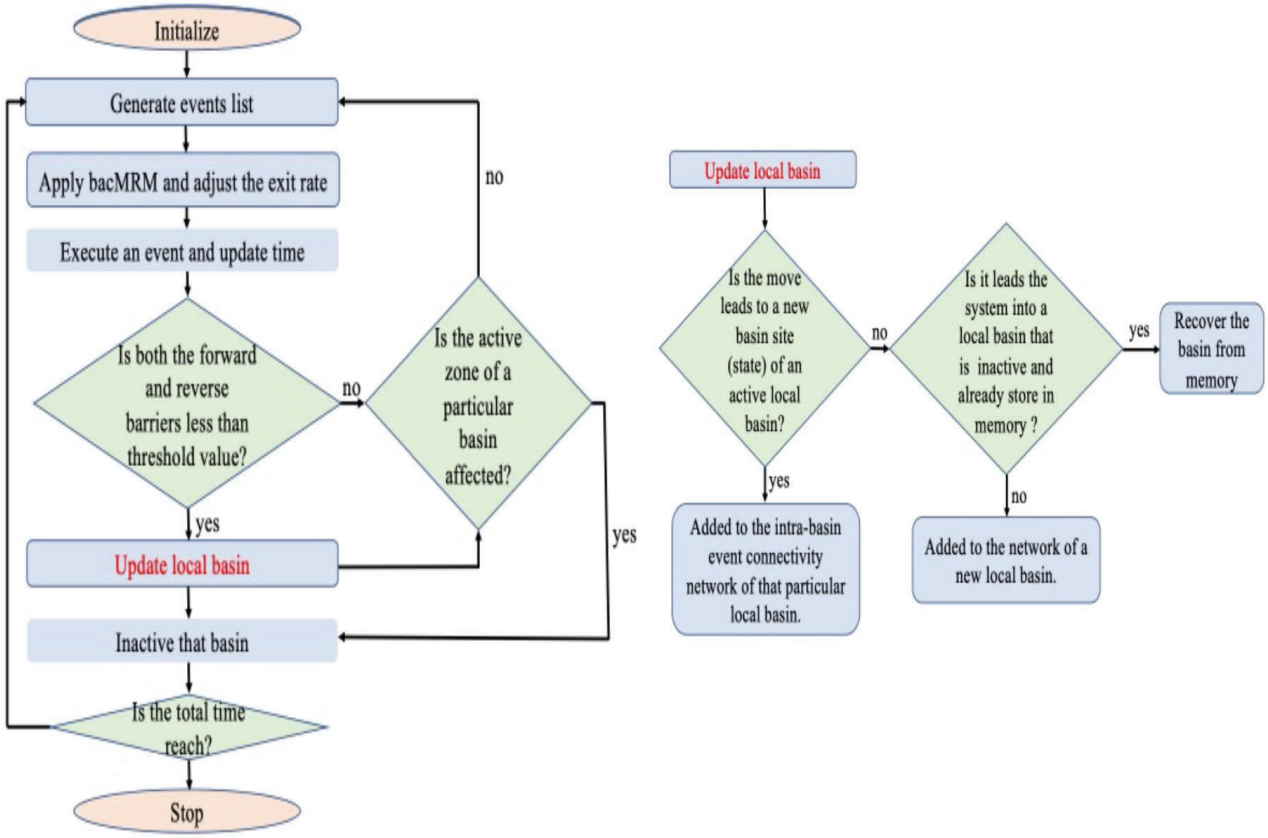

Fig. 6.2. Flowchart of local basin algorithm.

predetermined barrier cutoff value. Intra-basin states within the basin are visited only once, and the exit time associated with the exit-basin transitions is adjusted using the bacMRM procedure. In this way, when an exit-basin event takes place in one part of the system, only the basins that are physically close to the affected region are destroyed, while the others remain in the catalog. A workflow of the local basin algorithm is illustrated in **??**. The basic algorithm of the local basin approach is defined as follows:

(1) Perform a standard kART move by executing an event and advance time;

(2) Check the execute event:

(i) if the selected event is an intra-basin event: (a) if it leads to a new basin site (state) of an active local basin, then it is added to the intra-basin event connectivity network of that particular local basin and removed from the KMC tree of available events; or (b) if it leads to an already explored basin site (state) of an active local basin,

it is rejected, removed from the tree, and added to intra-basin event connectivity network, adjusting the rates as needed; or (c) if it leads the system into a local basin that is already store in memory, in that case, we use basin reconstruction algorithm (see below) to rebuild the complete basin; otherwise, (d) it will be considered as the first basin event, removed from the tree, and added to the network of a new local basin. Events associated with all atoms within the topo cut-off radius around the previous intra-basin site are considered exit-basin events and kept in the tree and could be picked as KMC move. Events associated with all atoms within the topo cut-off radius around the current intra-basin site will be marked as exit-basin events after the current configuration has been searched. Finally, The list of atoms in the basin-active-zone of that particular local basin is updated as S_t=$S_1 \cup S_2 \cup ... \cup S_n$ where S_t is the list of atoms in the basin-active-zone, n is the total number of intra-basin sites present in that local basin, and S_1, S_2, and S_n are the set of atoms within the topo cut-off radius around the first, second, and nth intra-basin site, respectively (see Fig. 6.2);

(ii) if the selected event is an exit-basin event of a local basin, we inactivate that local basin and all exit-basin events related to that local basin are removed from the KMC tree;

(iii) if the selected event is a non-basin event, in which case a standard kART move is applied;

(3) Check if this move affects the basin-active-zone (i.e., changes the topology/local environment of any atom inside the basin-active-zone) of any active local basin; we destroy that particular local basin.

(4) Generate all possible events for the current configuration.

(5) Apply the bac-MRM to all individual active local basins to modify the rate of the exit-basin transitions following Eq.6.6.5, and the total rate is adjusted accordingly.

(6) Return to step (1).

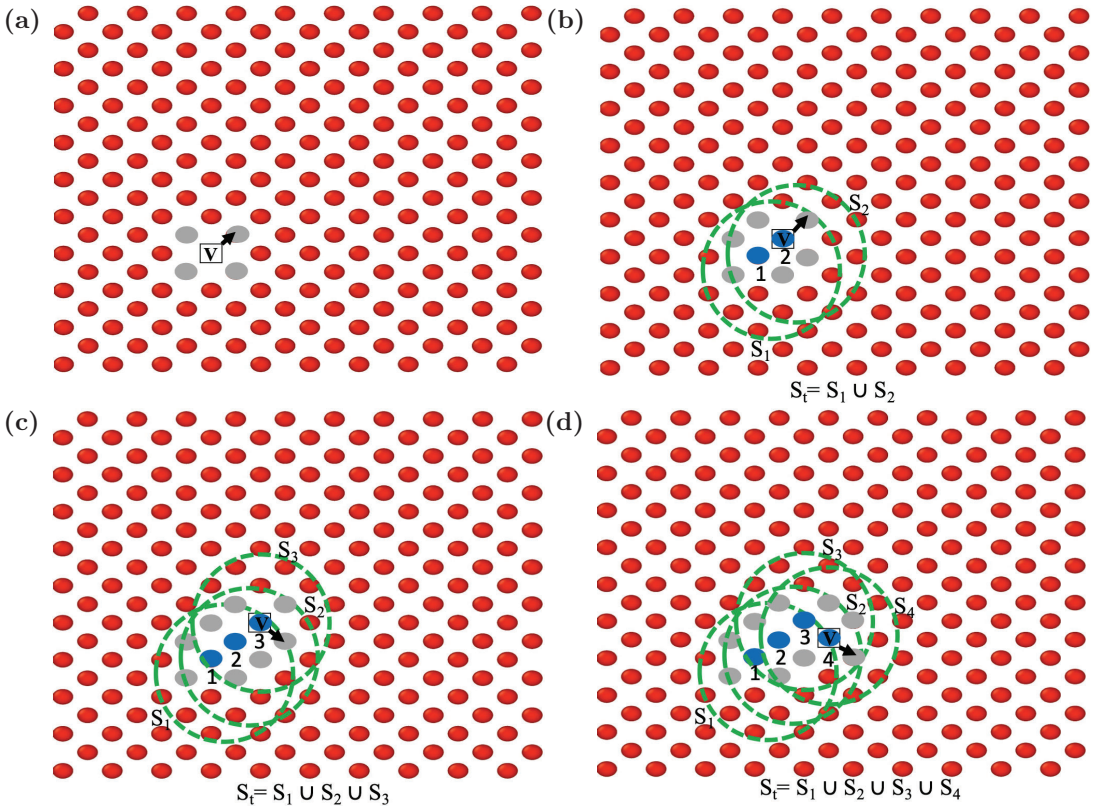

Fig. 6.3. Diagram illustrating the making of the basin-active-zone of a local basin containing four intra-basin states. Where S_t is the list of atoms in the basin-active-zone; S_1, S_2, S_3, and S_4 are the set of atoms within the topo cut-off radius around the first, second, third, and fourth intra-basin site respectively. blue and gray circles represent the intra-basin sites and basin-exit sites, respectively.

6.6.1. Basin reconstruction algorithm

The basin reconstruction algorithm allows us to recover all the intra-basin and exit-basin states and their connectivity. For example, suppose an executed event is a low-energy barrier event that leads the system to fall again into a visited local basin. Then, the executed event is added to the intra-basin event connectivity network (i.e., for the first intra-basin event, this is, at that time, the only event) and removed from the KMC tree. Currently, there are two intra-basin sites in the list of intra-basin sites. Our basin reconstruction algorithm starts from here. A workflow of the basin reconstruction algorithm is shown in **??**. The algorithm is as follows:

(1) Pick the first intra-basin site i=1 from the list of intra-basin sites;

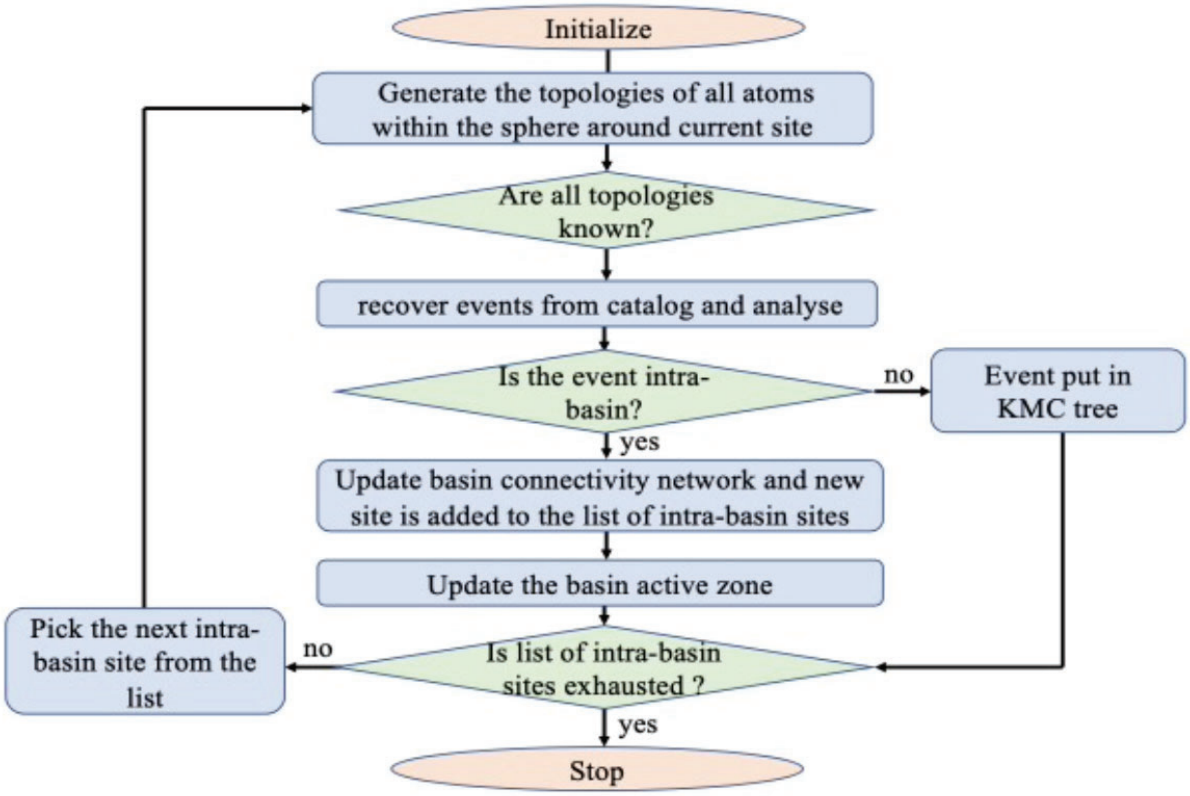

Fig. 6.4. Flowchart of the basin reconstruction algorithm.

(2) Generate the topology of all atoms within the topo cut-off radius around the site i;

(3) Check all the topologies: if all the topologies are known, recover associated events from the catalog and go to step 4. Otherwise, pick the next intra-basin site j $\rightarrow$ i from the list of intra-basin sites and return to step 2;

(4) Check all events:

(i) if an event is an intra-basin event (both forward and reverse barriers are lower than a predefined threshold value), it is added to the intra-basin event connectivity network, and if it leads to a new intra-basin site, the new site is added to the list of intra-basin sites; otherwise, (ii) it will be considered an exit-basin event and will be added to the KMC tree.

(5) Update the list of atoms in the basin-active-zone;

(6) Pick the next intra-basin site j $\rightarrow$ i from the list of intra-basin sites and return to step 2;

(7) Repeat step 2 to 6 until the list of intra-basin sites is exhausted.

6.6.2. The Mean Rate Method

Following Puchala et al. [112], a local basin is separated into intra-basin and exit-basin states. To determine the mean time per escape spent in each intra-basin state i, we need to create the transition probability matrix T with components,

$$T_{ij} = \frac{r_{ij}}{\sum_k r_{ik}} = \tau_i^1 r_{ij} \tag{6.6.1}$$

where r_{ij} is the rate going from intra-basin state i to intra-basin state j, where k runs over all intra-basin and exit-basin states and $\tau_i^1 = \frac{1}{\sum_k r_{ik}}$, the reciprocal of the sum of all rates leaving state i, is the mean residence time in state i each time it is visited.

As the system moves between states within the basin, the occupation probability for intra-basin states changes. The occupation probability vector of all intra-basin states after in-basin jump m and before jump m+1, $P(m)$ is thus given by repeated application of $\mathbf{T}$ to the initial occupation probability $P_i(0) = \delta_{is}$, where s is the starting state, as:

$$P(m) = \mathbf{T}^m p(0) \tag{6.6.2}$$

Then, all possible jumps (m) from zero to infinity are considered. This is equivalent to the assumption that the system is in equilibrium. The sum of the occupation probabilities over all possible number of jumps gives the average number of times each intra-basin state is visited:

$$P^{tot} = \sum_{m=0}^{\infty} \mathbf{T}^m P(0) = (\mathbf{I} - \mathbf{T})^{-1} P(0) \tag{6.6.3}$$

from which the mean residence time in intra-basin state i before leaving the basin can be calculated:

$$\tau_i = \tau_i^1 P_i^{tot} \tag{6.6.4}$$

These residence times are then used to accelerate the basin exit rates from intra-basin state i to exit-basin state j according to

$$< r_{ij} >= \frac{\tau_i}{\sum_k \tau_k} r_{ij} \tag{6.6.5}$$

with k summing over all intra-basin states.

6.7. Conclusion

In this work, we have presented a local basin method for solving the small-barrier problem arising from groups of recurrent local minima connected by low energy barriers and separated from the overall phase space of the system by high barriers. We have proposed an algorithm to detect, on the fly, groups of recurrent local minima connected by low barriers and consolidate them in a local basin, which we treat with the Markov state model. Finally, we have addressed the integration of this algorithm into standard kART simulations that include local basins and non-basin events. The algorithm presented here provides a general and robust formalism for identifying local basins and dealing with the low-barrier problem that is common in conventional KMC simulations. Implementation of this proposed local basin approach in kART is still in progress. Therefore, there are no supporting results regarding its applications. Once implemented, the algorithm of the approach can be used to study the anisotropic migration of interstitial clusters whose diffusion mechanism is a mixture of fast translations and slow rotations. It could be extended to simulate the dynamics of large objects, such as dislocation loops in solids. The short-time dynamics of these objects consists of transitions confined to a particular energy basin that does not lead to their average motion; only rare transitions corresponding to an exit from the original basin into a similar basin, such as concerted displacements of atoms in a particular direction, contribute to their evolution. Thus, if one were able to solve the dynamics of such objects for a single basin, since this basin simply repeats as the object moves, it could be possible to focus only on the basin-exit transitions that lead to the evolution of the system. In addition, the proposed

approach could also allow efficient calculation of sink strengths relative to defect clusters with mixed mobilities. This is an open- end to this thesis work; we outline other future avenues in perspectives.

Conclusion

Point defects play an important role in materials science. The evolution of materials is governed by the migration of point defects, which affect the physical and mechanical properties of the materials. During the last five years of this thesis, using kART we investigate certain phenomena related to the kinetics of point defects, in particular, the diffusion mechanisms of carbon impurities and vacancy clusters in $\alpha-$iron.

We recall the structure of the thesis and summarize the most relevant results obtained in this work:

Chapters 1-3 are bibliographical chapters devoted to the description of the problem studied (the point defects in materials) as well as the numerical methods to study it. In chapter 1, we briefly described the classification of point defects and their kinetics, as well as reviewed the different experimental and numerical methods to study defect evolution. In chapter 2, we recall the activated processes and transition state theory. We detail the kinetic Monte-Carlo method in its original form; then, we review the developments of this method over the past twenty years. In chapter 3, we described in detail the kinetic ART (kART) method, which is used in our studies.

In chapter 4, we studied the pressure effect on C diffusion in GB of $\alpha-$ iron. We succeeded in drawing a complete picture of the energy landscape, allowing us to provide detailed information on mechanisms and pathways. The effect of pressure can strongly alter the stability and diffusivity of C in GB in a way that depends strongly on the local environment and the nature of the deformation. We find that the segregation energy for a C interstitial tends to become more favorable for GB relative to bulk with increasing isotropic pressure,

with the gain depending on specific sites and changing little for a pressure change of 24 kbar. In addition, we note that the orientation of the pressure with respect to the GB changes the result. If pressure is applied perpendicular to the GB, the available free volume at the GB decreases, and so does the segregation energy, while pressure parallel to the GB plane increases the enthalpy of formation in the bulk, while maintaining a larger free volume and increasing the energy gain due to movement toward the GB. Pressure can also affect the different transition states differently, as shown by our detailed analysis of its effects on the three dominant transition states at the GB. While all three barriers increase linearly with increasing isotropic and normal pressure, albeit with different slopes, this is not the case for pressure applied parallel to the GB plane, which could lead to a change in the dominant diffusion mechanisms and overall diffusion if the pressure is high enough. These observations are important for understanding the evolution of heterogeneous materials, where local variations in pressure can alter carbon diffusion in the material.

In chapter 5, we investigated the stability and diffusion mechanism of vacancy clusters with one to eight vacancies in $\alpha-$iron. The binding energy of vacancy clusters generally increases with vacancy size, indicating a preference for further cluster growth. Moreover, the binding energies for the tetrahedral and octahedral clusters are higher and exhibit larger energy gradients. In contrast, the binding energies of the linear and planar clusters are lower and exhibit smaller gradients. This is expected since the tetrahedral and octahedral clusters with a lower surface-to-volume ratio should be more stable and exhibit a higher growth tendency. The diffusion of vacancies in $\alpha-$iron is a much broader and more complex phenomenon than originally thought. Using the kART method, we identified subtle mechanisms as well as rare and unexpected mechanisms, such as counterintuitive diffusion mechanisms of the di-vacancy cluster, which could easily be misidentified using simpler methods. We also found that vacancy clusters have longer lifetimes and lower diffusivity the larger the clusters are.

In chapter 6, we illustrate a local basin approach for kART, to deal more efficiently with systems in which multiple independent oscillators dominate the system kinetics. Flickering

basins (groups of oscillating minima) are far apart and spatially protected, geometrically, treated as single events, and limit information loss between events. The internal kinetics of each local basin is solved analytically using the accelerated basin method (bacMRM); the transition rates that allow the basin to exit are corrected by taking into account the correlations between states within the basin. In addition, the basin reconstruction algorithm will allow us to recover all the intra-basin and exit basin states as well as their connectivity graph when the system falls again into a previously visited local basin. This work is still being prepared for submission to a journal, but there is still some implementation to be done.

The work presented in this thesis is subject to further improvement and investigation. The following are the points that represent open questions of this work:

(1) As we saw in chapter 4, pressure can change C stability and diffusivity in GB in ways that depend strongly on the local environment and the nature of the deformation. It will be interesting to see how a multi-atom profile affects these results. Additional C atoms may block possible diffusion paths and elastically deform the system. In addition, the segregation profile depends on stress, as it can cause a rearrangement of the segregated atoms. In addition, it will be interesting to see how other defects, such as vacancies and substitution atoms, diffuse into GBs under pressure.

(2) In the standard KMC method, the master equation provides jump probabilities of the transitioning defects. Irradiation leads to long-term phenomena such as dislocations and dislocation loops, where a plane is normally missing. Standard KMC simulations are not efficient enough to study the evolution law over a long period of time. Using the local basin approach developed (as discussed in chapter 6), we can characterize the long-term evolution of defects. This can be achieved by relying on the local basin approach to the kART method. The law of evolution, from one state to another, leads to a macro jump.

(3) The local basin algorithm using the kART method discussed in Chapter 6 is under development. Therefore, there are no supporting results regarding its applications.

However, the algorithm could be more efficient and accurate in studying recombination kinetics for point defects.

(4) We note that the proposed local basin approach is based on the actual transition rate matrix in the crystal lattice. Therefore, it can be used to study the anisotropic migration of interstitial clusters whose diffusion mechanism mixes fast translations and slow rotations. In addition, the local basin approach can efficiently allow the calculation of sink strengths relative to defect clusters that exhibit mixed mobilities.

We believe that atomic numerical approaches to materials simulation have a promising future. Several options should be considered soon. Although kART is able to achieve time scales that cannot be reached by MD, such approaches are still more computationally intensive than lattice-based atomistic KMC. Moreover, kART is typically limited to a couple of tens of thousands of KMC steps, excluding analytically treated flickers. Consequently, these techniques are only applicable to systems where local mechanisms clearly dominate the physically relevant mechanisms. For example, simulating vacancy-induced solute diffusion in metals, where the proximity of a vacancy to a solute is required to observe an atomic jump, is considered too costly. To circumvent these limitations, one can calculate the equilibrium distribution of vacancies in the system during the time interval between configurations in which vacancies are near a solute. Alternatively, one could integrate off-lattice KMC with lattice-based KMC to provide efficient resolution of vacancy diffusion away from the solute while accurately accounting for elastic effects and interactions between solute and point defects through an off-lattice representation. Alternative options undoubtedly exist, and further research in this area is needed to determine the optimal approach to integrating these scales. Moreover, the ability of the kART method to manage defects is usually limited to a small number of defects, typically a few hundred. Increasing the number of defects leads to an increase in computational effort in two distinct ways. (1) It is necessary to assign events to each additional defect. Although optimising the reuse of events can lead to a reduction in computational effort, this is not always a feasible approach. For concentrated alloys, the number of local configurations increases exponentially with the number of

constituents, limiting the effectiveness of event reuse. As the number of defects increases, so do the overall rates, reducing the waiting time for each KMC step. To achieve identical time scales, additional computational resources in the form of KMC steps are required. Although synchronous and asynchronous parallelization techniques for the kinetic Monte Carlo (KMC) method provide a potential solution to this problem, it remains an unsolved obstacle for off-lattice KMC. Another major limitation of the on-the-fly kinetic Monte Carlo (KMC) such as the kART method concerns the study of the potential energy surface. In cases where the free energy is significantly affected by entropic factors, relying solely on the analysis of the surface of the potential energy can lead to erroneous predictions. To function optimally, these accelerated methods must use an appropriate and comparatively limited collection of response coordinates. It is conceivable that KMC could be used in the future in real-time to identify favourable reaction coordinates that can be used as input to accelerated free-energy techniques.

In summary, this type of research project combining theory and numerics is becoming a new norm. Moreover, the collaboration between numerical theorists and experimentalists is becoming more and more important, as experiments are more precise than ever, and at the same time, numerical simulations are more realistic and can handle more complex systems.

References

[1] *LAMMPS web site*. `http://lammps.sandia.gov`.

[2] Salawu Omotayo Akande, El Tayeb Bentia, Othmane Bouhali, and Fedwa El-Mellouhi. Searching for the rate determining step of the h2s reaction on fe (110) surface. *Applied Surface Science*, page 147470, 2020.

[3] Berni J Alder and Thomas Everett Wainwright. Studies in molecular dynamics. i. general method. *The Journal of Chemical Physics*, 31(2):459–466, 1959.

[4] Mie Andersen, Chiara Panosetti, and Karsten Reuter. A practical guide to surface kinetic monte carlo simulations. *Frontiers in chemistry*, 7:202, 2019.

[5] Sharon E Ashbrook, John M Griffin, and Karen E Johnston. Recent advances in solid-state nuclear magnetic resonance spectroscopy. *Annual Review of Analytical Chemistry*, 11:485–508, 2018.

[6] Robert S Averback and T Diaz De La Rubia. Displacement damage in irradiated metals and semiconductors. *Solid State Physics-Advances in Research and Applications*, 51(C):281–402, 1997.

[7] GT Barkema and Normand Mousseau. Event-based relaxation of continuous disordered systems. *Physical review letters*, 77(21):4358, 1996.

[8] S A_ Barnett and A_ Rockett. Monte carlo simulations of si (001) growth and reconstruction during molecular beam epitaxy. *Surface science*, 198(1-2):133–150, 1988.

[9] Charlotte Becquart, Normand Mousseau, and Christophe Domain. Kinetic monte carlo simulations of irradiation effects. 2020.

[10] CS Becquart, Jean-Marc Raulot, Guy Bencteux, Christophe Domain, Michel Perez, Sébastien Garruchet, and Hoang Nguyen. Atomistic modeling of an fe system with a small concentration of c. *Computational materials science*, 40(1):119–129, 2007.

[11] JR Beeler Jr and RA Johnson. Vacancy clusters in α-iron. *Physical Review*, 156(3):677, 1967.

[12] Laurent Karim Béland, Yonathan Anahory, Dries Smeets, Matthieu Guihard, Peter Brommer, Jean-François Joly, Jean-Christophe Pothier, Laurent J Lewis, Normand Mousseau, and François Schiettekatte. Replenish and relax: Explaining logarithmic annealing in ion-implanted c-si. *Physical review letters*, 111(10):105502, 2013.

[13] Laurent Karim Béland, Peter Brommer, Fedwa El-Mellouhi, Jean-François Joly, and Normand Mousseau. Kinetic activation-relaxation technique. *Physical Review E*, 84(4):046704, 2011.

[14] Laurent Karim Béland, Yuri N Osetsky, Roger E Stoller, and Haixuan Xu. Kinetic activation–relaxation technique and self-evolving atomistic kinetic monte carlo: Comparison of on-the-fly kinetic monte carlo algorithms. *Computational Materials Science*, 100:124–134, 2015.

[15] E.T. Bentria, G.K. N'tsouaglo, C.S. Becquart, O. Bouhali, N. Mousseau, and F. El-Mellouhi. The role of emerging grain boundary at iron surface, temperature and hydrogen on metal dusting initiation. *Acta Materialia*, 135:340–347, 2017.

[16] A Bhattacharya, E Meslin, J Henry, A Barbu, S Poissonnet, and B Décamps. Effect of chromium on void swelling in ion irradiated high purity fe–cr alloys. *Acta Materialia*, 108:241–251, 2016.

[17] Alfred B Bortz, Malvin H Kalos, and Joel L Lebowitz. A new algorithm for monte carlo simulation of ising spin systems. *Journal of Computational Physics*, 17(1):10–18, 1975.

[18] Peter Brommer, Laurent Karim Béland, Jean-François Joly, and Normand Mousseau. Understanding long-time vacancy aggregation in iron: A kinetic activation-relaxation technique study. *Physical Review B*, 90(13):134109, 2014.

[19] William D Callister Jr and David G Rethwisch. *Fundamentals of materials science and engineering: an integrated approach*. John Wiley & Sons, 2020.

[20] R Candela, S Gelin, N Mousseau, RGA Veiga, C Domain, M Perez, and CS Becquart. Investigating the kinetics of the formation of a c cottrell atmosphere around a screw dislocation in bcc iron: a mixed-lattice atomistic kinetic monte-carlo analysis. *Journal of Physics: Condensed Matter*, 33(6):065704, 2020.

[21] Nicolas Castin, MI Pascuet, and L Malerba. Mobility and stability of large vacancy and vacancy–copper clusters in iron: An atomistic kinetic monte carlo study. *Journal of Nuclear Materials*, 429(1-3):315–324, 2012.

[22] Chris Cesare and Shinichi Mochizuki. Graph-theory breakthrough tantalizes mathematicians. *Nat. News*, 2015.

[23] A. Chakrabarty, E.T. Bentria, S.A. Omotayo, O. Bouhali, N. Mousseau, C.S. Becquart, and F. El Mellouhi. Elucidating the role of extended surface defects at fe surfaces on co adsorption and dissociation. *Applied Surface Science*, 491:792–798, 2019.

[24] A. Chakrabarty, O. Bouhali, N. Mousseau, C.S. Becquart, and F. El-Mellouhi. Influence of surface vacancy defects on the carburisation of fe 110 surface by carbon monoxide. *Journal of Chemical Physics*, 145(4), 2016.

[25] Aurab Chakrabarty, Othmane Bouhali, Normand Mousseau, Charlotte S Becquart, and Fedwa El-Mellouhi. Insights on finite size effects in ab initio study of co adsorption and dissociation on fe 110 surface. *Journal of Applied Physics*, 120(5):055301, 2016.

[26] Lirong Chen, Wenbin Liu, Long Yu, Yangyang Cheng, Ke Ren, Haonan Sui, Xin Yi, and Huiling Duan. Probabilistic and constitutive models for ductile-to-brittle transition in steels: A competition between cleavage and ductile fracture. *Journal of the Mechanics and Physics of Solids*, 135:103809, 2020.

[27] Junghyun Cho, Jeffrey M Rickman, Helen M Chan, and Martin P Harmer. Modeling of grain-boundary segregation behavior in aluminum oxide. *Journal of the American Ceramic Society*, 83(2):344–352, 2000.

[28] Emmanuel Clouet, Sébastien Garruchet, Hoang Nguyen, Michel Perez, and Charlotte S Becquart. Dislocation interaction with c in α-fe: A comparison between atomic simulations and elasticity theory. *Acta Materialia*, 56(14):3450–3460, 2008.

[29] M Cogoni, BP Uberuaga, AF Voter, and Luciano Colombo. Diffusion of small self-interstitial clusters in silicon: temperature-accelerated tight-binding molecular dynamics simulations. *Physical Review B*, 71(12):121203, 2005.

[30] Yinan Cui, Giacomo Po, and Nasr Ghoniem. Does irradiation enhance or inhibit strain bursts at the submicron scale? *Acta Materialia*, 132:285–297, 2017.

[31] Murray S Daw and Michael I Baskes. Semiempirical, quantum mechanical calculation of hydrogen embrittlement in metals. *Physical review letters*, 50(17):1285, 1983.

[32] Peter M Derlet, D Nguyen-Manh, and SL Dudarev. Multiscale modeling of crowdion and vacancy defects in body-centered-cubic transition metals. *Physical Review B*, 76(5):054107, 2007.

[33] Tomas Diaz de la Rubia, Hussein M Zbib, Tariq A Khraishi, Brian D Wirth, Max Victoria, and Maria Jose Caturla. Multiscale modelling of plastic flow localization in irradiated materials. *Nature*, 406(6798):871–874, 2000.

[34] B Dieny and M Chshiev. Perpendicular magnetic anisotropy at transition metal/oxide interfaces and applications. *Reviews of Modern Physics*, 89(2):025008, 2017.

[35] George Ellwood Dieter and David Bacon. *Mechanical metallurgy*, volume 3. McGraw-hill New York, 1976.

[36] FG Djurabekova, Lorenzo Malerba, C Domain, and CS Becquart. Stability and mobility of small vacancy and copper-vacancy clusters in bcc-fe: An atomistic kinetic monte carlo study. *Nuclear Instruments and Methods in Physics Research Section B: Beam Interactions with Materials and Atoms*, 255(1):47–51, 2007.

[37] Flyura Djurabekova, Lorenzo Malerba, Roberto C Pasianot, Pär Olsson, and Kai Nordlund. Kinetics versus thermodynamics in materials modeling: The case of the di-vacancy in iron. *Philosophical Magazine*, 90(19):2585–2595, 2010.

[38] C Domain, CS Becquart, and L Malerba. Simulation of radiation damage in fe alloys: an object kinetic monte carlo approach. *Journal of Nuclear Materials*, 335(1):121–145, 2004.

[39] Jincheng Du and Jessica M Rimsza. Atomistic computer simulations of water interactions and dissolution of inorganic glasses. *npj Materials Degradation*, 1(1):16, 2017.

[40] F. El-Mellouhi, N. Mousseau, and Laurent J. Lewis. Kinetic activation-relaxation technique: An off-lattice self-learning kinetic Monte Carlo algorithm. *Physical Review B*, 78(15):153202, 2008.

[41] JH Evans. Observations of a regular void array in high purity molybdenum irradiated with 2 mev nitrogen ions. *Nature*, 229(5284):403–404, 1971.

[42] Merdith G Evans and Michael Polanyi. Some applications of the transition state method to the calculation of reaction velocities, especially in solution. *Transactions of the Faraday Society*, 31:875–894, 1935.

[43] Henry Eyring. The activated complex in chemical reactions. *The Journal of Chemical Physics*, 3(2):107–115, 1935.

[44] Francesco Ferroni, Xiaoou Yi, Kazuto Arakawa, Steven P Fitzgerald, Philip D Edmondson, and Steve G Roberts. High temperature annealing of ion irradiated tungsten. *Acta Materialia*, 90:380–393, 2015.

[45] FC Frank. Dislocations and point defects. *Discussions of the Faraday Society*, 23:122–127, 1957.

[46] Chu-Chun Fu, Jacques Dalla Torre, François Willaime, Jean-Louis Bocquet, and Alain Barbu. Multiscale modelling of defect kinetics in irradiated iron. *Nature materials*, 4(1):68–74, 2005.

[47] Yuh Fukai. Electrical resistivity due to vacancies and impurities in aluminium: Band structure effects in the defect scattering in polyvalent metals. *Physics Letters A*, 27(7):416–417, 1968.

[48] Timothy H Gfroerer. Photoluminescence in analysis of surfaces and interfaces. *Encyclopedia of analytical chemistry*, 67:3810, 2000.

[49] MR Gilbert, SL Dudarev, PM Derlet, and DG Pettifor. Structure and metastability of mesoscopic vacancy and interstitial loop defects in iron and tungsten. *Journal of Physics: Condensed Matter*, 20(34):345214, 2008.

[50] MR Gilbert, Z Yao, MA Kirk, ML Jenkins, and SL Dudarev. Vacancy defects in fe: Comparison between simulation and experiment. *Journal of nuclear materials*, 386:36–40, 2009.

[51] Stefan Goedecker. Minima hopping: An efficient search method for the global minimum of the potential energy surface of complex molecular systems. *The Journal of chemical physics*, 120(21):9911–9917, 2004.

[52] Viktor I Grafutin and Evgenii P Prokop'ev. Positron annihilation spectroscopy in materials structure studies. *Physics-Uspekhi*, 45(1):59, 2002.

[53] R Gul, UN Roy, SU Egarievwe, AE Bolotnikov, GS Camarda, Y Cui, A Hossain, G Yang, and RB James. Point defects: Their influence on electron trapping, resistivity, and electron mobility-lifetime product in cdtexse1- x detectors. *Journal of Applied Physics*, 119(2):025702, 2016.

[54] AS Haja Hameed, S Rohani, WC Yu, CY Tai, and CW Lan. Surface defects and mechanical hardness of rapidly grown dast crystals. *Journal of crystal growth*, 297(1):146–151, 2006.

[55] J Heikinheimo, K Mizohata, J Räisänen, Tommy Ahlgren, P Jalkanen, A Lahtinen, N Catarino, E Alves, and Filip Tuomisto. Direct observation of mono-vacancy and self-interstitial recovery in tungsten. *APL Materials*, 7(2):021103, 2019.

[56] Graeme Henkelman and Hannes Jónsson. A dimer method for finding saddle points on high dimensional potential surfaces using only first derivatives. *The Journal of chemical physics*, 111(15):7010–7022, 1999.

[57] Graeme Henkelman and Hannes Jónsson. Long time scale kinetic monte carlo simulations without lattice approximation and predefined event table. *The Journal of Chemical Physics*, 115(21):9657–9666, 2001.

[58] G Hirth and DL Kohlstedt. The stress dependence of olivine creep rate: Implications for extrapolation of lab data and interpretation of recrystallized grain size. *Earth and Planetary Science Letters*, 418:20–26, 2015.

[59] P Hohenberg and WJPR Kohn. Density functional theory (dft). *Phys. Rev*, 136(1964):B864, 1964.

[60] Adam Hospital, Josep Ramon Goñi, Modesto Orozco, and Josep L Gelpí. Molecular dynamics simulations: advances and applications. *Advances and applications in bioinformatics and chemistry*, pages 37–47, 2015.

[61] Jie Hou, Xiang-Shan Kong, Xuebang Wu, Jun Song, and CS Liu. Predictive model of hydrogen trapping and bubbling in nanovoids in bcc metals. *Nature Materials*, 18(8):833–839, 2019.

[62] Jie Hou, Yu-Wei You, Xiang-Shan Kong, Jun Song, and CS Liu. Accurate prediction of vacancy cluster structures and energetics in bcc transition metals. *Acta Materialia*, 211:116860, 2021.

[63] Beverley J Inkson. Scanning electron microscopy (sem) and transmission electron microscopy (tem) for materials characterization. In *Materials characterization using non-destructive evaluation (NDE) methods*, pages 17–43. Elsevier, 2016.

[64] Akio Ishii, Ju Li, and Shigenobu Ogata. "conjugate channeling" effect in dislocation core diffusion: Carbon transport in dislocated bcc iron. *PloS one*, 8(4):e60586, 2013.

[65] Anna Jääskeläinen, Luciano Colombo, and Risto Nieminen. Silicon self-diffusion constants by tight-binding molecular dynamics. *Physical Review B*, 64(23):233203, 2001.

[66] Antoine Jay, Mélanie Raine, Nicolas Richard, Normand Mousseau, Vincent Goiffon, Anne Hémeryck, and Pierre Magnan. Simulation of single particle displacement damage in silicon–part ii: Generation and long-time relaxation of damage structure. *IEEE Transactions on Nuclear Science*, 64(1):141–148, 2016.

[67] Jean-François Joly, Laurent Karim Béland, Peter Brommer, Fedwa El-Mellouhi, and Normand Mousseau. Optimization of the kinetic activation-relaxation technique, an off-lattice and self-learning kinetic monte-carlo method. In *Journal of Physics: Conference*

Series, volume 341, page 012007. IOP Publishing, 2012.

[68] Jean-Francois Joly, Laurent Karim Béland, Peter Brommer, and Normand Mousseau. Contribution of vacancies to relaxation in amorphous materials: A kinetic activation-relaxation technique study. *Physical Review B*, 87(14):144204, 2013.

[69] Dmytro Kandaskalov, Claude Mijoule, and Damien Connétable. Study of multivacancies in alpha fe. *Journal of nuclear materials*, 441(1-3):168–177, 2013.

[70] Bijaya B Karki, Dipta B Ghosh, and Ashok K Verma. First-principles prediction of pressure-enhanced defect segregation and migration at mgo grain boundaries. *American Mineralogist*, 100(5-6):1053–1058, 2015.

[71] V Keppens, D Mandrus, B Chakoumakos Sales, BC Chakoumakos, P Dai, R Coldea, MB Maple, DA Gajewski, EJ Freeman, and S Bennington. Localized vibrational modes in metallic solids. *Nature*, 395(6705):876–878, 1998.

[72] PG Klemens. Thermal resistance due to point defects at high temperatures. *Physical review*, 119(2):507, 1960.

[73] P Klugkist, AN Aleshin, W Lojkowski, LS Shvindlerman, W Gust, and EJ Mittemeijer. Diffusion of zn along tilt grain boundaries in al:: pressure and orientation dependence. *Acta materialia*, 49(15):2941–2949, 2001.

[74] AF Kohan, Gerbrand Ceder, Dane Morgan, and Chris G Van de Walle. First-principles study of native point defects in zno. *Physical Review B*, 61(22):15019, 2000.

[75] Walter Kohn and Lu Jeu Sham. Self-consistent equations including exchange and correlation effects. *Physical review*, 140(4A):A1133, 1965.

[76] D Kulikov §, Lorenzo Malerba, and Marc Hou. On the binding energies and configurations of vacancy and copper–vacancy clusters in bcc fe–cu: a computational study. *Philosophical magazine*, 86(2):141–172, 2006.

[77] Yuko Kumeda, David J Wales, and Lindsey J Munro. Transition states and rearrangement mechanisms from hybrid eigenvector-following and density functional theory.: application to c10h10 and defect migration in crystalline silicon. *Chemical physics letters*, 341(1-2):185–194, 2001.

[78] Keith J Laidler and M Christine King. The development of transition-state theory. *J. phys. Chem*, 87(15):2657–2664, 1983.

[79] Alessandro Laio and Michele Parrinello. Escaping free-energy minima. *Proceedings of the national academy of sciences*, 99(20):12562–12566, 2002.

[80] DV Lang. Deep-level transient spectroscopy: A new method to characterize traps in semiconductors. *Journal of applied physics*, 45(7):3023–3032, 1974.

[81] Carl Lévesque, Sjoerd Roorda, François Schiettekatte, and Normand Mousseau. Internal mechanical dissipation mechanisms in amorphous silicon. *Physical Review Materials*, 6(12):123604, 2022.

[82] Zhichao Li, Andrew M Freborg, Bruce D Hansen, and Tirumalai S Srivatsan. Modeling the effect of carburization and quenching on the development of residual stresses and bending fatigue resistance of steel gears. *Journal of materials engineering and performance*, 22(3):664–672, 2013.

[83] Binggang Liu, Wei Li, Xianwen Lu, Xiaoshuai Jia, and Xuejun Jin. The effect of retained austenite stability on impact-abrasion wear resistance in carbide-free bainitic steels. *Wear*, 428:127–136, 2019.

[84] W Lojkowski, U Södervall, S Mayer, and W Gust. The effect of pressure on indium diffusion along< 001> tilt grain boundaries in copper bicrystals. *Interface Science*, 6(3):187–196, 1998.

[85] Witold Łojkowski. Evidence for pressure effect on impurity segregation in grain boundaries and interstitial grain boundary diffusion mechanism. In *Defect and Diffusion Forum*, volume 129, pages 269–278. Trans Tech Publ, 1996.

[86] Chenyang Lu, Liangliang Niu, Nanjun Chen, Ke Jin, Taini Yang, Pengyuan Xiu, Yanwen Zhang, Fei Gao, Hongbin Bei, Shi Shi, et al. Enhancing radiation tolerance by controlling defect mobility and migration pathways in multicomponent single-phase alloys. *Nature communications*, 7(1):13564, 2016.

[87] Jianming Lu, Hongdong Zhang, and Yuliang Yang. Monte carlo simulation of kinetics and chain-length distribution in radical polymerization. *Macromolecular Theory and*

Simulations, 2(5):747–760, 1993.

[88] Eduardo Machado-Charry, Laurent Karim Béland, Damien Caliste, Luigi Genovese, Thierry Deutsch, Normand Mousseau, and Pascal Pochet. Optimized energy landscape exploration using the ab initio based activation-relaxation technique. *The Journal of chemical physics*, 135(3):034102, 2011.

[89] Sami Mahmoud and Normand Mousseau. Long-time point defect diffusion in ordered nickel-based binary alloys: How small kinetic differences can lead to completely long-time structural evolution. *Materialia*, 4:575–584, 2018.

[90] Sami Mahmoud, Mickaël Trochet, Oscar A Restrepo, and Normand Mousseau. Study of point defects diffusion in nickel using kinetic activation-relaxation technique. *Acta Materialia*, 144:679–690, 2018.

[91] PA Maksym. Fast monte carlo simulation of mbe growth. *Semiconductor Science and Technology*, 3(6):594, 1988.

[92] Rachid Malek and Normand Mousseau. Dynamics of lennard-jones clusters: A characterization of the activation-relaxation technique. *Physical Review E*, 62(6):7723, 2000.

[93] Rachid Malek and Normand Mousseau. Dynamics of lennard-jones clusters: A characterization of the activation-relaxation technique. *Physical Review E*, 62(6):7723, 2000.

[94] Lorenzo Malerba, Napoleon Anento, Juan Pablo Balbuena, CS Becquart, Nicolas Castin, Maria José Caturla, Christophe Domain, C Guerrero, CJ Ortiz, B Pannier, et al. Physical mechanisms and parameters for models of microstructure evolution under irradiation in fe alloys–part i: Pure fe. *Nuclear Materials and Energy*, 29:101069, 2021.

[95] Lorenzo Malerba, Mihai-Cosmin Marinica, N Anento, C Björkas, H Nguyen, C Domain, F Djurabekova, Pär Olsson, K Nordlund, A Serra, et al. Comparison of empirical interatomic potentials for iron applied to radiation damage studies. *Journal of Nuclear Materials*, 406(1):19–38, 2010.

[96] Soroush Masoudi, Ghasem Amirian, Ehsan Saeedi, and Mohammad Ahmadi. The effect of quench-induced residual stresses on the distortion of machined thin-walled parts. *Journal of Materials Engineering and Performance*, 24(10):3933–3941, 2015.

[97] Brendan D McKay et al. Practical graph isomorphism. 1981.

[98] Brendan D McKay and Adolfo Piperno. Nauty and traces user's guide (version 2.5).

[99] Brendan D McKay and Adolfo Piperno. Practical graph isomorphism, ii. *Journal of symbolic computation*, 60:94–112, 2014.

[100] MI Mendelev, S Han, DJ Srolovitz, GJ Ackland, DY Sun, and M Asta. Development of new interatomic potentials appropriate for crystalline and liquid iron. *Philosophical magazine*, 83(35):3977–3994, 2003.

[101] Sinisa Dj Mesarovic. Lattice continuum and diffusional creep. *Proceedings of the Royal Society A: Mathematical, Physical and Engineering Sciences*, 472(2188):20160039, 2016.

[102] N. Mousseau, L. K. Béland, P. Brommer, F. El-Mellouhi, J. F. Joly, G. K. N'tsouaglo, O. A. Restrepo, and M. Trochet. Following atomistic kinetics on experimental timescales with the kinetic Activation Relaxation Technique. *Computational Materials Science*, 100:111–123, 2015.

[103] Normand Mousseau, Laurent Karim Béland, Peter Brommer, Fedwa El-Mellouhi, Jean-François Joly, Gawonou Kokou N'Tsouaglo, Oscar Restrepo, and Mickaël Trochet. Following atomistic kinetics on experimental timescales with the kinetic activation–relaxation technique. *Computational Materials Science*, 100:111–123, 2015.

[104] Normand Mousseau, Laurent Karim Béland, Peter Brommer, Jean-François Joly, Fedwa El-Mellouhi, Eduardo Machado-Charry, Mihai-Cosmin Marinica, and Pascal Pochet. The activation-relaxation technique: Art nouveau and kinetic art. *Journal of Atomic and Molecular Physics*, 2012, 2012.

[105] Normand Mousseau and Philippe Derreumaux. Exploring energy landscapes of protein folding and aggregation. *Frontiers in Bioscience-Landmark*, 13(12):4495–4516, 2008.

[106] Michihiko Nagumo and Kenichi Takai. The predominant role of strain-induced vacancies in hydrogen embrittlement of steels: Overview. *Acta Materialia*, 165:722–733, 2019.

[107] Kenichi Nakashima, Roger E Stoller, and Haixuan Xu. Recombination radius of a frenkel pair and capture radius of a self-interstitial atom by vacancy clusters in bcc fe.

Journal of Physics: Condensed Matter, 27(33):335401, 2015.

[108] Koichi Ohno and Satoshi Maeda. A scaled hypersphere search method for the topography of reaction pathways on the potential energy surface. *Chemical physics letters*, 384(4-6):277–282, 2004.

[109] JY Park, HCW Huang, RW Siegel, and RW Balluffi. A quantitative study of vacancy defects in quenched tungsten by combined field-ion microscopy and electrical resistometry. *Philosophical Magazine A*, 48(3):397–419, 1983.

[110] Michele Parrinello and Aneesur Rahman. Crystal structure and pair potentials: A molecular-dynamics study. *Physical review letters*, 45(14):1196, 1980.

[111] Steve Plimpton. Fast parallel algorithms for short-range molecular dynamics. *Journal of computational physics*, 117(1):1–19, 1995.

[112] Brian Puchala, Michael L. Falk, and Krishna Garikipati. An energy basin finding algorithm for kinetic monte carlo acceleration. *The Journal of Chemical Physics*, 132(13):134104, 2010.

[113] MJ Puska and RM Nieminen. Defect spectroscopy with positrons: a general calculational method. *Journal of Physics F: Metal Physics*, 13(2):333, 1983.

[114] KD Rasch, RW Siegel, and H Schultz. Quenching and recovery investigations of vacancies in tungsten. *Philosophical Magazine A*, 41(1):91–117, 1980.

[115] Oscar A Restrepo, Charlotte S Becquart, Fedwa El-Mellouhi, Othmane Bouhali, and Normand Mousseau. Diffusion mechanisms of c in 100, 110 and 111 fe surfaces studied using kinetic activation-relaxation technique. *Acta Materialia*, 136:303–314, 2017.

[116] Oscar A Restrepo, Normand Mousseau, Fedwa El-Mellouhi, Othmane Bouhali, Mickaël Trochet, and Charlotte S Becquart. Diffusion properties of fe–c systems studied by using kinetic activation–relaxation technique. *Computational Materials Science*, 112:96–106, 2016.

[117] Oscar A Restrepo, Normand Mousseau, Mickaël Trochet, Fedwa El-Mellouhi, Othmane Bouhali, and Charlotte S Becquart. Carbon diffusion paths and segregation at high-angle tilt grain boundaries in α-fe studied by using a kinetic activation-relation technique.

Physical Review B, 97(5):054309, 2018.

[118] Sougata Roy, George Theng Ching Ooi, and Sriram Sundararajan. Effect of retained austenite on micropitting behavior of carburized aisi 8620 steel under boundary lubrication. *Materialia*, 3:192–201, 2018.

[119] Iwan Halim Sahputra, Aurab Chakrabarty, Oscar Restrepo, Othmane Bouhali, Normand Mousseau, Charlotte S Becquart, and Fedwa El-Mellouhi. Carbon adsorption on and diffusion through the fe (110) surface and in bulk: Developing a new strategy for the use of empirical potentials in complex material set-ups. *Physica Status Solidi (b)*, 254(2):1600408, 2017.

[120] Andrea Elisabet Sand, Jesper Byggmästar, A Zitting, and K Nordlund. Defect structures and statistics in overlapping cascade damage in fusion-relevant bcc metals. *Journal of Nuclear Materials*, 511:64–74, 2018.

[121] Alecsandre Sauvé-Lacoursière, Simon Gelin, Gilles Adjanor, Christophe Domain, and Normand Mousseau. Unexpected role of prefactors in defects diffusion: The case of vacancies in the 55fe-28ni-17cr concentrated solid-solution alloys. *Acta Materialia*, 237:118153, 2022.

[122] Irwin H Segel. Enzyme kinetics: behavior and analysis of rapid equilibrium and steady state enzyme systems. 1975.

[123] AH Seville. Effects of vacancies on the physical properties of platinum. *Platinum Metals Review*, 19(3):96–99, 1975.

[124] Daniel Sheppard, Rye Terrell, and Graeme Henkelman. Optimization methods for finding minimum energy paths. *The Journal of chemical physics*, 128(13):134106, 2008.

[125] N Soneda, S Ishino, and T Diaz De la Rubia. Vacancy loop formation by'cascade collapse'in a-fe: A molecular dynamics study of 50kev cascades. *Philosophical magazine letters*, 81(9):649–659, 2001.

[126] Barbara Stuart. Infrared spectroscopy. *Kirk-Othmer encyclopedia of chemical technology*, 2000.

[127] Cheng Sun. A short review of defect superlattice formation in metals and alloys under irradiation. *Journal of Nuclear Materials*, page 153479, 2021.

[128] Cheng Sun, Chao Jiang, Ericmoore Jossou, Mehmet Topsakal, Simerjeet K Gill, Lynne E Ecker, and Jian Gan. Self-assembly of solid nanoclusters in molybdenum under gas ion implantation. *Scripta Materialia*, 194:113651, 2021.

[129] Cheng Sun, David J Sprouster, Yongfeng Zhang, Di Chen, Yongqiang Wang, Lynne E Ecker, and Jian Gan. Formation window of gas bubble superlattice in molybdenum under ion implantation. *Physical Review Materials*, 3(10):103607, 2019.

[130] Wenwen Sun, Yuman Zhu, Ross Marceau, Lingyu Wang, Qi Zhang, Xiang Gao, and Christopher Hutchinson. Precipitation strengthening of aluminum alloys by room-temperature cyclic plasticity. *Science*, 363(6430):972–975, 2019.

[131] Sibel Suzen, Hande Gurer-Orhan, and Luciano Saso. Detection of reactive oxygen and nitrogen species by electron paramagnetic resonance (epr) technique. *Molecules*, 22(1):181, 2017.

[132] Shigeru Suzuki, Minoru Obata, Kenji Abiko, and Hiroshi Kimura. Role of carbon in preventing the intergranular fracture in iron-phosphorus alloys. *Transactions of the Iron and Steel Institute of Japan*, 25(1):62–68, 1985.

[133] Shigeru Suzuki, S Tanii, K Abiko, and H Kimura. Site competition between sulfur and carbon at grain boundaries and their effects on the grain boundary cohesion in iron. *Metallurgical Transactions A*, 18(6):1109–1115, 1991.

[134] Deyana S Tchitchekova, Julien Morthomas, Fabienne Ribeiro, Roland Ducher, and Michel Perez. A novel method for calculating the energy barriers for carbon diffusion in ferrite under heterogeneous stress. *The Journal of chemical physics*, 141(3):034118, 2014.

[135] Mickaël Trochet, Laurent Karim Béland, Jean-François Joly, Peter Brommer, and Normand Mousseau. Diffusion of point defects in crystalline silicon using the kinetic activation-relaxation technique method. *Physical Review B*, 91(22):224106, 2015.

[136] Mickaël Trochet, Alecsandre Sauvé-Lacoursière, and Normand Mousseau. Algorithmic developments of the kinetic activation-relaxation technique: Accessing long-time kinetics

of larger and more complex systems. *The Journal of chemical physics*, 147(15):152712, 2017.

[137] Oleg Trushin, Altaf Karim, Abdelkader Kara, and Talat S Rahman. Self-learning kinetic monte carlo method: application to cu (111). *Physical Review B*, 72(11):115401, 2005.

[138] Roberto GA Veiga, CS Becquart, and M Perez. Comments on "atomistic modeling of an fe system with a small concentration of c". *Computational materials science*, 82:118–121, 2014.

[139] Roberto GA Veiga, Michel Perez, CS Becquart, Christophe Domain, and Sébastien Garruchet. Effect of the stress field of an edge dislocation on carbon diffusion in α-iron: Coupling molecular statics and atomistic kinetic monte carlo. *Physical Review B*, 82(5):054103, 2010.

[140] Lisa Ventelon, F Willaime, Chu-Chun Fu, M Heran, and I Ginoux. Ab initio investigation of radiation defects in tungsten: Structure of self-interstitials and specificity of di-vacancies compared to other bcc transition metals. *Journal of Nuclear Materials*, 425(1-3):16–21, 2012.

[141] George H Vineyard. Frequency factors and isotope effects in solid state rate processes. *Journal of Physics and Chemistry of Solids*, 3(1-2):121–127, 1957.

[142] Arthur F Voter. Classically exact overlayer dynamics: Diffusion of rhodium clusters on rh (100). *Physical review B*, 34(10):6819, 1986.

[143] Arthur F Voter. Hyperdynamics: Accelerated molecular dynamics of infrequent events. *Physical Review Letters*, 78(20):3908, 1997.

[144] Arthur F Voter. A method for accelerating the molecular dynamics simulation of infrequent events. *The Journal of chemical physics*, 106(11):4665–4677, 1997.

[145] Arthur F Voter. Parallel replica method for dynamics of infrequent events. *Physical Review B*, 57(22):R13985, 1998.

[146] Arthur F Voter. Introduction to the kinetic monte carlo method. In *Radiation effects in solids*, pages 1–23. Springer, 2007.

[147] F Wan, S Ohnuki, H Takahashi, T Takeyama, and R Nagasaki. Vacancy loop formation in hydrogen-ion-implanted alpha-iron. *Philosophical Magazine A*, 53(2):L21–L26, 1986.

[148] Lei Wan, Xiaoqiu Ye, Xingzhong Cao, Shuoxue Jin, and Tao Gao. First-principles study of helium in austenitic fe 6.3 at% cr alloys: Structural, stability, energetics, and clustering with vacancies. *Materials Today Communications*, 29:102837, 2021.

[149] Jingliang Wang, Rebecca Janisch, Georg KH Madsen, and Ralf Drautz. First-principles study of carbon segregation in bcc iron symmetrical tilt grain boundaries. *Acta Materialia*, 115:259–268, 2016.

[150] Zhiyong Wang, Youhong Li, and James B Adams. Kinetic lattice monte carlo simulation of facet growth rate. *Surface science*, 450(1-2):51–63, 2000.

[151] Bertram Eugene Warren. *X-ray Diffraction*. Courier Corporation, 1990.

[152] E Weinan, Weiqing Ren, and Eric Vanden-Eijnden. String method for the study of rare events. *Physical Review B*, 66(5):052301, 2002.

[153] Ming Wen, Akiyuki Takahashi, and Nasr M Ghoniem. Kinetics of self-interstitial cluster aggregation near dislocations and their influence on hardening. *Journal of nuclear materials*, 392(3):386–395, 2009.

[154] S Rushbrook Williams and LW Barr. A radioactive tracer study of diffusion processes in lead and silver bromide. *Le Journal de Physique Colloques*, 34(C9):C9–173, 1973.

[155] Ruqian Wu, Arthur J Freeman, and GB Olson. Effects of carbon on fe-grain-boundary cohesion: First-principles determination. *Physical Review B*, 53(11):7504, 1996.

[156] Xianglin Wu, Xiao Pan, Meimei Li, and James F Stubbins. Modeling tensile response and flow localization effects in 316ss after exposure to spallation and fission irradiation environments. *Journal of nuclear materials*, 343(1-3):302–307, 2005.

[157] Xiongwu Wu and Shaomeng Wang. Enhancing systematic motion in molecular dynamics simulation. *The Journal of chemical physics*, 110(19):9401–9410, 1999.

[158] Haixuan Xu, Yury N Osetsky, Roger E Stoller, et al. Simulating complex atomistic processes: On-the-fly kinetic monte carlo scheme with selective active volumes. *Physical Review B*, 84(13):132103, 2011.

[159] Haixuan Xu, Roger E Stoller, and Yury N Osetsky. Cascade defect evolution processes: Comparison of atomistic methods. *Journal of nuclear materials*, 443(1-3):66–70, 2013.

[160] Lijun Xu, Donghai Mei, and Graeme Henkelman. Adaptive kinetic monte carlo simulation of methanol decomposition on cu (100). *The Journal of chemical physics*, 131(24):244520, 2009.

[161] Hui Yang, Minsheng Huang, and Zhenhuan Li. The influence of vacancies diffusion-induced dislocation climb on the creep and plasticity behaviors of nickel-based single crystal superalloy. *Computational Materials Science*, 99:348–360, 2015.

[162] Yong-Gang Yang, Zhen-Li Mi, Mei Xu, Qi Xiu, Jun Li, and Hai-Tao Jiang. Impact of intercritical annealing temperature and strain state on mechanical stability of retained austenite in medium mn steel. *Materials Science and Engineering: A*, 725:389–397, 2018.

[163] Jiwang Zhang, Wei Li, Huaqiang Wang, Qingpeng Song, Liantao Lu, Wenjian Wang, and Zhongwei Liu. A comparison of the effects of traditional shot peening and micro-shot peening on the scuffing resistance of carburized and quenched gear steel. *Wear*, 368:253–257, 2016.

Appendix A

Supplementary material: Pressure effect on diffusion of carbon at the $85.91° < 100 >$ symmetric tilt grain boundary of $\alpha-$iron.

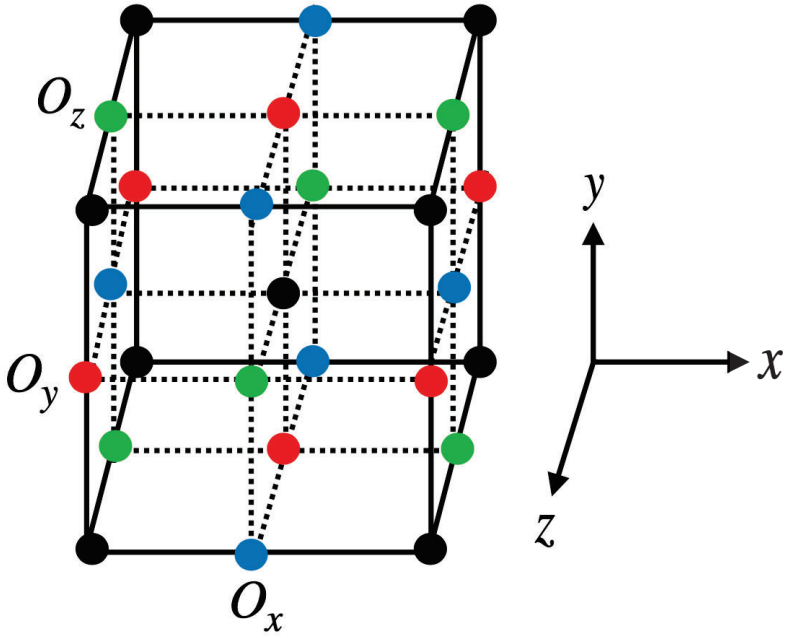

Fig. A.1. Schematic representation of atomic positions showing the three different octahedral interstitial sites (variants) within the bcc Fe unit cell. Iron atoms are represented by black circles, while the three structurally equivalent variants of octahedral interstitial directed along x, y, or z crystallographic axis are labeled and represented by blue, red and green circles respectively.

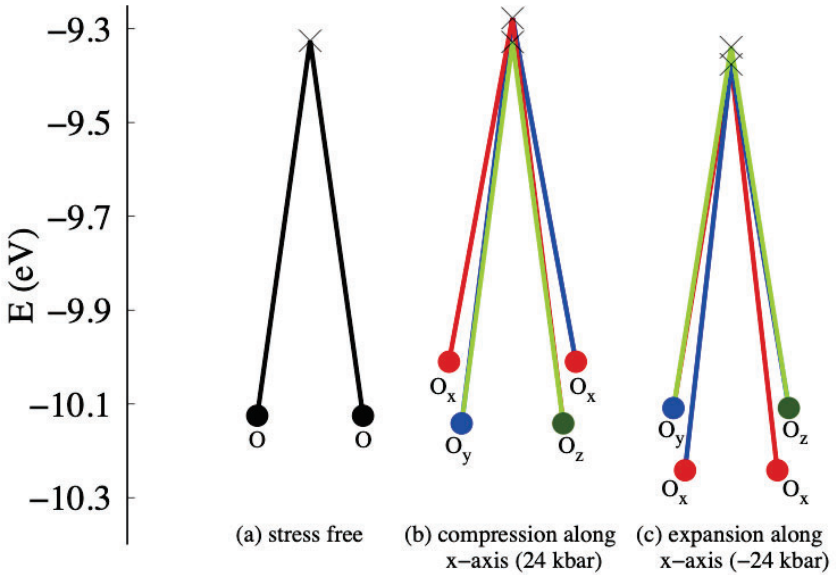

Fig. A.2. Octahedral to octahedral carbon diffusion pathways in a perfect BCC bulk iron at zero pressure and upon the application of with compressive and tensile strains along the x axis. Pressure leads to lifting the degeneracy in the energetics of the octohedral sites Ox, Oy, Oz. For each case, E is measured with respect to the energy of the pure Fe system under the same deformation. The circles and crosses represent the energy minima and saddle points, respectively.

Table A.1. Parameters of the functions fitting the data points of activation energies for a single carbon in the bulk under uniaxial and biaxial pressure which is shown in Fig.2 and Fig.3 .

			Constant term (eV)	Linear parameter (eV/kbar)	Quadratic parameter (eV/kbar^2)
Enthalpy	Isotropic pressure		-8033.830 ± 0.003	14.495 ± 0.001	$-0.004 \pm 8.61 \times 10^{-6}$
Activation energy	Isotropic pressure	$O \rightarrow O$	0.797 ± 0.002	$0.001 \pm 9.32 \times 10^{-5}$	$8.570 \times 10^{-6} \pm 6.07 \times 10^{-6}$
	Uniaxial pressure (x-axis)	$O_x \rightarrow O_y$		$-0.003 \pm 1.89 \times 10^{-5}$	$-3.96 \times 10^{-7} \pm 9.68 \times 10^{-7}$
		$O_y \rightarrow O_x$		$0.003 \pm 6.27 \times 10^{-6}$	$-2.52 \times 10^{-6} \pm 3.21 \times 10^{-7}$
		$O_y \rightarrow O_z$		$0.001 \pm 7.37 \times 10^{-6}$	$-1.44 \times 10^{-5} \pm 3.78 \times 10^{-7}$
	Biaxial pressure (y and z axes)	$O_x \rightarrow O_y$		$0.004 \pm 6.98 \times 10^{-6}$	$-8.47 \times 10^{-6} \pm 4.55 \times 10^{-7}$
		$O_y \rightarrow O_x$		$-0.002 \pm 3.10 \times 10^{-6}$	$-6.35 \times 10^{-6} \pm 2.02 \times 10^{-7}$
		$O_y \rightarrow O_z$		$1.30 \times 10^{-5} \pm \times 3.24 \times 10^{-6}$	$-6.05 \times 10^{-6} \pm 2.11 \times 10^{-7}$

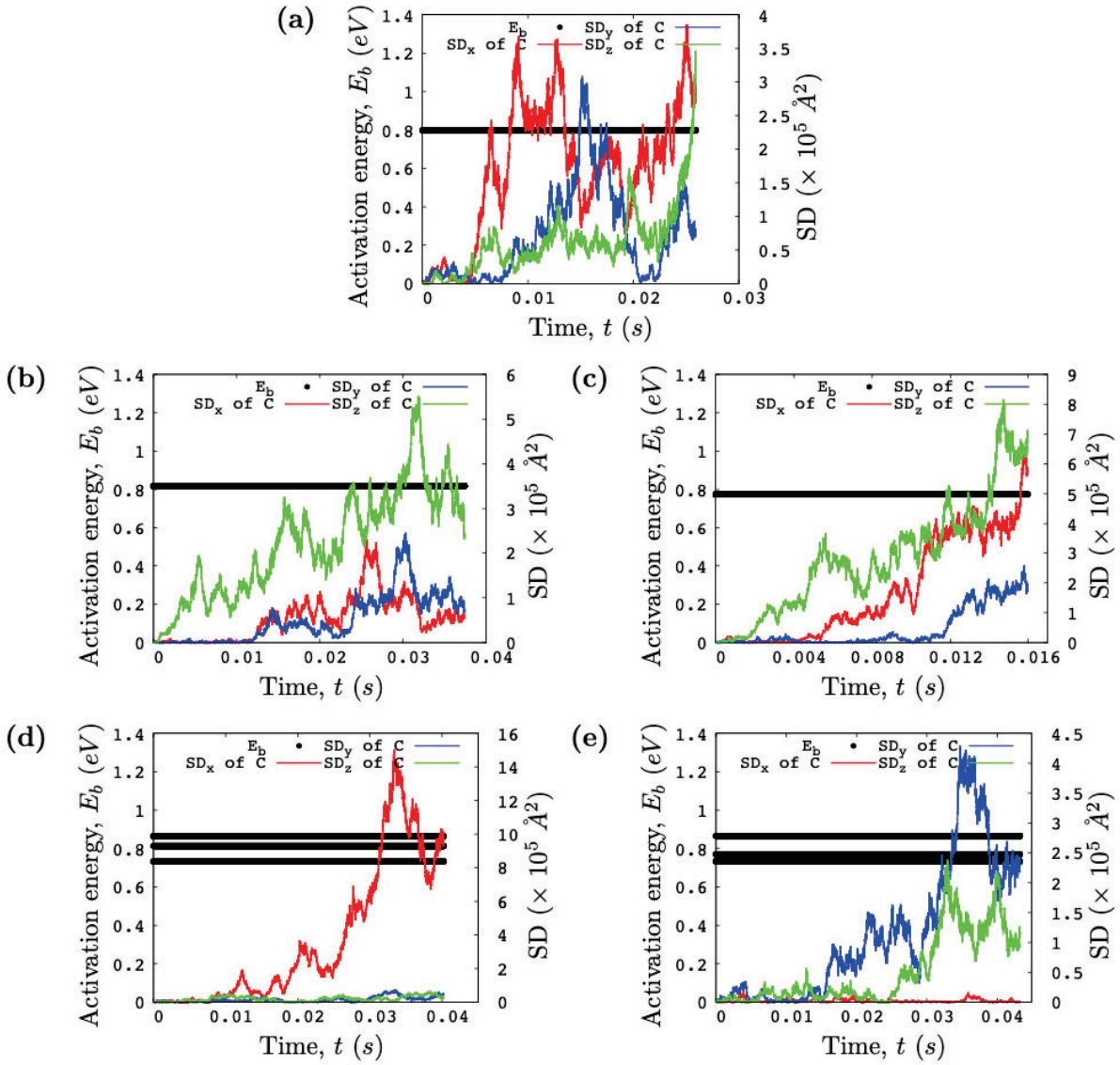

Fig. A.3. Activation-energy (left axis: black symbols) and squared displacement diffusion for a single C interstitial in a perfect crystall (right axis: red, blue and green line indicate the x, y and z direction respectively) as a function of time for 200 000 KMC steps run at 600 K for five different deformations: (a) stress free cell (0 kbar), (b) isotropic compression (24 kbar), (c) isotropic expansion (-24 kbar), (d) uniaxial compression (24 kbar) and (e) uniaxial expansion (-24 kbar).

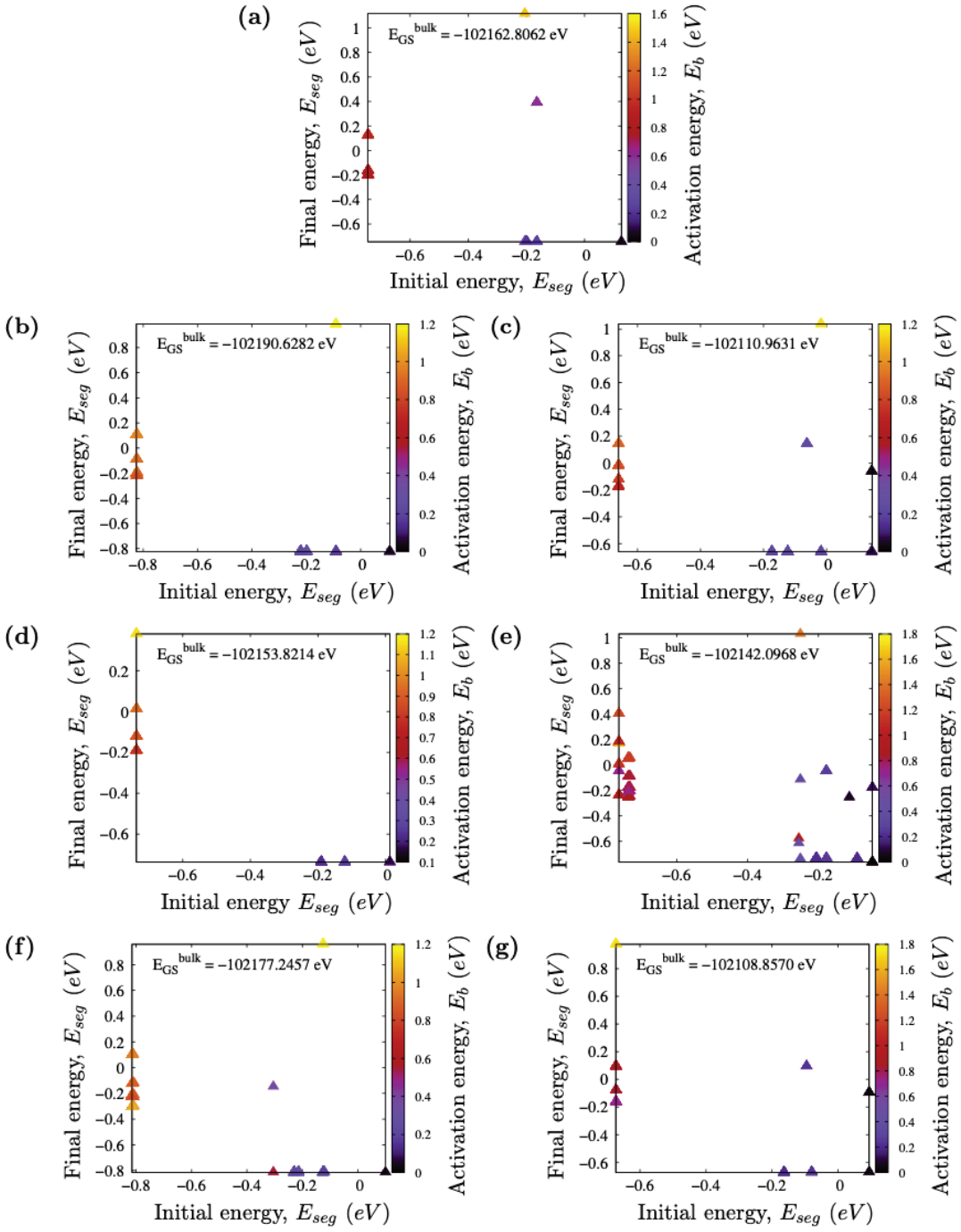

Fig. A.4. Representation of all available events for a single C at GB. The x and y axes represent the initial and final energy for each event, the color defines the saddle energy. All initial and final energies are measured with respect to the bulk ground state for C: (a) stress free cell (0 kbar), (b) isotropic compression (12 kbar), (c) isotropic expansion (-12 kbar), (d) uniaxial compression (12 kbar), (e) uniaxial expansion (-12 kbar), (f) biaxial compression (12 kbar) and (g) biaxial expansion (-12 kbar).

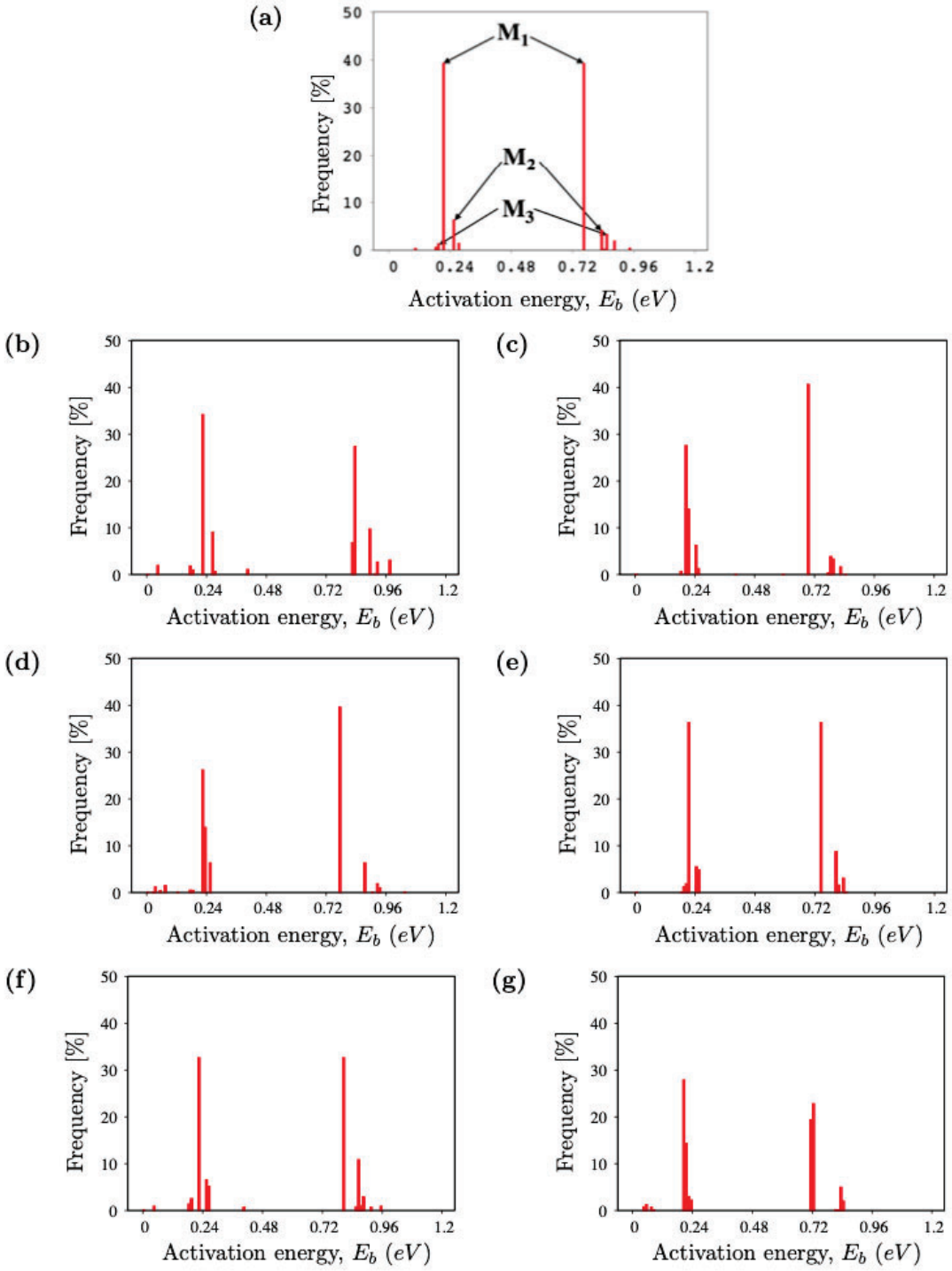

Fig. A.5. Histogram of the activation energy barriers of the available events during the 12000 KMC steps a single carbon at GB at 600 K: (a) stress free cell (0 kbar), (b) isotropic compression (12 kbar), (c) isotropic expansion (-12 kbar), (d) uniaxial compression (12 kbar), (e) uniaxial expansion (-12 kbar), (f) biaxial compression (12 kbar) and (g) biaxial expansion (-12 kbar)

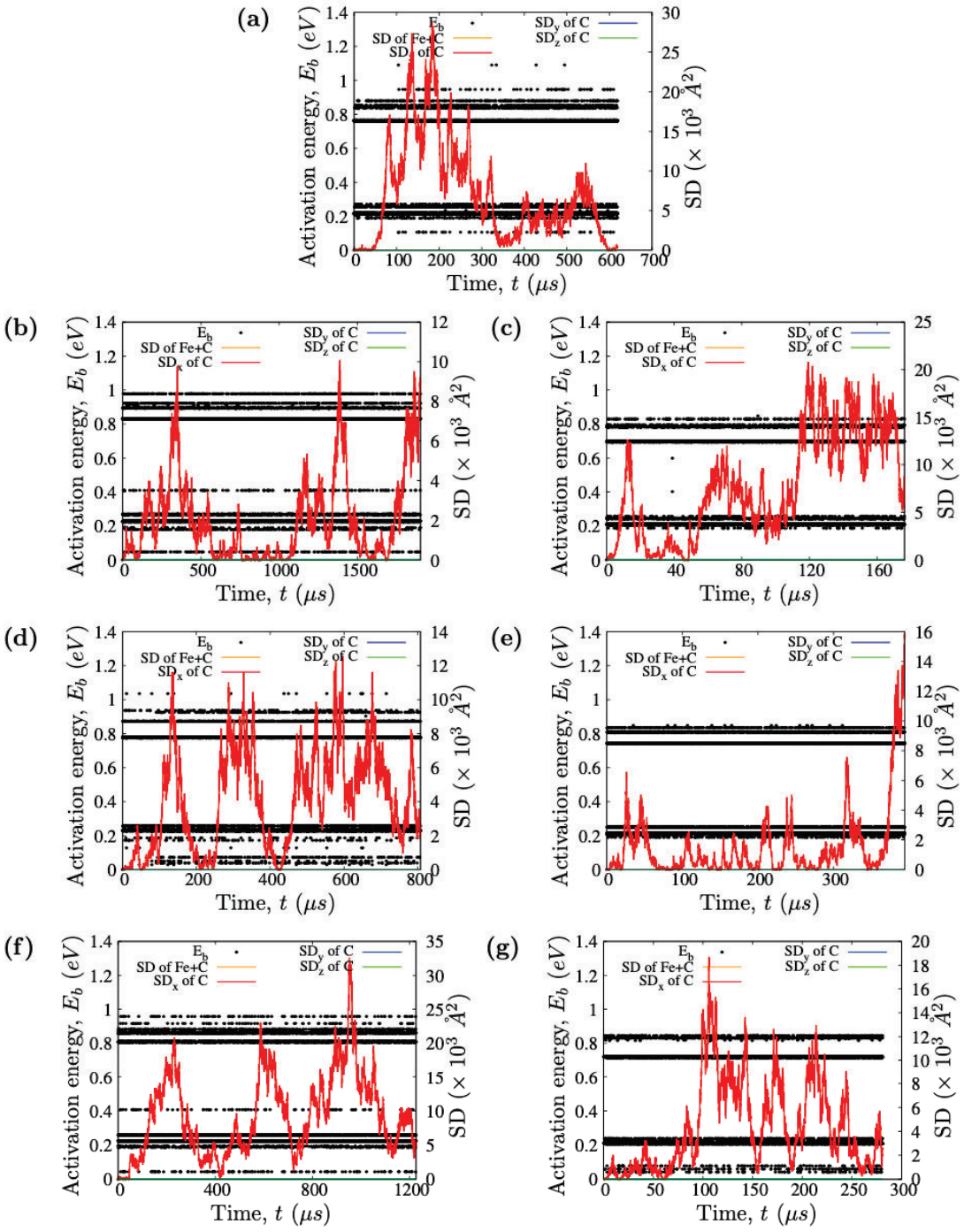

Fig. A.6. Activation energy (left, black symbols) and squared displacement diffusion (right, red, blue and green line represented x, y and z direction respectively) as a function of time for 12 000 KMC steps a single carbon at GB at 600 K: (a) stress free cell (0 kbar), (b) isotropic compression (12 kbar), (c) isotropic expansion (-12 kbar), (d) uniaxial compression (12 kbar), (e) uniaxial expansion (-12 kbar), (f) biaxial compression (12 kbar) and (g) biaxial expansion (-12 kbar)

Table A.2. The calculated activation volume V^{act} , activation barrier E^{act} and diffusion prefactor D_0 at zero pressure and temperature 600K. Activation volume and activation energy is calculated from the relationships, $V^{act} = -k_B T(\frac{\partial lnD}{\partial P})_T$ and $E^{act} = -k_B(\frac{\partial lnD}{\partial \frac{1}{T}})_P$ respectively. Where, k_B, T and P are Boltzmann constant, temperature and pressure respectively.

	Applied pressure	Activation volume V^{act} $(\times\ 10^{-30}\ m^3)$	Activation energy E^{act} (eV)	Diffusion prefactor D_0 $(\times\ 10^{-7}\ m^2 s^{-1})$
GB	Isotropic	8.702 ±0.002	0.772 ±0.001	6.020 ±0.02
	along x axis	2.664 ±0.012		
	along y and z axes	5.364 ±0.013		
Bulk	Isotropic	1.493 ±0.002	0.799 ±0.001	1.37 ±0.001
	along x axis	1.628 ± 0.009^a -1.782 ± 0.03^b		
	along y and z axis	3.012 ± 0.025^a -0.5 ± 0.005^b		

_ ^{a} under compression, ^{b} under expansion.

Appendix B

Supplementary material: Structural evolution of vacancy clusters in $\alpha-$iron: A kinetic activation-relaxation technique study

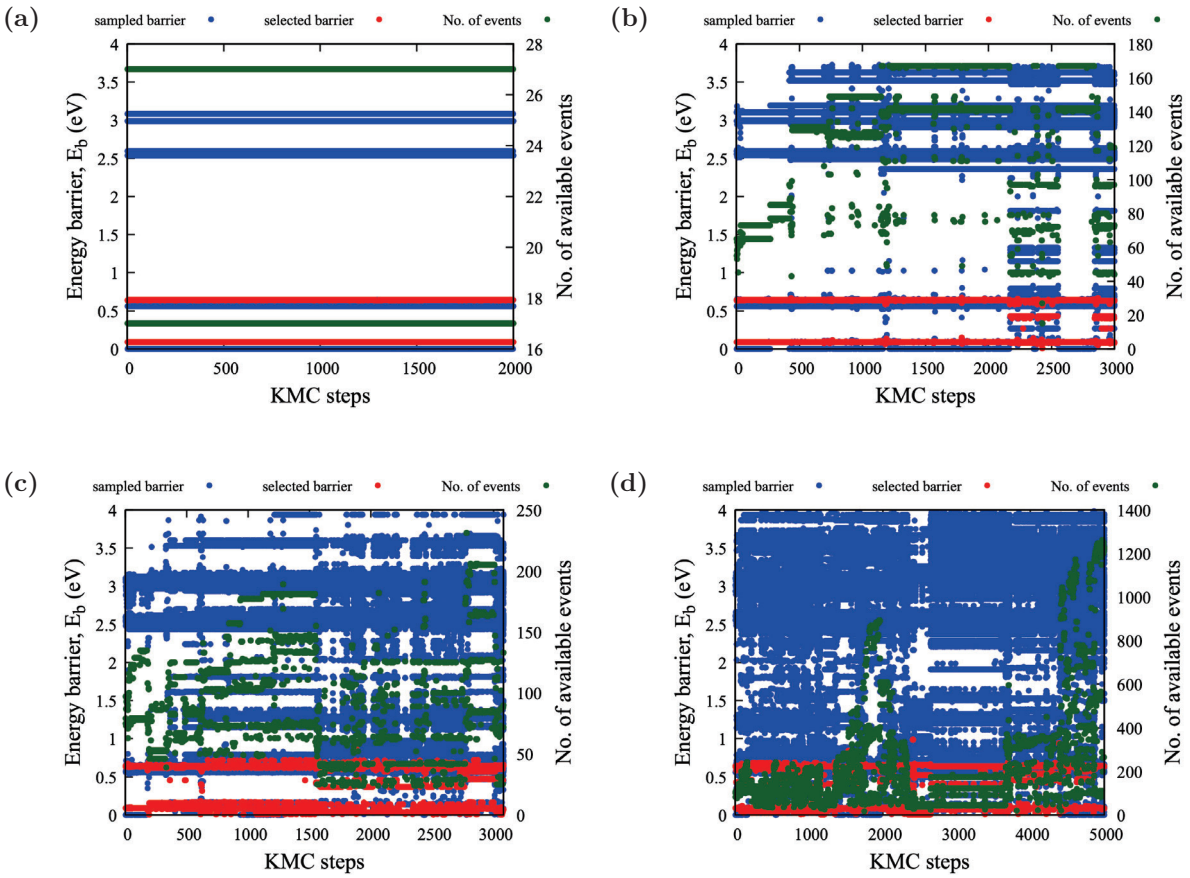

Fig. B.1. Evolution of the energy landscape as a function of KMC steps for (a) one, (b) two, (c) three, and (d) four vacancies in bcc Fe. Left axis: energy barrier for the sampled (blue symbols) and selected (red symbols) events. Right axis: number of available activation energies per KMC steps (green symbols).

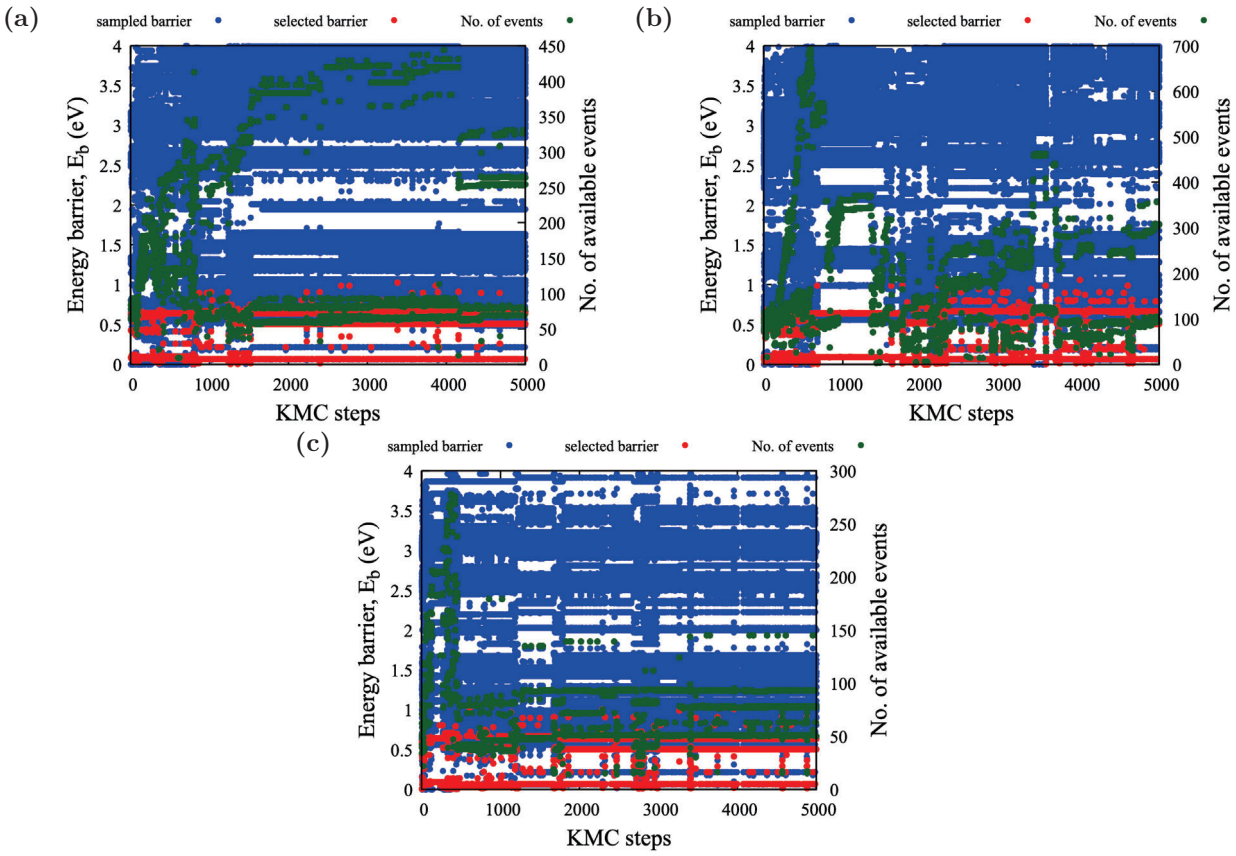

Fig. B.2. Evolution of the energy landscape as a function of KMC steps for initial line dislocation contains five vacancies along (a) [100], (b) [110], and (c) [111] in bcc Fe. Left axis: energy barrier for the sampled (blue symbols) and selected (red symbols) events. Right axis: number of available activation energies per KMC steps (green symbols).

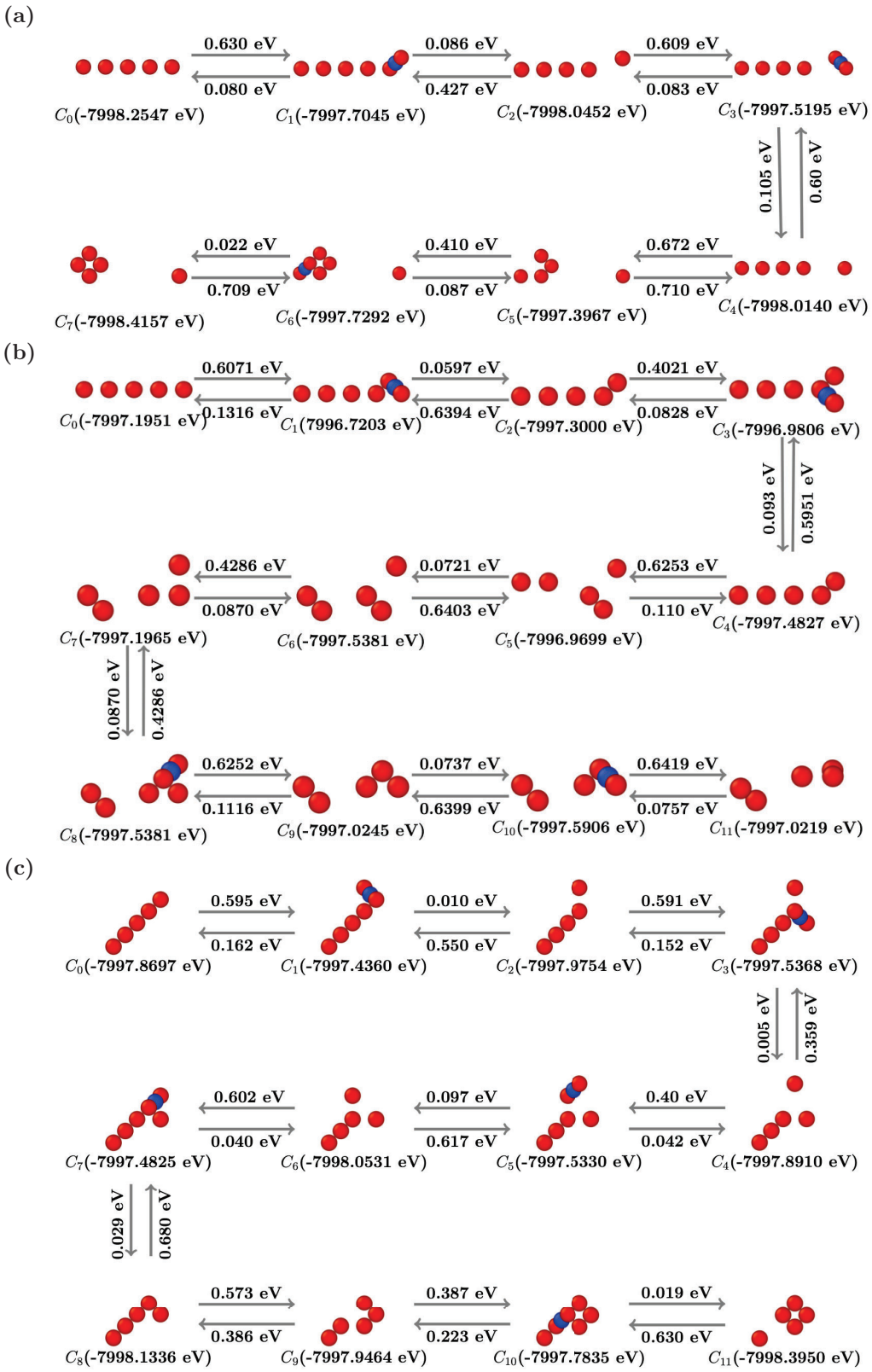

Fig. B.3. First few steps of the collapsing of the line dislocation of 5 vacancies along (a) [100], (b) [110], and (c) [111] direction.

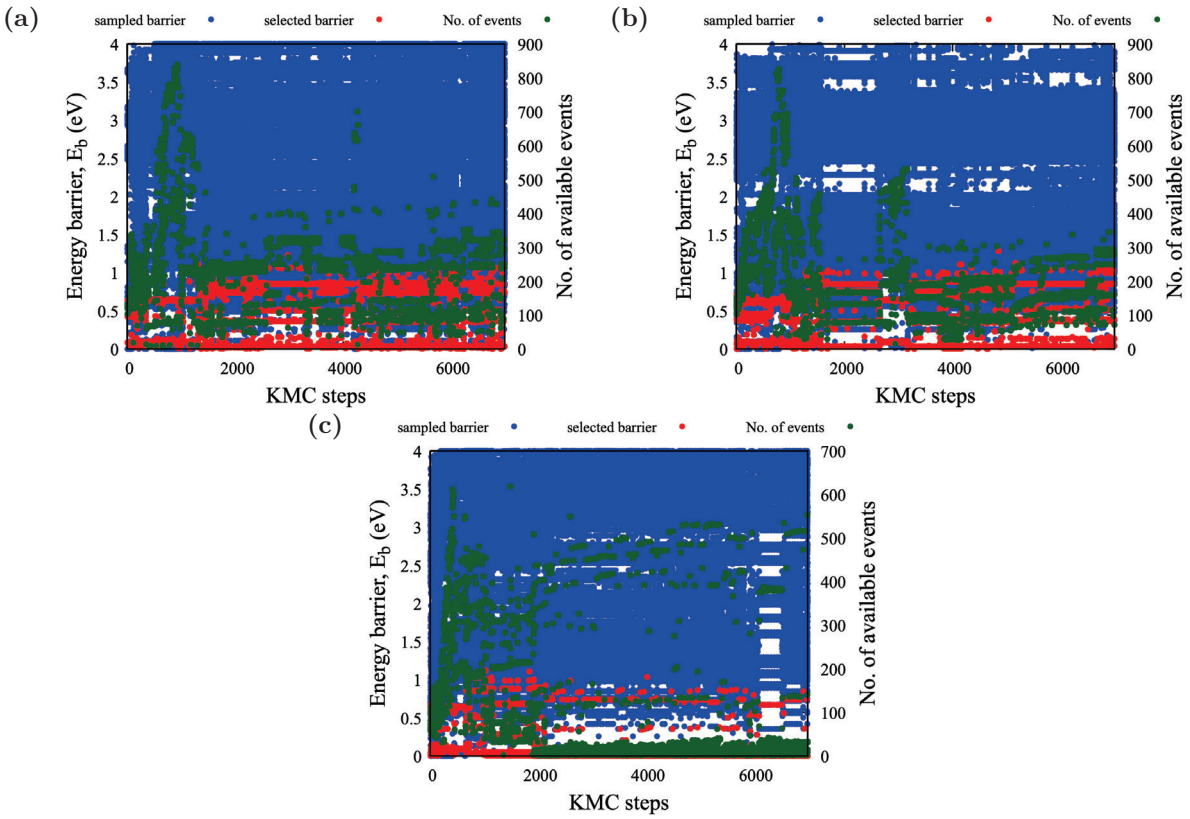

Fig. B.4. Evolution of the energy landscape as a function of KMC steps for initial line dislocation contains eight vacancies along (a) [100], (b) [110], and (c) [111] in bcc Fe. Left axis: energy barrier for the sampled (blue symbols) and selected (red symbols) events. Right axis: number of available activation energies per KMC steps (green symbols).